Structural, metamorphic and geochronological insights on the Variscan evolution of the Alpine basement in the Belledonne Massif (France)

Kévin Fréville, Pierre Trap, Michel Faure, Jérémie Melleton, Xian-Hua Li, Wei Lin, Olivier Blein, Olivier Bruguier, Marc Poujol

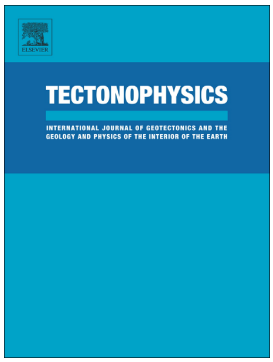

Structural, metamorphic and geochronological insights on the Variscan evolution of the Alpine basement in the Belledonne Massif (France)

Kévin Fréville, Pierre Trap, Michel Faure, Jérémie Melleton, Xian-Hua Li, Wei Lin, Olivier Blein, Olivier Bruguier, Marc Poujol

PII: S0040-1951(18)30029-5
DOI: https://doi.org/10.1016/j.tecto.2018.01.017
Reference: TECTO 127755

To appear in: *Tectonophysics*

Received date: 11 April 2017
Revised date: 12 January 2018
Accepted date: 16 January 2018

Please cite this article as: Kévin Fréville, Pierre Trap, Michel Faure, Jérémie Melleton, Xian-Hua Li, Wei Lin, Olivier Blein, Olivier Bruguier, Marc Poujol , Structural, metamorphic and geochronological insights on the Variscan evolution of the Alpine basement in the Belledonne Massif (France). The address for the corresponding author was captured as affiliation for all authors. Please check if appropriate. Tecto(2017), https://doi.org/10.1016/j.tecto.2018.01.017

Structural, metamorphic and geochronological insights on the Variscan evolution of the Alpine basement in the Belledonne Massif (France).

Kévin Fréville[a,c,] *, Pierre Trap[b], Michel Faure[a], Jérémie Melleton[c], Xian-Hua Li[d], Wei Lin[d], Olivier Blein[c], Olivier Bruguier[e], Marc Poujol[f]

* Corresponding author: kevin.freville@univ-orleans.fr

[a] UMR 7327, Institut des Sciences de la Terre d'Orléans, Université d'Orléans, CNRS, 45071 ORLEANS Cedex 2, France.

[b] UMR 6249 Chrono-environnement, Université de Franche-Comté, 16 route de Gray, 25030 Besançon Cedex, France

[c] BRGM, Georesources Division, Mineral deposit studies and development unit, 3, avenue Claude-Guillemin, BP 36009 - 45060 Orléans cedex 2 – France

[d] State Key Laboratory of Lithospheric Evolution, Institute of Geology and Geophysics, Chinese Academy of Sciences, Beijing, China.

[e] Géosciences Montpellier, Université de Montpellier II, Place Eugene Bataillon, 34095 Montpellier Cedex 5, France

[f] Géosciences Rennes, UMR CNRS 6118, OSUR, Université Rennes 1, 35042 Rennes Cedex, France

Abstract:

A structural and petrochronological study was carried out in the southern part of the Belledonne crystalline massif. A first tectonometamorphic event, Dx, corresponds to the eastward thrusting of the Chamrousse ophiolitic complex characterized by a low-temperature–moderate-pressure metamorphism reaching 0.535 ± 0.045 GPa and 427.5 ± 17.5 °C. A subsequent D_1 deformation is defined by a penetrative S_1 foliation that mostly dips towards the west and displays an E-W- to NE-SW-trending mineral and stretching lineation L_1. D_1 is associated with a top-to-the east shearing and is responsible for the crustal thickening accommodated by the eastward nappe stacking and the emplacement of the Chamrousse ophiolitic complex upon the Rioupéroux-Livet unit. This event is characterized by an amphibolite facies metamorphism (0.58 GPa ± 0.06; 608 ± 14 °C) that attains partial melting at the base of the nappe pile (0.78 ± 0.07 GPa; 680.5 ± 11.5 °C). LA-ICP-MS U-Pb dating of monazite grains from the mica schists of the Rioupéroux-Livet unit constrain the age of D_1 to 337 ± 7 Ma. The D_2 tectono-metamorphic event is characterized by NE-SW trending, upright to NE-verging synfolial folding. Folding associated with D_2 is pervasively developed in all lithotectonic units with the development of a steeply-dipping S_2 foliation. In particular, D_2 involves the uppermost weakly metamorphosed Taillefer unit. LA-ICP-MS U-Pb dating performed on detrital zircon grains shows that the Taillefer conglomerates was deposited during the Visean. A zircon SIMS U-Pb age of 352±1 Ma from a plagioglase-rich leucocratic sill of the Rioupéroux-Livet unit is interpreted as the age of magmatic emplacement. Our results suggest that the D_2 event took place between 330 Ma and 310 Ma. We propose a new interpretation of the tectonometamorphic evolution of the southern part of the Belledonne massif, focusing on the Middle Carboniferous stages of the Variscan orogeny.

Keywords: Variscan Belt, Alpine External Crystalline Massifs, Belledonne Massif, SIMS and LA-ICP-MS dating, Thermobarometry, zircon and monazite dating

1. Introduction

In Europe, the Variscan belt is interpreted as the result of a Devonian to Carboniferous continent-continent collision of Laurussia in the north, and Gondwana in the south, with several intermediate micro-continents trapped between them (Autran and Cogné, 1980; Ballèvre et al., 2009; Bard et al., 1980; Franke, 2000; Faure et al., 2005; Matte, 1986, 2007; Paris and Robardet, 1990; Stampfli et al., 2013; Tait et al., 1997, 2000; Von Raumer et al., 2003). The Variscan orogenic evolution is relatively well documented in the main crystalline massifs found in Iberia, the Armorican Massif, French Massif Central, Vosges, Ardennes, and the Bohemian Massif (Lardeaux et al., 2014; Stampfli et al., 2002, 2013) (Fig. 1A). The Variscan belt is also exposed through the Alpine Basement, as the East Variscan branch, with its External Crystalline Massifs (ECMs, Fig. 1B), which have been much less studied. While there are controversies concerning the timing of the main tectonometamorphic events and the correlations of the ECM's distinct basement domains, several interpretations have already been proposed, with comparisons to the Maures-Tanneron Massif, the Corsica-Sardinia region, and other Variscan fragments of the Alps (Corsini and Rolland, 2009; Fernandez et al., 2002; Faure et al., 2014; Guillot et al., 2009; Guillot and Ménot, 2009; Rossi et al., 2009; Von Raumer et al., 2013). A first interpretation argues that the East Variscan branch resulted from a tectonic collage along a N030°E East Variscan Shear Zone (EVSZ) during late Carboniferous to Permian time (Corsini and Rolland, 2009; Guillot et al., 2009; Padovano et al., 2012). A second interpretation suggests that the Variscan massifs of the East Variscan branch first drifted from the Gondwana margin, and then accreted along the Armorica during early Paleozoic time (Stampfli et al., 2002; Von Raumer, 1998; Von Raumer et al., 2003, 2009, 2013, 2014, 2015).

This contribution presents new structural, P-T estimates and geochronological constraints (LA-ICP-MS U-Pb on zircon and monazite) for the southwestern Belledonne Massif, mostly along the Romanche Valley and surrounding areas (Fig 2). These results represent crucial records for the ECMs, enabling us to better define a relevant geodynamic model for the Variscan Orogen, particularly for Middle Carboniferous time.

2. Geological setting

2.1 The External Crystalline Massifs

The ECMs are composed of various Cambrian to Carboniferous metamorphic, plutonic and migmatitic rocks, mantled by late Carboniferous to Permian non-metamorphic sedimentary and volcanic series, which are in turn unconformably overlain by Mesozoic sedimentary rocks (Fig. 1B, Barfety et al., 2000; Guillot et al., 2009). Based on their structural and petrological differences, the ECMs can be divided into three domains. The easternmost domain consists of Variscan granites and migmatites (Fig. 1B). The central domain, which corresponds to SW Pelvoux, SW Belledonne and SW Aiguilles Rouges, consists of the Chamrousse Ophiolite, amphibolite facies metamorphic rocks, and the Visean volcano-sedimentary series (see details below). The westernmost domain (NW Belledonne) exhibits a micaschist series called the Série Satinée (e.g. Bordet and Bordet, 1963; Fig. 1B).

During the early Jurassic, continental rifting affected Pangea and led to the formation of hemi-grabens resulting in a local tilting of the Paleozoic basement along normal faults (Barfety et al., 1988; Lemoine, 1988). The Miocene deformation is very heterogeneous with localized steeply-dipping brittle-ductile shear zones that accommodated the Alpine NW-SE compression (Bellahsen et al., 2012, 2014, Bellanger et al., 2014, 2015; Marquer et al., 2006). The Miocene deformation is associated with a low-grade metamorphism, with from prehnite-pumpellyite to

greenschist facies conditions (Gratier et al., 1973). Except for this low-grade metamorphism and localized deformation along Alpine shear zones, the evidence of pre-Alpine, i.e., Variscan tectonometamorphic events is well preserved in the Belledonne Massif.

2.2 The main lithotectonic units in the Belledonne Massif

The Belledonne Massif is divided into three tectonic parts delimited by high-angle strike slip faults (Figs. 1B, 2; Barfety et al., 1972, 2000). To the NW, in the External Domain, the Série Satinée is bounded to the east by the Synclinal Median dextral strike-slip Fault (SMF) (Bordet and Bordet, 1963; Simeon, 1979). Based on a structural analysis, Simeon (1979) shows that the SMF records a polyphase history with a late-Variscan dextral strike-slip fault that was reworked by a reverse faulting and then a normal faulting during the Mesozoic and Alpine deformations respectively. The protolith for this series, which consists of alternations of low metamorphic grade quartz-feldspar sandstone and two-mica bearing micaschists, is considered to be a turbidite formation (Bordet and Bordet, 1963). East of the SMF, the Internal Domain of the Belledonne Massif is divided into two parts, on either sides of the Rivier-Belle Etoile fault (RBE, Fig. 1B). The NE part is composed of partly migmatitic volcanoclastic series intruded by Visean granitoids (Barfety et al., 2000; Debon and Lemmet, 1999). Scarce eclogitic relics are documented in the NE Belledonne, with a U-Pb zircon age of 395±2Ma, interpreted as defining the age of the HP event (Paquette et al., 1989). A similar Eo-Devonian HP event is invoked for the eclogites that crop out in the Aiguilles Rouges (Paquette et al., 1989). In the Argentera Massif, the HP event is younger, with Carboniferous ages ranging from 340 to 336 Ma (Rubatto et al., 2010). This contribution focuses on the SW part of the Belledonne Massif (Fig. 2). The following lithological or tectonic units are recognized: i) the Chamrousse ophiolitic complex; ii) the Rioupéroux-Livet volcanosedimentary unit; iii) the Allemont migmatitic unit; and iv) the Taillefer terrigenous-volcanic unit (Ménot, 1988a).

The Chamrousse ophiolitic complex (Bodinier et al., 1981; Carme, 1965a, 1970; Pin and Carme, 1987) consists of a well-preserved kilometer-scale ophiolite that may have formed in a back-arc basin at around 496 Ma (Ménot et al., 1988; Pin and Carme, 1987). Detailed mapping indicates that the ophiolitic succession is tectonically inverted with serpentinized ultramafic rocks that are underlain by gabbros and amphibolites (Bodinier et al., 1981). Pillow lavas, volcanic and sedimentary rocks occupy the lowermost position. The presence of ductile shear zones between each lithological sub-unit attests to the tectonic disruption and inversion of the ophiolitic sequence (Barfety et al., 1972, 1988; Carme, 1965a). A low pressure and high temperature (LP-HT) metamorphism estimated at 0.3-0.4 GPa and 500-600 °C is reported by (Guillot et al., 1992).These authors considered this LP-HT metamorphism to be contemporaneous with a rift-related intra-oceanic deformation defined by the development of NW-SE-trending lineation and top-to the NW shearing.

The Rioupéroux-Livet unit is composed of bimodal magmatic and volcano-sedimentary rocks (Ménot, 1988b). The magmatic portion includes felsic and mafic lavas; the graywackes in the volcanoclastic portion are intruded by trondhjemitic sills. These trondhjemites have been dated at 367-362 Ma by K/Ar on amphibole (Ménot et al., 1985, 1987; Ménot, 1986), and at 367±17 Ma and 352±55 Ma by U-Pb on zircon (Ménot et al., 1985; Ménot, 1988b). The volcano-sedimentary sequence exhibits an alternation of plagioclase-rich leucocratic beds, felsic metavolcanics, metapelites and rare marbles. Towards the east, the metapelitic layers thicken and become more abundant.

The Rioupéroux-Livet unit was interpreted as an active continental margin (Carme and Pin, 1987) whereas Ménot (1987, 1988b) argued for a continental extensional setting with a progressive change from mantle to crustal magmatic sources. An amphibolite facies metamorphism is recorded by garnet-staurolite-bearing micaschists with peak metamorphic P-T conditions of 0.8±0.2 Gpa and 590±60 °C (Fernandez et al., 2002; Guillot and Ménot, 1999).

A near isothermal decompression evolution down to P-T conditions of 0.7±0.2 Gpa and 590±60°C before a late retrogression under greenschist facies conditions is reported (Fernandez et al., 2002; Guillot and Ménot, 1999). In view of the K-Ar dating on amphibolite (Ménot et al., 1987), and the granitoid emplacement ages (Debon et al., 1998), Guillot et al. (2009) considered that the amphibolite facies metamorphism is related to a nappe stacking event that occurred between 341 ± 13 Ma and 324 ± 13 Ma. The metamorphic gap observed between the Chamrousse ophiolitic complex and the Rioupéroux-Livet unit is explained by the thrusting of the former upon the latter along the Rioupéroux thrust (RT, Fig. 2).

East of the Rioupéroux-Livet unit, the *Allemont migmatitic unit* consists of a hundred-meter-thick anatectic zone with garnet-bearing metatexites, migmatitic gneisses and anatectic granites (Fig. 2, Guillot and Ménot, 1999). These rocks were interpreted as being formed during a late Carboniferous to Permian extensional tectonic phase coeval with crustal melting (Fernandez et al., 2002; Guillot and Ménot, 1999). The Rivier-Belle Etoile fault zone truncates the metatexites observed near Allemont, suggesting that their apparent thickness is probably underestimated (Fig. 5A).

The Taillefer unit is composed of terrigenous rocks, dominantly siltstones with graphitic layers, sandstones, conglomerates, and acidic volcanic rocks. On the basis of poorly preserved fossil plant fragments, the Taillefer unit was believed to be upper Visean in age (ca. 330 Ma) (Gibergy, 1968). However, a U/Pb zircon age of 336± 5 Ma was recently obtained for a granitoid intrusion within the Taillefer unit in the Pelvoux massif (Fréville, 2016). The Taillefer unit experienced a greenschist facies metamorphism coeval with ductile deformation (Barfety et al., 1972). The Taillefer unit rocks unconformably overlie the Rioupéroux-Livet unit (Carme, 1965b), and both units were involved in the same tectonic-metamorphic event. On the basis of the geochemical tholeiitic signature with evidence for crustal contamination of the magmatic

rocks, the Taillefer unit was interpreted as a back-arc basin developed on a thin continental crust (Vivier et al., 1987).

As regards the tectonic history, several studies (Fernandez et al., 2002; Guillot et al., 2009; Guillot and Ménot, 2009) lead to the following evolution: (i) an early Devonian nappe emplacement represented in the SW Belledonne by a top-to-the-NNW thrusting related to an early obduction of the Chamrousse ophiolite complex; (ii) a Visean nappe stacking responsible for the back thrusting of the Chamrousse ophiolitic complex onto the Rioupéroux-Livet unit, and the top-to-the-ENE shearing within this unit; and (iii) a Westphalian-middle Stephanian extensional tectonics allowing the emplacement and metamorphism of the Allemont migmatitic unit.

3. Structural analysis

Macro- and microstructural investigations in the southwestern part of the Belledonne Massif enable the recognition of a succession of two main ductile deformation phases, called D_1 and D_2. In what follows the deformation features are described from the top to the bottom of the tectonic pile, and from west to east. Table 1 summarizes the structural features and the tectonic and metamorphic events identified in this study over the southwestern portion of the Belledonne Massif.

3.1 D_1 deformation: Nappe stacking

The main planar fabric of the *Chamrousse ophiolitic complex* is defined as a metamorphic foliation S_1, which mostly parallels the primary bedding, which may correspond to magmatic layering. S_1 strikes N-S to NE-SW and dips mainly toward the west, but E- or SE-vergent post-folial folds may disturb the S_1 dip (Figs. 2, 5, 6). S_1 is superimposed on the deformation related to the rifting event and represented by a NW-SE trending lineation and top-

to-the-NW shearing described by Guillot et al. (1992). Along the tectonic contact between the Chamrousse and Rioupéroux-Livet units (i.e. the RT), and the low angle internal ductile thrust within the Chamrousse unit, S_1 becomes very penetrative and exhibits mylonitic fabrics (Fig. 3A). The S_1 planar fabric comprises an E-W- to NE-SW-trending mineral and stretching lineation L_1 (Fig. 6) that is well exemplified by elongated amphibole needles within amphibolite. Mafic boudins elongated along L_1 are also observed. Intra-folial folds (F_1) with axes parallel to L_1, are also seen. As with S_1, L_1 becomes more pronounced in the mylonitic zones that developed along the internal contacts in the Chamrousse ophiolitic complex, particularly between serpentinite and gabbro. These shear zones suggest a top-to-the-ENE motion (Fig. 3A).

In the western part of the *Rioupéroux-Livet unit*, the structural elements are similar to those described in the Chamrousse ophiolitic unit. The main planar fabric is a metamorphic foliation S_1 that strikes N-S to NE-SW and dips mainly toward the west (Figs. 3B, 3C, 3D, 3E, 5, 6). S_1 exhibits an E-W- to NE-SW-trending L_1 (Fig. 6) that defines the preferential orientation of elongated amphibole needles, biotite aggregates and elongated quartz within amphibolite and metapelite respectively (Fig. 3F). Along the L_1 and within the XZ plane, kinematic indicators observed in the field or in thin sections are in agreement with a top-to-the-E shearing (Figs. 3C, 3D, 7A, 7C).

F_1 isoclinal folds emphasized by the attitudes of several quartz-rich layers within the volcanosedimentary rocks are observed. S_1 and F_1 intrafolial folds strike N-S and dip gently to the west (Figs. 3B, 3D, 6). Furthermore, the D_1 fabric observed in the Rioupéroux-Livet reworked has an earlier bedding, (S_0), preserved as plagioclase-rich leucocratic layers in a few F_1 fold hinges (Figs. 3B, 8A).

In the easternmost part of the Rioupéroux-Livet unit, a D_1 strain gradient is documented by the progressive development of a mylonitic zone at the base of the unit (Fig. 3E, 5). Several

mylonitic bands, moderately westward-dipping (30° - 50°) and a decimeter to several meters thick, exhibit a pervasive E-W trending, stretching lineation (L_1), along which top-to-the-E shear criteria, such as sigmoidal veins, drag folds and sigmoidal blasts are observed (Figs. 3C, 3D, 3E, 7C, 7D). These mylonitic bands correspond to a high-strain zone, approximately 1 km thick, here named the Allemont shear zone (ASZ) (Figs. 2, 5A). Thus along the eastern part of the Belledonne Massif, a D_1 strain gradient increasing from west to east is observed. As described in the next section, the increase in metamorphic grade and the onset of partial melting is consistent with this east-directed strain gradient, which is interpreted here as being related to the D_1 nappe stacking event.

Within the Allemont migmatitic unit the early D_1 structural elements were partially erased during the melting, nevertheless when observed they exhibit the same geometric features as those described within the Rioupéroux-Livet unit. Moreover, the biotite and quartzo-feldspathic leucosomes define a preferred mineral orientation parallel to S_1. In what follows, this planar structure is also considered to be coeval with the S_1 observed in the Rioupéroux-Livet unit.

An early deformation attributed to S_1, characterized by relict N-S-striking and westward dipping foliation, is also observed in the Série Satinée unit (Fig. 6). It is worth noting that the D_1 event described here in several units is not observed in the Taillefer unit (Table 1).

3.2 NW-SE D2 shortening

In the southwestern part of the Belledonne Massif, in both the inner and outer branches, N000°E to N030°E striking, upright or slightly eastward overturned, km-scale F_2 folds are observed (Fig. 2). These structures belong to the D_2 deformation as S_1 is folded along a broad N030°E trending sub-horizontal axis with sub-vertical or steeply westward dipping axial planes (Figs. 2, 4A, 4B, 4C, 6). Commonly, the F_2 long limbs are moderately (20° to 40°) west dipping,

and the short limbs are sub-vertical (Fig. 5). At the centimeter- to decimeter-scale F_2 folds tend to be more upright (Fig. 4A). The D_2 deformation is responsible for a refolding of L_1 in which the initial D_1 E-W trend becomes parallel to a NE-SW direction (Figs. 3F, 8B, 8C). The D_2 linear fabric is dominated by a NE-SW trending, weakly SW plunging L_2 crenulation lineation that parallels the meter-scale F_2 fold axes (Figs. 4D, 6). The L_2 crenulation lineation is observed in the Chamrousse ophiolitic complex, the Rioupéroux-Livet unit and the Taillefer unit (Fig. 4D), as well as in the Série Satinée unit (Fig. 6).

D_2 shearing with opposite kinematics, attested by mm- to cm-scale shear bands is recognized along F_2 flanks (Figs. 4B, 4E, 4F, 7B and 8D). These opposite senses of shear, coeval with F_2 folding, can also be seen at the microscopic scale (Fig. 7B). Owing to the geometry of F_2 folds, with long flanks dipping toward the WNW, the apparent top-to-the-W sense of shear is preponderant (Figs. 4E, 8D). These shear bands are easily observed in the plane perpendicular to the L_2 crenulation lineation (Fig. 8D). The Allemont migmatitic unit is also deformed by the D_2 folding. Asymmetric pockets of melt (Figs. 4B, 4E) and shear bands (Figs. 4B, 4E, 4F) show a top-to-the-NW or top-to-the-SE shearing.

Within the Rioupéroux-Livet unit, S_2 is subvertical and strikes NE-SW (Figs. 4C, 6). The S_2 foliation is mostly observed near the hinge of F_2. S_2 is very penetrative in metapelitic layers and less so in the more competent volcanoclastic layers (Fig 4A, 4C, 8A). In the Rioupéroux-Livet unit near Allemont, a NW-SE-directed D_2 shortening gradient is marked by the tightening of upright folds (Figs. 4A, 5B), and by the development of meter-scale S_2 corridors along which the $S_{0\text{-}1}$ foliation is transposed (Fig. 8C).

Within the Taillefer unit, an S_2 slaty cleavage pervasively develops: it strikes NE-SW and dips steeply, predominantly to the NW. It is well recorded within the black shale sediment but may be observed in the terrigenous and volcanic rocks as well. The elongation of quartz pebbles defines an L_2 stretching lineation with a NE-SW trend and moderate plunge. Since the planar

and linear structures observed in the Taillefer unit exhibit the same orientation as the D_2 structures recognized in the Rioupéroux-Livet unit, they are attributed to the D_2 event (Table 1).

In summary, two main phases of penetrative deformation are easily recognized along the Romanche valley, namely an earlier D_1 deformation event corresponding to an eastward nappe stacking, and a subsequent D_2 deformation event attributed to a general NW-SE-directed shortening.

4. Petrological analysis

Two samples from the Rioupéroux-Livet unit and one from the Allemont migmatitic unit were selected to place thermobarometric constraints on the deformation events described in the previous section. Sample locations are shown in figures 2 and 5. From west to east, the samples are i) a staurolite-garnet micaschist (MCE56Va), sampled near Livet (Figs. 2, 5A); ii) a kyanite-garnet micaschist (MCE240) from the eastern part of the Rioupéroux-Livet unit (Figs. 2, 5A); and iii) a garnet-bearing metatexite (MCE195a) that comes from the Allemont migmatitic unit (Figs. 2, 5A). Electron Microprobe Analyses were performed, using a CAMECA SX100 at the University of Lille, France. Results are presented in Table 2.

4.1 Sample petrography and mineral chemistry

Garnet-kyanite micaschist (MCE240)

Sample MCE240 is a fine-grained micaschist with an S_1 planar fabric defined by the preferred orientation of platy biotite and muscovite grains (Fig. 9A). The S_1 foliation wrapped around inherited mm- to cm-scale lenses displays a garnet + biotite + muscovite + kyanite + albite + plagioclase + quartz assemblage (Fig. 9A). These lenses are devoid of any clear microstructural elements. Garnet appears as fractured mm-sized porphyroblasts. The garnet's chemical

composition ranges from *ca.* Alm_{65}; Py_{06}; Grs_{21} and $Spss_{09}$ in the core to *ca.* Alm_{70}; Py_{10}; Grs_{19} and $Spss_{01}$ in the rim (Table 2). Kyanite grains are mm sized and highly retrogressed, with the development of secondary white mica (Mu2) (Fig. 9A). Plagioclase is homogeneous in composition with Ab_{78-89}. Biotite grains exhibit an average X_{Mg} ranging between 0.42 and 0.45 (Table 2).

Garnet-staurolite micaschist (MCE56va)

The MCE56va rock consists of a fine-grained micaschist with a garnet + staurolite + biotite + muscovite + quartz main assemblage (Fig. 9B). The S_1 planar fabric is defined by the preferred orientation of micas (Fig. 9B). Garnet and staurolite grains appear as mm-sized porphyroblasts with asymmetric quartz pressure shadows indicating a top-to-the-East shearing along the plane parallel to L_1. Garnet porphyroblasts are subhedral, rich in quartz inclusions, and have a homogeneous composition of *ca.* Alm_{80}; Py_{14}; Grs_{6} and $Spss_{004}$. Subhedral staurolites reach 0.5 to 1 mm in size and have X_{Fe} contents ranging from 0.87 to 0.89. Biotite has a variable composition with an X_{Mg} ranging between 0.45 and 0.49 (Table 2).

Garnet-bearing metatexite (MCE195a)

Sample MCE195a consists of an assemblage of garnet, biotite, muscovite, plagioclase, quartz (Fig. 9C) and rare sillimanite (<1%). Platy muscovite and biotite grains define the planar fabric (Fig. 9C). Sillimanite grains oblique to the S_1 foliation suggest late crystallization (see insert in Fig. 9C). Garnet appears as small µm-sized subhedral grains that nucleate around biotite grains (Fig. 9C). Garnet is homogeneous in composition with *ca.* Alm_{75}; Py_{10}; Grs_{03} and $Spss_{10}$. Biotite has an X_{Mg} around 0.46-0.48 (Table 2). The mm-to cm-thick leucocratic layers have a mineral assemblage of quartz, plagioclase, and rod-shaped muscovite grains.

4.2 P-T metamorphic conditions

The P-T metamorphic conditions were obtained from computation of phase diagram sections calculated in the MnO-Na_2O-CaO-K_2O-FeO-MgO-Al_2O_3-SiO_2-H_2O (MnNCKFMASH) system for micaschists. Calculations were performed with Perple_X'6.7.1 (Connolly and Pettrini, 2002; Connolly, 2005) using bulk rock compositions that were obtained by WD-XRF analysis at the University of Lausanne, Switzerland (Table 3). Thermodynamic data for end-members are from the updated version of the internally consistent thermodynamic dataset of Holland and Powell (1998), revised in Coggon and Powell (2002). Solid-solution models and end-member phases considered in the pseudosection calculations are listed in Table 4.

Results for Sample MCE240 are presented on Figure 10. The amount of water used in the P-T pseudosection modeling is determined by the calculation of a T-X_{H2O} pseudosection (X_{H2O} stands for the amount of water in the bulk composition). It appears that H_2O content is the critical parameter influencing the stability of garnet + chlorite *vs* garnet + kyanite assemblages (Fig. 10A). Considering H_2O as a saturated component, the garnet + chlorite assemblage is stable but kyanite is not predicted. The peak temperature equilibrium assemblage observed in the rock sample, i.e., biotite + plagioclase + muscovite + garnet + kyanite + albite + quartz, is predicted to be stable at undersaturated conditions only (Fig. 10A). To estimate the H_2O content we considered the LOI (2.3wt%, corresponding to 0.0127 mol) to represent X_{H2O}=1. The T-X_{H2O} diagram shows that the kyanite-bearing equilibrium is stable for an X_{H2O}=0.6, for T<660°C and P=0.7 GPa. We then used the corresponding molar content (H_20=0.083) to calculate the P-T pseudosection shown in Figure 10B. The predicted P-T fields of the observed main paragenesis (biotite + muscovite + plagioclase + albite + garnet + kyanite + quartz) are predicted to be stable for PT conditions from 310 °C to 450°C and 0.3 GPa to 0.78 GPa, respectively (Fig. 10 B). The chemical composition of the garnet rim and isopleth contouring allow us to refine the P-T conditions to 0.68 ± 0.1 GPa and 427 ± 16 °C (Fig. 10B). The garnet core chemical composition provides prograde P-T estimates at 0.33 ± 0.05 GPa and

370 ± 25°C (Fig. 10). A second P-T pseudosection is proposed, to take into account the garnet fractionation during prograde metamorphism, since it has been demonstrated that 2 vol% of garnet can significantly affect garnet isopleth thermobarometry (Lanari and Engi, 2017) .

Figure 10C shows the P-T pseudosection calculated from a new bulk composition after 5% of garnet fractionation. A point-counting estimation revealed a maximum of 8-10 vol% of garnet in Sample MCE240. However, for the P-T conditions of the garnet core, thermodynamic computation predicts less than 5vol% of garnet (for instance, 1.8 wt% at 0.3GPa and 360°C with a garnet-core composition). We chose to consider a 5% fractionation. Based on this value we recalculated a bulk rock composition minus the contribution of 5vol% of garnet with a core composition, (in wt%) of: SiO2, 65.82; Al2O3, 14.47; Fe2O3, 5.74; MgO, 1.97; CaO, 0.35; Na2O, 1.79, K2O 3.43; TiO2, 0.81; MnO, 0.0; H_20 2.34. The major typology differences between the two P-T pseudsections (Bulk 1 and Bulk 2 (-5%grt)) are shown in figure 10D. First, the removal of 5vol% of garnet lead to a shift to lower temperature of the kyanite-out boundary. Secondly, the biotite + muscovite + plagioclase + albite + garnet + kyanite + quartz stability field area is reduced, with a change in pressure condition from ca. 0.55±0.2 GPa to 0.475±0.1 GPa. The X_{Ca}^{Grt} isopleths are shifted to lower temperatures and pressures. The X_{Mg}^{Grt} isopleth typology remains similar (Fig; 10D). Accordingly, we consider that the best estimation for the peak P-T conditions recorded by sample MCE240 is P=0.535±0.045 GPa and T=427.5±17.5 °C.

For Sample MCE56Va, the P-T diagram was computed with H_2O as a saturated component. In this condition, the pseudosection of Sample MCE56va (Fig. 11A) shows the stability field of biotite + muscovite + garnet + staurolite + quartz + H_2O equilibrium ranging between 0.43 GPa and 0.74 GPa and 575°C and 640°C (Fig. 11A). Isopleth contouring of the chemical compositions of biotite and garnet enable us to refine the P-T conditions to 0.58 ± 0.06 GPa and 608 ± 14 °C (Fig. 11A).

For the migmatite (Sample MCE195a), the water content used in the pseudosection calculation cannot be deciphered solely on the basis of the bulk composition analysis. For high temperature conditions, the amount of water involved was determined via the calculation of a T-X_{H2O} pseudosection, such that the solidus is water-saturated at 0.7 GPa (Figure 11B). Thermodynamic modeling of the migmatitic Sample MCE195a shows a stability field for biotite + muscovite + plagioclase + garnet + quartz + melt ranging between 0.66 GPa and 0.9 GPa and 650°C to 700°C (Fig. 11B). Under these conditions, the volume fraction of melt predicted at the peak conditions by the model is 0.06vol%. Garnet chemical composition constrains the peak P-T conditions to 0.78 ± 0.07 GPa and 680.5 ± 11.5 °C (Fig. 11B).

To sum up, two metamorphic events are documented from these petrological results. The first is characterized by the kyanite-bearing metapelite MCE240, and records a medium pressure – low temperature (MP-LT) metamorphism. The second event corresponds to a medium pressure – high temperature (MP-HT) metamorphism recorded by the staurolite-garnet micaschist MCE56Va and the migmatite MCE195a. The MP-HT conditions are interpreted as those of the D_1 nappe stacking event. Such thermodynamic modeling results are consistent with field observation and argue for an eastward increase in temperature up to partial melting (Fig. 5A).

5. Geochronological constraints

In the SE Belledonne area, radiometric data are rare, and some of them were acquired more than 30 years ago. The advances in analytical techniques and the development of in situ and in-context methods allow us to refine the timing of the evolution of this Variscan segment. In this section zircon and monazite age data from several tectonic units are presented and discussed.

Zircon SIMS U-Pb age of the plagioclase-rich leucocratic sills *in the Rioupéroux-Livet unit*

As mentioned in the previous sections, several plagiogranitic dykes and sills intrude the bimodal volcanclastic rocks of the Rioupéroux-Livet unit. Sample MCE116, collected near Rioupéroux just below the RT, is one of these plagioclase-rich leucocratic sills, (located at 45° 5'17.99"N; 5°53'50.80"E; Fig. 2). This rock comprises an assemblage of quartz and plagioclase with some late chlorite and epidote, developing along fractures from Ca-rich plagioclase, and secondary calcite probably developed during Cenozoic Alpine events. Plagioclase, up to 2-3 mm in size, exhibits a clear oscillatory zoning (Fig 12B). Zircon grains were carefully handpicked under a binocular microscope, placed on an epoxy mount and polished. Sixty zircon grains were selected for SIMS U-Pb analyses, performed at the Institute of Geology and Geophysics of the Chinese Academy of Sciences, Beijing. The Plešovice zircon (Sláma et al., 2008) standard was measured to monitor the accuracy and yielded a concordia age of 335.3 ± 2.5 Ma (N=14, MSWD=0.43), which is in good agreement with the reported ID-TIMS age of 337.1 ± 0.4 Ma (Sláma et al., 2008). The methodology employed is described in Li et al. (2009) and Do Couto et al. (2015). The zircon grains exhibit a well-developed magmatic oscillatory zoning, typical of a magmatic origin (Corfu et al., 2003) (Table 5; Fig. 12C). U and Pb contents range between 70-685 ppm and 4-40 ppm respectively. These zircon grains yield a concordant age of 352 ±1 Ma (N=60; MSWD=0.66) (Fig. 12A). This age is interpreted as the age of magmatic emplacement of the plagioglase-rich sills' protolith.

Detrital zircon ages from the Série Satinée turbidite

Ninety-nine detrital zircon grains extracted from a sandstone of the Série Satinée turbidite (MC5) sampled near the Lac Mort, near Laffrey (45° 2'8.73"N, 5°47'29.48"E, Fig. 2)

were analyzed by LA-ICP-MS at the Institute of Geology and Geophysics of the Chinese Academy of Sciences, Beijing, following the protocol described by Wang et al. (2010).

These zircon grains were carefully handpicked under a binocular microscope, placed on an epoxy mount and polished. The zircons were selected to represent the full variation in shape, color and size of the zircons in the rock sample. In this study, we excluded zircon age analyses with discordances higher than ±10%. The majority of analyses (98 grains) exhibit a main Neoproterozoic peak at ca. 600-645 Ma, along with subordinate peaks at 800, 900, 2100, and 2800 Ma (Fig. 13). The absence of Mesoproterozoic ages is typical of North Gondwana derived materials (Melleton, 2008 and reference therein). The youngest zircon grain yields an age of ca. 463 Ma, providing a maximum estimate for the deposition age of this sandstone in Ordovician times (Table 6; Fig 13).

Detrital zircon ages from the Taillefer conglomerate

One hundred and twelve detrital zircon grains extracted from a conglomerate of the Taillefer unit sampled in the Southern part of Taillefer massif (44°54'35.13"N, 5°56'50.69"E; Figure 1) were analyzed by LA-ICP-MS at the Université Rennes 1 using a ESI NWR193UC Excimer laser system coupled to an Agilent 7700x quadrupole ICP-MS. The analytical protocol may be found in Manzotti et al. (2016) and the analytical conditions in Supplementary Table 1. Along with the unknowns, the Plešovice zircon (Sláma et al., 2008) standard was measured to monitor accuracy and yielded a $^{206}Pb/^{238}U$ concordia age of 336.3 ± 3.3 Ma (N=6, MSWD=0.54), which is in good agreement with the reported ID-TIMS age of 337.1 ± 0.4 Ma (Sláma et al., 2008). In this study, we excluded zircon analyses with a discordance greater than ±10%.

The main population (104 grains) defines an Ordovician peak at ca. 450 Ma and a second major upper Cambrian peak in the 500-550 Ma range. Subordinate peaks at 600-800 Ma, 2100, 2600

and 2900 Ma are also observed (Figure 14). Some Mesoproterozoic ages are also seen. The youngest concordant zircon provides a Devonian age of ca. 395 Ma, implying a post late early Devonian deposit (Table 7, Figure 14).

LA- ICP-MS U-Pb dating of monazite from micaschist in the Rioupéroux-Livet unit

LA-ICP-MS U-Pb analyses on seven monazite grains from a biotite-garnet-staurolite micaschist (MCE56Va; 45° 6'38.81"N, 5°56'3.63"E, Fig. 2), were carried out at the Université de Montpellier II following the procedure described in Bruguier et al. (2009). Analyses were conducted on a polished thin section (Supplementary Table 2), thereby preserving the textural context of the dated grains. The dated monazite grains are elongated in the metamorphic foliation (S_1) of the micaschist, and they show no chemical zoning (Fig 15 A, 15B). Two slightly concordant analyses and 5 discordant analyses, with common lead content, are spread along a discordia curve line representing a mixing between radiogenic and common with theoretical common Pb values. In a Tera-Wasserburg concordia diagram, a regression through the data points yields an intercept age of 337 ± 7 Ma (MSWD=0.17).

The textural relationships, as well as grain contacts between monazite, biotite, staurolite and the development of monazite grains along pressure shadows, indicate that the crystallization of monazite took place during amphibolite facies metamorphism (Fitzsimons et al., 2005). We therefore consider that the age of 337 ± 7 Ma obtained corresponds to the D_1 tectonometamorphic event (Table 8; Fig. 15C).

6. Discussion

6.1 *Tectonometamorphic evolution*

Two metamorphic stages are evident from our thermobarometrical work. MP-LT metamorphism (Mx) is recorded in a lens of kyanite-bearing micaschist from the Rioupéroux-Livet unit. The P-T estimates indicate a prograde evolution from 0.33 ± 0.05 Gpa and 370 ± 25°C up to 0.535 ± 0.0.045 Gpa and 427.5 ± 17.5°C (Fig. 16). The strain fabric associated with the Mx kyanite-bearing assemblage remains unknown owing to the intense D_1 and D_2 overprint. Nevertheless, an early MP-LT Dx/Mx tectonometamorphic event has already been described by Guillot and Ménot (1999). We suggest that the Dx/Mx event documented here may correspond to the thrusting at the mid-crustal level of the Chamrousse ophiolite upon the Rioupéroux-Livet unit, from west to wast.

The second metamorphic event (M_1) is recorded in the staurolite-bearing micaschist from the Rioupéroux-Livet unit, with peak conditions of 0.58 ± 0.06 GPa and 608 ± 14°C. In agreement with Guillot and Ménot (1999), M_1 is interpreted as coeval with the top-to-the-E nappe stacking event responsible for the penetrative D_1 fabric (S_1, L_1, F_1) observed in the Chamrousse ophiolitic complex, the Rioupéroux-Livet unit and the Allemont migmatitic unit. It is worth noting that the Série Satinée unit recorded a pre-D_2 event, which could correspond to the D_1 event (Simeon, 1979). Absence of the D_1 deformation in the Taillefer unit is in agreement with its post-D_1 (Visean) deposition age, as proposed by Gibergy (1968). In our interpretation, the D_1/M_1 event is the main tectonometamorphic phase experienced by the SE part of the Belledonne Internal Domain, whereas it was previously considered to be a back-thrusting event (Guillot and Ménot, 1999). Previous works (Fernandez et al., 2002; Guillot et al., 2009; Guillot and Ménot, 2009) proposed a top-to-the-NW shearing event responsible for the nappe stacking in the Chamrousse ophiolite, followed by a back thrusting of this realm. However, recent studies show that during the Alpine orogeny the deformation was partially accommodated in the Variscan basement along shortening structures characterized by east-dipping Alpine shear zones with top-to-the-NW kinematics (Bellahsen et al., 2014; Bellanger

et al., 2014, 2015). Accordingly, we argue that the top-to-the-W shear bands are related to the Alpine events and that an early NW-directed nappe stacking event is unlikely.

The M_1 event recorded in the Rioupéroux-Livet unit corresponds to the partial melting of the Allemont unit micaschist, under the P-T conditions of 0.78 ± 0.07 GPa and 680.5 ± 11.5°C obtained from a metatexite (Fig. 16). On the basis of the apparent top-to-the-W shear bands in the Allemont and Rioupéroux-Livet units, a southwestward extensional event has been invoked to accommodate the exhumation of the Allemont migmatitic unit (Fernandez et al., 2002; Guillot et al., 2009; Guillot and Ménot, 2009, 1999). Based on our structural analysis, we suggest that the top-to-the-W shear bands are instead the result of the D_2 shortening event developed in the west-dipping limbs of the F_2 folds. We also documented the D_2 as a pervasive event corresponding to a bulk NE-SW shortening observed in the Série Satinée unit of the western Belledonne, the Chamrousse ophiolitic complex, and the Rioupéroux-Livet, Allemont migmatitic and Taillefer units. D_2 is also responsible for the partial reorientation of the E-W trending L_1 lineation into a N30-trending direction.

In previous studies, the D_2 tectonometamorphic event was poorly documented and more commonly associated with the nappe stacking event, with the L_2 crenulation lineation interpreted as the result of interference between D_1 and an earlier west-directed deformation phase (Fernandez et al., 2002; Guillot et al., 2009). The N30-trending stretching lineation corresponding to the reoriented L_1, was previously interpreted as related to late dextral strike slip shearing along the East Variscan Shear Zone (Guillot et al., 2009). Moreover, the petrologic analysis, as well as the age of the equivalent unit in the Pelvoux massif (330 ± 3 Ma, (Fréville, 2016)) shows that the migmatization that occurred at the end of the prograde M_1 metamorphism, was contemporaneous with the syn-D_1 crustal thickening event. We therefore prefer to interpret the migmatization in the Allemont migmatitic unit as the result of syn-collisional prograde

metamorphism rather than as the expression of a late Carboniferous extensional event (Fernandez et al., 2002; Guillot et al., 2009; Guillot and Ménot, 1999, 2009).

In agreement with previous petrological studies that documented the presence of sillimanite in the Allemont unit (Guillot and Ménot, 1999), our results support an eastward temperature increase, reaching its climax at the base of the nappe pile. Although not observed during our study, cordierite has been reported in the Allemont migmatitic unit and interpreted as coeval with the deformation responsible for the shear band development (Guillot and Ménot, 1999). However, the crystallization of cordierite, unambiguously coeval with a late increment of the D_2 event, took place during the exhumation of the migmatite, but this might also have occurred during bulk shortening.

6.2 Timing of the tectonic, magmatic and metamorphic events

The absolute timing of the tectonometamorphic events is poorly documented, in particular for the early MP-LT event. Nevertheless, the Dx event might be bracketed between approximately. 500 Ma and 355 Ma, corresponding to the age of the Chamrousse ophiolitic complex and the age of the bi-modal magmatism of the Rioupéroux-Livet unit respectively. Based on hornblende $^{40}Ar/^{30}Ar$ dating from amphibolite at the base of the ophiolitic nappe, Guillot et al. (2009) proposed an age of ca. 376 ± 7 Ma for the Dx event.

The absolute ages of the D_1 and D_2 events remain undocumented. Nevertheless, considering the K-Ar dating on amphibolite (Ménot et al., 1987) and the granite emplacement age (Debon et al., 1998) that postdate the D_1 phases, Guillot et al. (2009) considered that the nappe stacking event occurred between 341 ± 13 Ma and 324 ± 13 Ma. In our study, the monazite age from the staurolite-bearing micaschist defines the age of prograde metamorphism (M_1) at 337 ± 7 Ma, coeval with the nappe stacking event (D_1).

The deposition location, the deposition age and the deformation age of the Taillefer unit within the nappe pile remain uncertain. As shown above, this unit was assumed to be Visean in age, and was interpreted as being unconformably deposited upon the ophiolitic complex and the Rioupéroux-Livet unit (Carme, 1965a, 1965b; Gibergy, 1968). The Taillefer's sedimentary rocks may have been deposited during a Visean extensional phase (Guillot et al., 2009). However, no Visean extensional features have been recognized in the SW Belledonne area. Furthermore, the absence of detrital Carboniferous zircon in the Taillefer conglomerates (Fig. 14) is not in agreement with the development of any rift-related basin since volcanic zircon clasts would be expected there. Moreover, a recent study in the Pelvoux area showed that the Taillefer unit is intruded by a Carboniferous granitoid emplaced at 336 ± 5 Ma (U/Pb, zircon, Fréville, 2016). These new data imply that the Taillefer unit was already emplaced on the top of the nappe pile during the D_1 event, before this granitoid intrusion. We therefore propose that the Taillefer unit may correspond to a thrust sheet emplaced during the late stage of the D_1 event. Finally, the D_2 event occurred during the late Carboniferous (i.e., 330-300 Ma), which is in agreement with the ages of 330 Ma and 325 Ma already proposed by Guillot et al. (2009) and Guillot and Ménot (2009)

It was previously proposed that the nappe stacking event was followed by the tectonic juxtaposition of the Série Satinée unit and the Eastern Domain along the SMF between 305 and 270 Ma, in response to large displacements accommodated by the East Variscan Shear Zone (Guillot et al., 2009; Guillot and Ménot, 2009). Nevertheless, if the upright folding experienced by the Série Satinée is the same as the D_2 deformation in the Internal Domain, the Série Satinée unit must have reached its present location before the onset of the D_2 event (Late Carboniferous). Assuming that the Série Satinée unit experienced the D_1 event implies that this unit was already in its present position before the D_1 event, which occurred at *ca*. 340 Ma, and it should therefore have recorded the MP-LT Mx metamorphism. If the Série Satinée unit was

already in its present location before the Visean, then the Late Carboniferous EVSZ cannot account for the position of this part of the Variscan basement as previously proposed (Corsini and Rolland, 2009; Guillot et al., 2009; Guillot and Ménot, 2009; Padovano et al., 2012).

An interpretative tectonic scenario is proposed in Figure 17, which presents the succession of deformation events and related P-T paths from 400 to 300 Ma:

(1) From *ca.* 400 Ma to 380 Ma, the westward subduction of the Chamrousse oceanic domain was responsible for the eclogite that crops out in the NE Belledonne (Fig. 17A).

(2) Between *ca.* 380 Ma and *ca.* 360 Ma a slice of the oceanic domain was overthrust towards the east, forming the Chamrousse ophiolitic nappe. This corresponds to the Dx tectonic event, which is responsible of the MP-LT metamorphism recorded in the Rioupéroux-Livet unit (Fig. 17B).

(3) From *ca.* 360 Ma to *ca.* 350 Ma, the Rioupéroux-Livet magmatic rocks were emplaced as sill intrusions into the thinning crust during rifting. We have as yet no reliable evidence allowing us to identify the cause of rifting. The age of the Rioupéroux-Livet unit was previously considered to be 367-362 Ma based on K/Ar dating on amphibole and 367 ± 17 Ma and 352 ± 55 Ma by the U/Pb method on zircon (Ménot, 1986; Ménot et al., 1985, 1987, 1988). In agreement with Ménot (1986), the zircon ages obtained in this study suggest that the Rioupéroux-Livet bimodal magmatism took place during the Tournaisian at 352 ± 1 Ma. In this interpretation we suggest that the Taillefer volcano-clastic sedimentary rocks were deposited at that time (Fig. 17C).

(4) From *ca.* 350 to *ca.* 330 Ma, the D_1 event was responsible for nappe stacking and crustal thickening that lead to MP-HT metamorphism. Partial melting of the deep crust proceeded from late prograde metamorphic evolution (Fig. 17D). As argued above, the thrusting of the Taillefer unit toward the east may have occurred during the late-D_1 period.

(5) From 330 to 310 Ma, the D_1 tectonic pile was folded by the D_2 horizontal NW-SE shortening (Fig. 17E). The D_2 deformation may have occurred during peak temperature and retrograde evolution. One may consider that the transition from D_1 to D_2 results from progressive deformation causing overlap between late-D_1 and early-D_2 structures.

6.3 Comparison with some neighboring Variscan domains.

The major portion of the ECMs consists of magmatic rocks and granitoids especially in the easternmost domain (Fig. 1). Early Paleozoic ophiolites, such as the Chamrousse examples, are not recognized in other parts of the ECMs, thus, a direct comparison between the SW part of the Belledonne Massif and the Eastern domain is not straightforward. Nevertheless, the SW part of the Aiguilles Rouges Massif displays some lithological and structural features similar to those described here in the Belledonne Massif. Three units are recognized in the SW section of the Aiguilles Rouges Massif (Dobmeier, 1998), These are: (i) a Visean unit made up of metagraywackes and metavolcanites that can be compared to the Taillefer unit; (ii) greenschist and amphibolite facies metamorphic units composed of micaschists and epidote-amphibolites, comparable to the Rioupéroux-Livet unit; and (iii) a gneissic unit with incipient traces of partial melting. These units reveal a tectonometamorphic evolution similar to that of the SW Belledonne Massif with an east-directed thrusting event that emplaced the greenschist and amphibolite facies metamorphic units upon the migmatitc gneissic unit. As for the Rioupéroux-Livet unit, this nappe stacking event is coeval with similar metamorphic PT conditions (0.65 GPa and 600 °C) dated at *ca.* 331-337 Ma (Dobmeier, 1998; Von Raumer et al., 1999). This event would probably correspond to the D_1 event recorded in the SW part of the Belledonne Massif. After the thrusting of the Visean metagraywacke and metavolcanite unit (similar to the Taillefer unit), an E-W bulk shortening event is reported (Von Raumer et al., 1999) that might correspond to the D_2 event recorded in the Belledonne Massif.

To the south, in the Argentera Massif (Fig. 1), in spite of the recognition of HP metamorphic rocks and migmatites (Compagnoni et al., 2010; Paquette et al., 1989; Rubatto et al., 2010), the Variscan deformation sequence is not clearly identified, owing to a strong Alpine overprint. Nonetheless, recent U-Pb geochronological studies argue for a Carboniferous HP metamorphism recorded by zircons dated at 340.7 ± 4.2 Ma and 336.3 ± 4.1 Ma, within HP granulites that recorded peak PT conditions of *ca.* 1.4 GPa and 735 ± 15 °C (Ferrando et al., 2008; Rubatto et al., 2010). These Carboniferous ages in the Argentera Massif are in agreement with the D_1/M_1 event reported in the Belledonne Massif and can be related to the same crustal thickening.

In the Maures Massif, a polyphase synmetamorphic deformation was documented in the mid-1960s (e.g. Arthaud et al., 1966; Oliot et al., 2015 and enclosed references). It comprises a first top-to-the-W shearing that appears to be the main tectonic event, followed by a back-folding event. Although the same tectonic succession is reported with nappe stacking followed by folding, the lithological and structural correlation between the Belledonne and Maures massifs cannot be unambiguously confirmed.

Farther south, in Variscan Corsica, a northern domain (in current geographic coordinates) characterized by gneisses and amphibolites (partly retrogressed from eclogitic metagabbros) experienced a top-to-the-NE ductile shearing coeval with an MP-MT metamorphism (Faure et al., 2014). This tectonic event could be related to the D_1 nappe stacking event described in the SW Belledonne Massif.

At a larger scale, on the basis of a recent review (Lardeaux et al., 2014), a tentative first-order comparison of the tectonometamorphic evolution of the Belledonne Massif and other Variscan massifs, such as the French Massif Central, Vosges, and Bohemian Massifs could be suggested. The Carboniferous evolution of the Belledonne Massif described in this review may exhibit certain similarities with the tectonometamorphic history recognized in the Moldanubian zone

of the Variscan belt, for instance: i) the formation of a bimodal magmatism similar to that of the Rioupéroux-Livet unit; ii) a collisional phase coeval with an MP-HT metamorphism M_1; and iii) the Visean unconformity of the volcanosedimentary unit similar to that of the Taillefer unit. However, several lines of evidence argue against simple correlations. In particular, the bimodal magmatism of the Rioupéroux Livet unit, dated at 355 ± 1 Ma, is younger than other bimodal magmatic domains, such as the Brévenne unit in the French Massif Central, which is dated at 366 ± 5 Ma (Pin and Paquette, 1997). Also, the Brévenne unit is interpreted as a back-arc basin (Faure et al., 1997, 2009) while the geodynamic setting of the Rioupéroux-Livet unit is not yet settled. Moreover, on the basis of similar P-T conditions, the reported age of *ca.* 337 Ma in the Belledonne Massif, which corresponds to the D_1 nappe stacking event, might be compared to the D_2 event in the French Massif Central (Faure et al., 2005, 2009). However, the D_2 event in the French Massif Central occurred during late Devonian to early Carboniferous time, i.e., 20 Ma before the main D_1 tectonometamorphic event in the Belledonne Massif.

Based on similar lithology and age, a parallel can be made between the Taillefer unit of the Belledonne Massif and the Visean "Tufs Antracifères" series that crops out in the NE part of the French Massif Central and in the southern Vosges Massif. However, because of the lack of geochemical data on the Taillefer's sedimentary rocks, an unambiguous correlation of this unit with the Tufs Anthracifères series remains tentative for now. Concerning the possible relationships between the Belledonne Massif and the Vosges and Bohemian Massifs, further investigations are needed.

7. Conclusion

The SW part of the Variscan Belledonne Massif recorded three tectonometamorphic events, identified as Dx, D_1 and D_2 (Table. 1). The Dx event corresponds to the eastward thrusting of

the Chamrousse ophiolitic complex onto the Rioupéroux-Livet unit, causing an LT-MP metamorphism at 0.535 ± 0.045GPa and 427.5 ± 17.5 °C (Mx). The Dx event may have occurred before 360 Ma. The bimodal magmatism of the Rioupéroux-Livet unit, occurred at 352 ± 1 Ma. The main synmetamorphic deformation event D_1 occurred at 337 ± 7 Ma with peak metamorphic conditions of 0.58 ± 0.06 GPa and 608 ± 14 °C. D1 corresponds to an eastward nappe stacking event that transported the Chamrousse ophiolitic complex onto the Rioupéroux-Livet unit. The partial melting at the base of the nappe pile gave rise to the Allemont migmatite, developed at 0.78 ± 0.07 GPa and 680.5 ± 11.5 °C. During the late Visean (330-325 Ma), volcanites, sandstone and conglomerate of the Taillefer unit were thrust onto the previously deformed units (Table 1). Subsequently, the D_2, NW-SE bulk shortening event, characterized by folding of the S_1 foliation, and development of the NE-SW L_2 crenulation, affected all units, including the Cambro-Ordovician flysch unit (the Série Satinée).

8. Acknowledgments

The authors thank ISTO, BRGM, the Laboratoire Chrono-Environnement, and the Observatoire des Sciences de l'Univers en Région Centre for their financial support. We also gratefully acknowledge Pierre Lanarie and anonymous reviewers for their constructive suggestions. We strongly appreciate the English review of this contribution from J.V. Guy-Bray.

References

Arthaud, F., Mattauer, M., Proust, F., 1966. La structure et la microtectonique dans les nappes hercyniennes de la Montagne noire, in: Etages Tectoniques. Colloque de Neuchatel.

Autran, A., Cogné, J., 1980. La zone interne de l'orogène varisque dans l'ouest de la France et sa place dans le developpement de la chaine hercynienne. Géologie Eur. 26° CGI Paris Mém. BRGM 108, 90–111.

Bard, J.P., Burg, J.., Matte, P., Ribeiro, A., 1980. La chaine hercynienne d'Europe occidentale en termes de tectonique des plaques. Géologie Eur. 26° CGI Paris Mém. BRGM 108, 233–246.

Barfety, J.C., Bordet, P., Carme, F., Debelmas, J., Meloux, M., Montjuvent, G., Sarrot-Reynaud, J., 1972. Notice feuille de Vizille, 1/50000, 797.

Barfety, J.C., Gidon, M., Ménot, R.-P., Debon, F., Pêcher, S., Guillot, S., Fourneaux, J.C., Gamond, J.-F., 2000. Notice feuille de Domène, 1/50000, 773.

Barfety, J.C., Montjuvent, G., Pécher, A., Carme, F., 1988. Notice feuille de La Mure, 1/50000, 821.

Bellahsen, N., Jolivet, L., Lacombe, O., Bellanger, M., Boutoux, A., Garcia, S., Mouthereau, F., Le Pourhiet, L., Gumiaux, C., 2012. Mechanisms of margin inversion in the external Western Alps: Implications for crustal rheology. Tectonophysics 560–561, 62–83. https://doi.org/10.1016/j.tecto.2012.06.022

Bellahsen, N., Mouthereau, F., Boutoux, A., Bellanger, M., Lacombe, O., Jolivet, L., Rolland, Y., 2014. Collision kinematics in the western external Alps. Tectonics 33, 2013TC003453. https://doi.org/10.1002/2013TC003453

Bellanger, M., Augier, R., Bellahsen, N., Jolivet, L., Monié, P., Baudin, T., Beyssac, O., 2015. Shortening of the European Dauphinois margin (Oisans Massif, Western Alps): New insights from RSCM maximum temperature estimates and 40Ar/39Ar in situ dating. J. Geodyn. 83, 37–64. https://doi.org/10.1016/j.jog.2014.09.004

Bellanger, M., Bellahsen, N., Jolivet, L., Baudin, T., Augier, R., Boutoux, A., 2014. Basement shear zones development and shortening kinematics in the Ecrins Massif, Western Alps. Tectonics 33, 84–111. https://doi.org/10.1002/2013TC003294

Bodinier, J.L., Dupuy, C., Dostal, J., Carme, F., 1981. Geochemistry of Ophiloites from Chamrousse Complexe (Belledonne Massif, Alps). Contrib Miner. Pet. 78, 379–388.

Bordet, P., Bordet, C., 1963. Belledonne-Grande Rousses et Aiguilles Rouges Mont Blanc: quelques données nouvelles sur leurs rapports structuraux. -Livre à la mémoire du professeur Fallot.-. Mém. Hors Sér. Société Géologique Fr. 1, 309–316.

Bruguier, O., Hammor, D., Bosch, D., Caby, R., 2009. Miocene incorporation of peridotite into the Hercynian basement of the Maghrebides (Edough massif, NE Algeria): Implications for the geodynamic evolution of the Western Mediterranean. Chem. Geol. 261, 172–184. https://doi.org/10.1016/j.chemgeo.2008.11.016

Carme, F., 1970. Age briovérien probable de la majeure partie des séries supposées dévono-dinantiennes et existence d'un cycle ororgénique anté-hercynien, sans doute cadomien, dans la chaîne de Belledonne (Alpes Française). C R Acad Sc Paris 271, 631–633.

Carme, F., 1965a. Sur deux formations, d'origine volcanique, des schistes cristallins anté-houillers de la chaîne de Belledonne (Alpes Francaise). C R Acad Sc Paris 260, 6401–6404.

Carme, F., 1965b. Existence de deux formations détritique remarquables dans les schistes cristallins anté-houiller du Taillefer (chaîne de Belledonne Alpes françaises). C R Acad Sc Paris 260, 6656–6659.

Carme, F., Pin, C., 1987. Vue d'ensemble sur le magmatisme pré-orogénique et l'évolution métamorphique et tectonique varisque dans le Sud de la chaîne de Belledonne (Massifs Cristallins Externes, Alpes francaises). Comptes Rendus Accadémie Sci. Sér. II 304, 1177–1180.

Coggon, R., Holland, T.J.B., 2002. Mixing properties of phengitic micas and revised garnet-phengite thermobarometers. J. Metamorph. Geol. 20, 683–696. https://doi.org/10.1046/j.1525-1314.2002.00395.x

Compagnoni, R., Ferrando, S., Lombardo, B., Radulesco, N., Rubatto, D., 2010. Paleo-European crust of the Italian Western Alps: Geological history of the Argentera Massif and comparison with Mont Blanc-Aiguilles Rouges and Maures-Tanneron Massifs. J. Virtual Explor. 36. https://doi.org/10.3809/jvirtex.2010.00228

Connolly, J.A.., 2005. Computation of phase equilibria by linear programming: A tool for geodynamic modeling and its application to subduction zone decarbonation. Earth Planet. Sci. Lett. 236, 524–541.

Connolly, Pettrini, K., 2002. An automated strategy for calculation of phase diagram sections and retieval of rock properties as a function of physical conditions. J. Metamorph. Geol. 20, 697–708.

Corfu, F., Hanchar, J.M., Hoskin, P.W.O., Kinny, P., 2003. Atlas of Zircon Textures. Rev. Mineral. Geochem. 53, 469–500. https://doi.org/10.2113/0530469

Corsini, M., Rolland, Y., 2009. Late evolution of the southern European Variscan belt: Exhumation of the lower crust in a context of oblique convergence. Comptes Rendus Geosci. 341, 214–223.

Debon, F., Guerrot, C., Ménot, R.P., Vivier, G., Cocherie, A., 1998. Late variscan granites of the Belledonne massif (French Western Alps): an Early Visean magnesian plutonism. Schweiz Miner. Petrogr Mitt 78, 67–85.

Debon, F., Lemmet, M., 1999. Evolution of Mg/Fe Ratios in Late Variscan Pultonic Rocks from the External Crystalline Massif of the Alps (France, Italy, Switzerland). J. Petrol. 40, 1151–1185.

Do Couto, D., Faure, M., Augier, R., Cocherie, A., Rossi, P., Li, X.-H., Lin, W., 2015. Monazite U–Th–Pb EPMA and zircon U–Pb SIMS chronological constraints on the tectonic, metamorphic, and thermal events in the inner part of the Variscan orogen, example from the Sioule series, French Massif Central. Int. J. Earth Sci. https://doi.org/10.1007/s00531-015-1184-0

Dobmeier, C., 1998. Variscan P-T deformation paths from the southwestern Aiguilles Rouges massif (External massif, western Alps) and their implication for its tectonic evolution. Int. J. Earth Sci. 87, 107–123.

Faure, M., Lardeaux, J.-M., Ledru, P., 2009. A review of the pre-Permian geology of the Variscan French Massif Central. Comptes Rendus Geosci. 341, 202–213.

Faure, M., Leloix, C., Roig, J.-Y., 1997. L'Evolution polycyclique de la chaine hercynienne. Bull. Soc. Geol. Fr. 168, 695–705.

Faure, M., Mezeme, E.B., Duguet, M., Cartier, C., J.Y. Talbot, 2005. Paleozoic tectonic evolution of medio-europa from the example of the french massif central and massif armoricain. J. Virtual Explor. 19, Paper 5.

Faure, M., Rossi, P., Gaché, J., Melleton, J., Frei, D., Li, X., Lin, W., 2014. Variscan orogeny in Corsica: new structural and geochronological insights, and its place in the Variscan geodynamic framework. Int. J. Earth Sci. 103, 1533–1551.

Fernandez, A., Guillot, S., Ménot, R.P., Ledru, P., 2002. Late Paleozoic polyphased tectonics in the SW Belledonne massif (external crystalline massifs, French Alps). Geodin. Acta 15, 127–139.

Ferrando, S., Lombardo, B., Compagnoni, R., 2008. Metamorphic history of HP mafic granulites from the Gesso-Stura Terrain (Argentera Massif, Western Alps, Italy). Eur. J. Mineral. 20, 777–790. https://doi.org/10.1127/0935-1221/2008/0020-1891

Fitzsimons, I.C.W., Kinny, P.D., Wetherley, S., Hollingsworth, D.A., 2005. Bulk chemical control on metamorphic monazite growth in pelitic schists and implications for U-Pb age data. J. Metamorph. Geol. 23, 261–277. https://doi.org/10.1111/j.1525-1314.2005.00575.x

Franke, W., 2000. The mid-European segment of the Variscides: tectonostratigraphic units, terrane boundaries and plate tectonic evolution. Geol. Soc. Lond. Spec. Publ. 179, 35–61.

Fréville, K., 2016. L'orogenèse Varisque dans les massifs cristallins externes de Belledonne et du Pelvoux (Alpes occidentales françaises). Rôle de la fusion partielle et du plutonisme dans la structuration de la croûte continentale. Université d'Orléans.

Gibergy, P., 1968. Découverte de “grès à trous” renfermant des schistes noirs de Valbonnais (série cristallophyllienne des Massifs Cristallins Externes dans les Alpes française). C R Acad Sc Paris 267, 1251–1254.

Gratier, J.-P., Lejeune, B., Vergne, J.L., 1973. Etude des déformations de la couverture et des bordures sédimentaires des massifs cristallins externes de Belledonne,des Grandes Rousses et du Pelvoux (depuis Les Aravis jusqu’à La région de Remollon). Alpes françaises (phdthesis). Université Joseph-Fourier - Grenoble I.

Guillot, S., di Paola, S., Ménot, R.-P., Ledru, P., Spalla, M., Gosso, G., Schwartz, S., 2009. Suture zones and importance of strike-slip faulting for Variscan geodynamic reconstructions of the External Crystalline Massifs of the western Alps. Bull Soc Géol Fr. 180, 483–500.

Guillot, S., Ménot, R.P., 2009. Paleozoic evolution of the External Crystalline Massifs of the Western Alps. C R Geosci. 341, 253–265.

Guillot, S., Ménot, R.P., 1999. Nappe stacking and first evidence of late Variscan extension in the Belledonne Massif (External Crystalline Massifs, French Alps). Geodin. Acta 12, 19–111.

Guillot, S., Ménot, R.P., Lardeaux, J.M., 1992. Tectonique intra-oceanique distensive dans l’ophiolite paleozoique de Chamrousse (Alpes occidentales). Bull. Soc. Geol. Fr. 163, 229–240.

Holland, T.J.B., Powell, R., 1998. An internally consistent thermodynamic data set for phases of petrological interest. J. Metamorph. Geol. 16, 309–343. https://doi.org/10.1111/j.1525-1314.1998.00140.x

Lanari, P., Engi, M., 2017. Local Bulk Composition Effects on Metamorphic Mineral Assemblages. Rev. Mineral. Geochem. 83, 55–102. https://doi.org/10.2138/rmg.2017.83.3

Lardeaux, J.M., Schulmann, K., Faure, M., Janou ek, V., Lexa, O., Skrzypek, E., Edel, J.B., tipska, P., 2014. The Moldanubian Zone in the French Massif Central, Vosges/Schwarzwald and Bohemian Massif revisited: differences and similarities. Geol. Soc. Lond. Spec. Publ. 405, 7–44. https://doi.org/10.1144/SP405.14

Lemoine, M., 1988. Des nappes embryonnaires aux blocs basculés: évolution des idées et des modèles sur l'histoire mésozoïque des Alpes occidentales. G-Alp. 8, 787–797.

Li, X.-H., Liu, Y., Li, Q.-L., Guo, C.-H., Chamberlain, K.R., 2009. Precise determination of Phanerozoic zircon Pb/Pb age by multicollector SIMS without external standardization: MULTICOLLECTOR SIMS ZIRCON Pb/Pb DATING. Geochem. Geophys. Geosystems 10, n/a-n/a. https://doi.org/10.1029/2009GC002400

Manzotti, P., Ballèvre, M., Poujol, M., 2016. Detrital zircon geochronology in the Dora-Maira and Zone Houillère: a record of sediment travel paths in the Carboniferous. Terra Nova.

Marquer, D., Calcagno, P., Barfety, J.C., Baudin, T., 2006. 3D modeling and kinematics of the external zone of the French Western Alps (Belledonne and Grand Chatelard Massifs, Maurienne Valley, Savoie). Eclogae Geol Helv 99, 211–222.

Matte, P., 2007. Variscan thrust nappes, detachment, and strike-slip faults in the French Massif Central: Interpretation of lineations. Geol. Soc. Am. Memoire 200, 391–402.

Matte, P., 1986. Tectonics and plate tectonics model for the variscan belt of Europe. Tectonophysics 126, 329–374.

Melleton, J., 2008. Continental crust recycling in the variscan orogen by zircon inheritance investigation (U-Pb in situ measurements by LA-MC-ICPMS) (Theses). Université d'Orléans.

Ménot, R.-P., 1988a. An overview of the geology of the Belledonne Massif (External Crystalline Massifs of western Alps). Schweiz Miner. Petrogr Mitt 70, 33–53.

Ménot, R.-P., 1988b. Magmatisme paléozoïque et structuration carbonifère du massif de Belledonne (Alpes françaises). Contraintes nouvelles pour les schémas d'évolution de la chaîne varisque Ouest-Européenne (Mémoire et doccuments du centre armoricain d'étude structural des socles). Rennes.

Ménot, R.P., 1987. Magamtisme paléozoïques et structuration carbonifère de massif de Belledonne (Alpes Française). Contraintes nouvelles pour le schémas d'évolution de la chaîne Varisque ouest-européenne. Université de Rennes.

Ménot, R.-P., 1986. Les formations plutono-volcaniques dévoniennes de Rioupéroux-Livet (massifs cristallins externes des Alpes françaises) : nouvelles définitions lithostratigraphique et pétrographique. Schweiz. Miner. Petrog Mitteilungen 66, 229–258.

Ménot, R.-P., Bonhomme, M.G., Vivier, G., 1987. Structuration tectono-métamorphique carbonifère dans le massif de Belledonne (Alpes occidentales françaises) : apport de la géochronologie K/Ar des amphiboles. Schweiz. Miner. Petrog Mitteilungen 67, 273–284.

Ménot, R.-P., Peucat, J.-J., Piboule, M., Scarenzi, D., 1985. Cambro-Ordovician age for the ophiolitic complex of Chamrousse-Tabor (Belledonne massif, french external alpine domain. Ofioliti 10, 527.

Ménot, R.-P., Peucat, J.J., Scarenzi, D., Piboule, M., 1988. 496 My age of plagiogranites in the Chamrousse ophiolite complex (external crystalline massifs in the French Alps): evidence of a Lower Paleozoic oceanization. Earth Planet. Sci. Lett. 88, 82–92. https://doi.org/10.1016/0012-821X(88)90048-9

Oliot, E., Melleton, J., Schneider, J., Corsini, M., Gardien, V., Rolland, Y., 2015. Variscan crustal thickening in the Maures-Tanneron massif (South Variscan belt, France): new in situ monazite U-Th-Pb chemical dating of high-grade rocks. Bull. Société Géologique Fr. 186, 145–169. https://doi.org/10.2113/gssgfbull.186.2-3.145

Padovano, M., Elter, F.M., Pandeli, E., Franceshelli, M., 2012. The East Variscan Shear Zone: new insights into its role in the Late Carboniferous collision in southern Europe. Int. Geol. Rev. 54, 957–970.

Paquette, J.-L., Ménot, R.-P., Peucat, J.-J., 1989. REE, Sm-Nd and U-Pb zircon study of eclogites from the Alpine External Massifs (Western Alps)" evidence for crustal contamination. Earth Planet. Sci. Lett. 96, 181–198.

Paris, F., Robardet, M., 1990. Early Palaeozoic palaeobiogeography of the Variscan regions. Tectonophysics 1977, 193–213.

Pin, C., Carme, F., 1987. A Sm-Nd isotopic study of 500 Ma old oceanic crust in the Variscan belt of Western Europe: the Chamrousse ophiolite complex, Western Alps (France). Contrib. Mineral. Petrol. 96, 406–413. https://doi.org/10.1007/BF00371258

Pin, C., Paquette, J.-L., 1997. A mantle-derived bimodal suite in the Hercynian Belt: Nd isotope and trace element evidence for a subduction-related rift origin of the Late Devonian Brévenne metavolcanics, Massif Central (France). Contrib. Mineral. Petrol. 129, 222–238. https://doi.org/10.1007/s004100050334

Robardet, M., 2003. The Armorica 'microplate': fact or ¢ction? Critical review of the concept and contradictory palaeobiogeographical data. Palaeogeogr. Palaeoclimatol. Palaeoecol. 195, 125–148.

Rossi, P., Oggiano, G., Cocherie, A., 2009. A restored section of the "southern Variscan realm" across the Corsica–Sardinia microcontinent. Comptes Rendus Geosci. 341, 224–238. https://doi.org/10.1016/j.crte.2008.12.005

Rubatto, D., Ferrando, S., Compagnoni, R., Lombardo, B., 2010. Carboniferous high-pressure metamorphism of Ordovician protoliths in the Argentera Massif (Italy), Southern European Variscan belt. Lithos 116, 65–76. https://doi.org/10.1016/j.lithos.2009.12.013

Schulmann, K., Lexa, O., Racek, M., Tajcmanova, L., Konopasek, J., Edel, J.-B., Lehmann, A.P. ans J., 2008. Vertical extrusion and horizontal channel flow of orogenic lower crust: key exhumation mechanisms in large hot orogens? J Metamorph. Geol 26, 273–297.

Simeon, Y., 1979. Etude petrologique, geochimique et structurale des terrains cristallins de Belledonne entre l'Arc et L'Isere (Alpes Françaises). Université de Grenoble.

Sláma, J., Košler, J., Condon, D.J., Crowley, J.L., Gerdes, A., Hanchar, J.M., Horstwood, M.S.A., Morris, G.A., Nasdala, L., Norberg, N., Schaltegger, U., Schoene, B., Tubrett, M.N., Whitehouse, M.J., 2008. Plešovice zircon — A new natural reference material for U–Pb and Hf isotopic microanalysis. Chem. Geol. 249, 1–35. https://doi.org/10.1016/j.chemgeo.2007.11.005

Stampfli, G.M., Borel, G.D., Marchant, R., Mosar, J., 2002. Western Alps geological constraints on western Tethyan reconstructions. J. Virtual Explor. 7, 75–104.

Stampfli, G.M., Hochard, C., Vérard, C., Wilhem, C., Von Raumer, J.F., 2013. The formation of Pangea. Tectonophysics 593, 1–19. https://doi.org/10.1016/j.tecto.2013.02.037

Tabaud, A.-S., 2012. Le magmatisme des Vosges : conséquence des subductions paléozoïques (datation, pétrologie, géochimie, ASM). Université de Strasbourg.

Tait, J., Schatz, M., Bachtadse, V., Soffel, H., 2000. Palaeomagnetism and Palaeozoic palaeogeography of Gondwana and European terranes. Geol. Soc. Lond. Spec. Publ. 179, 21–31.

Tait, J.A., Bachtadse, V., Franke, W., Soffel, H.C., 1997. Geodynamic evolution of the European Variscan fold belt: palaeomagnetic and geological constraints. Geol. Rundsch. 86, 585–598.

Talbot, J.-Y., Faure, M., Chen, Y., Martelet, G., 2005. Pull-apart emplacement of the Margeride granitic complex (French Massif Central). Implications for the late evolution of the Variscan orogen. J. Struct. Geol. 27, 1610–1629. https://doi.org/10.1016/j.jsg.2005.05.008

Vivier, G., Ménot, R.-P., Giraud, P., 1987. Magmatismes et structuration orogenique paleozoiques de la chaine de Belledonne (massifs cristallins externes alpins) le domaine nord-oriental. Géologie Alp. 63, 25–53.

Von Raumer, J., Albrecht, J., Bussy, F., Lombardo, B., Ménot, R.-P., Schaltegger, U., 1999. The Palaeozoic metamorphic evolution of the Alpine External Massifs. Schweiz. Miner. Petrog Mitteilungen 79, 5–22.

Von Raumer, J.F., 1998. The Palaeozoic evolution in the Alps: from Gondwana to Pangea. Geol. Rundsch. 87, 407–435. https://doi.org/10.1007/s005310050219

Von Raumer, J.F., Bussy, F., Scaltegger, U., Schulz, B., Stampfli, G.M., 2013. Pre-Mesozoic Alpine basements? Their place in the European Paleozoic framework. GSA Bull. 125, 89–108.

Von Raumer, J.F., Bussy, F., Stampfli, G.M., 2009. The Variscan evolution in the External massifs of the Alps and place in their Variscan framework. Comptes Rendus Geosci., Mécanique de l'orogénie varisque : Une vision moderne de le recherche dans le domaine de

l'orogénieMechanics of Variscan Orogeny: A modern view on orogenic research 341, 239–252. https://doi.org/10.1016/j.crte.2008.11.007

Von Raumer, J.F., Finger, F., Veselá, P., Stampfli, G.M., 2014. Durbachites–Vaugnerites – a geodynamic marker in the central European Variscan orogen. Terra Nova 26, 85–95. https://doi.org/10.1111/ter.12071

Von Raumer, J.-F., Stampfi, G.M., Bussy, F., 2003. Gondwana-derived microcontinents, the constituents of the Variscan and Alpine collisional orogens. Tectonophysics 365, 7–22.

Von Raumer, J.F., Stampfli, G.M., Arenas, R., Martínez, S.S., 2015. Ediacaran to Cambrian oceanic rocks of the Gondwana margin and their tectonic interpretation. Int. J. Earth Sci. 104, 1107–1121. https://doi.org/10.1007/s00531-015-1142-x

Wang, L.-J., Griffin, W.L., Yu, J.-H., O'Reilly, S.Y., 2010. Precambrian crustal evolution of the Yangtze Block tracked by detrital zircons from Neoproterozoic sedimentary rocks. Precambrian Res. 177, 131–144. https://doi.org/10.1016/j.precamres.2009.11.008

FIGURE CAPTIONS

Figure 1. A: Location of External Crystalline Massifs (ECMs) within the Variscan belt, modified after (Faure et al., 2005, 2014; Tabaud, 2012; Talbot et al., 2005; Von Raumer, 1998). B: Geological map of ECMs, modified after (Debon and Lemmet, 1999; Guillot et al., 2009). Dashed box shows the position of Figure 2.

Figure 2. Geological map of the Southwestern part of the Belledonne Massif. The cross-sections on Figures 6A and 6B are shown by lines A and B respectively. Stars indicate samples used for thermobarometry (see Figs. 10, and 11. Squares indicate the dated samples of Figures 12, 13 and 15.

Figure 3. Outcrop photographs of stuctures related to D_1. A: contact between serpentinite and microgabbro in the Chamrousse ophiolitic complex showing top-to-the-NE sense of shear. B: F_1 drag fold of S_{0-1} foliation showing a top-to-the-NE sense of shear in the Rioupéroux-Livet unit near Séchilienne. Note the development of axial planar foliation. C: asymmetric sigmoidal quartz-feldspar aggregates indicating a top-to-the-E-NE sense of shear. D: transposition of S_0 bedding by S_1 cleavage during top-to-the-NE motion in the Rioupéroux-Livet unit. E: mylonitic metapelite near Allemont in the Rioupéroux-Livet unit. Note the west-to-east deformation increase in the Rioupéroux-Livet unit between outcrop photographs B to E. F: Initially E-W-striking mineral lineation reoriented in the NE-SW direction close to NE-SW crenulation lineation during the D_2 folding.

Figure 4. Outcrop photographs of structures related to D_2. A: folding of S_{0-1} foliation during the D_2 event in the metavolcanic rocks of the Rioupéroux-Livet unit. Note the absence of penetrative S_2 foliation. B: NE-SW-striking F_2 fold in metapelite near Allemont. Note i) the top-to-the-NW sense of shear on the NW flank and top-to-the-SE shearing on SE flank, and ii) the presence of melt pockets on each flank of the fold showing that melting is earlier than the

D_2 deformation. Black boxes indicate detail photographs E and F. C: S_2 foliation developed parallel to axial plane of F_2 fold in metapelite in the Rioupéroux-Livet unit. D: NE-SW striking crenulation lineation in weakly-metamorphosed schist in the Taillefer unit. E: Top-to-the-NW sheared melt pocket on the NW flank of the D_2 fold shown in picture B. F, Top-to-the-SE-sense of shear in the SE flank of the D_2 fold shown in picture B.

Figure 5. A: SW-NE cross-section through the Belledonne Massif. Stars indicate the locations of samples used for thermobarometry (See Figs. 10 and 11. B): W-E cross-section through the Taillefer unit. The two cross-sections are located on Figure 2. SMF: Synclinal Median Fault; ASZ: Allemont Shear Zone; RBE: Rivier Belle Etoile fault; RT: Rioupéroux Thrust.

Figure 6.Stereographic plots of poles of foliation planes, lineations and fold axes plotted on the lower hemisphere in equal-area projection; n represents the number of measurement. Contour interval = 10% probability of measurement values.

Figure 7. Representative photomicrographs of microstructures and mineral phases. The thin sections are parallel to the stretching lineation and perpendicular to foliation. A: sigmoidal garnet indicating a top-to-the-NE sense of shear in the Rioupéroux-Livet unit. B: conjugate shear bands developed on each flank of a D_2 fold in volcanoclastic facies of the Rioupéroux-Livet unit. C: sigmoidal garnet indicating a top-to-the-ENE sense of shear. D: sigmoidal kyanite indicating a top-to-the-ENE shearing related to the Dx deformation.

Figure 8. Field sketches of D_1-D_2 relationships. Quartz-feldspar-rich beds are shown in gray. A: Folding of the $S_{0\text{-}1}$ foliation by D_2 folds responsible for local development of S_2 in metapelitic layers. B: Reorientation of L_1 mineral lineation by D_2 event. C: Tight D_2 folding responsible

for shortening of S_{0-1}, development of S_2 foliation, and L_1 reorientation. D: Relationships between the conjugate post-folial shear bands developed on both limbs of D_2 folds, and refolding of L_1 stretching lineation. The N070E plane is parallel to the reoriented L_1 lineation.

Figure 9. Photomicrographs of mineralogical assemblages. A: Kyanite (Ky), plagioclase (Pl), garnet (Gt), muscovite (Mu), biotite (Bi), quartz (q) mineralogical assemblage observed in migmatitic metapelite of the Allemont migmatitic unit (sample MCE240). B: Garnet, biotite, muscovite, staurolite (Std), quartz mineralogical assemblage in metapelite of the Rioupéroux-Livet unit (Sample MCE-56va). C: Garnet, biotite, muscovite, plagioclase, quartz mineralogical assemblage in metapelite (Sample MCE -195a). Note the garnet overgrowth around biotite. Insert: Sillimanite grain cutting the S_1 foliation.

Figure 10: Isochemical phase diagrams of metapelite Sample MCE240 calculated for MnNCKFMASH system. See Figures 2 and, 5 for location. A. T-$X_{(H2O)}$ of Sample MCE240 at 0.7 GPa.. B. Isochemical phase diagram with the original bulk (Bulk1). The predicted Bi+Pl+Ab+Mu+Gt+ky+q peak assemblage observed in thin section (Figure 9A) gives P-T conditions of 0.68 ± 0.1 Gpa and 427 ± 16 °C. Prograde P-T conditions are estimated at 0.33 ± 0.05 Gpa and 370 ± 25 °C. Dotted line represents garnet compositional isopleths for rim and core. C. Isochemical phase diagram taking into account 5% of garnet fractionation (Bulk 2). The predicted Bi + Pl + Ab + Mu + Gt + ky + q peak assemblage observed in thin section (Figure 9A) gives P-T conditions of 0.535 ± 0.045 Gpa and 427.5 ± 17.5 °C. Dotted line represents garnet compositional isopleths for rim. D. P-T diagram showing the major typology difference between Bulk 1 and Bulk 2. Mineral abbreviations used are: Bi, Biotite; Mu, muscovite; Chl, Chlorite; Crd, Cordierite; St, Staurolite; San, K-feldspar; Pl, Plagioclase; Ab,

Albite; mic, Microcline; gl, Glaucophane; Gt, Garnet; and, Andalusite, ky, Kyanite; sill, Sillimanite; Opx, Orthopyroxene; q, Quartz; melt, silicate liquid.

Figure 11. A: Isochemical phase diagrams calculated for MnNCKFMASH system for metapelite Sample MCE-56va. See Figures 2, 5 for location. The predicted Bi+St+Mu+Gt+q assemblage observed in thin section (Figure 9B) gives P-T conditions of 0.58 ± 0.06 Gpa and 608 ± 14°C. Biotite, muscovite and pyrope compositional isopleths. B. T-$X_{(H2O)}$ of Sample MCE195a. C: Pseudosection diagrams calculated for MnNCKFMASH system for migmatitic metapelite Sample MCE-195a. See Figures 2, 5 for location. The predicted Bi+Pl+Mu+Gt+q+melt assemblage observed in thin section (Figure 9C) gives P-T conditions of 0.78 ± 0.07 Gpa and 680.5 ± 11.5°C. Garnet compositional isopleths. Mineral abbreviations are the same as for Figure 10.

Figure 12. Zircon SIMS U-Pb geochronological data for plagioclase-rich sills (Sample MCE116), see Figure 2 for location. A: Concordia diagram showing a 352.4 ± 1.4 Ma age. B: photomicrograph showing the texture of the dated plagioclase-rich sills. C: CL image of representative dated zircon.

Figure 13. Relative probability diagram of zircon LA-ICP-MS U-Pb ages of for detrital zircon from sandstone Sample MC5 from the Série Satinée of Western Belledonne, see Figure 2 for location. Age peaks are Neoproterozoic, since no zircon younger than 463 Ma was found, an Ordovican maximum age of deposition is assumed.

Figure 14. Relative probability age diagram of zircon LA-ICP-MS U-Pb ages of detrital zircons from a conglomerate sample from the Taillefer unit. Age peaks are Cambrian, with no zircon younger than 396 Ma. Location in Fig. 1

Figure 15. Monazite LA ICP-MS U-Pb ages of metapelite (Sample MCE-56va), see Figure 2 for location. A: Location of one representative monazite grain in the S_1 foliation plane. B: SEM-BSE image of representative dated monazite. C: Concordia diagram giving a lower intercept age of 337 ± 7 Ma.

Figure 16. Summary of the metamorphic conditions recorded in the southwestern part of the Belledonne Massif. The black squares are P-T data from (Guillot and Ménot, 1999). Black and gray (dashed) arrows represent inferred P-T path corresponding to the observed structures. Dx, D_1, and D_2 indicate the deformation phases described in this paper, including the literature data.

Figure 17. Conceptual model of the geodynamic evolution of the SW Belledonne Massif shown as schematic cross-sections through the orogen. A: Westward subduction of the Chamrousse oceanic domain at ca. 400-380 Ma. B: At *ca.* 380-360 Ma a slice of the Chamrousse oceanic domain is thrust eastwards, triggering an MP-LT metamorphism that defines the Dx/Mx tecto-metamorphic event. C: At *ca.* 360-350 Ma the bimodal magmatism of the Rioupéroux-Livet unit takes place and the Taillefer volcanosedimentary rocks are deposited; D: During the Early Carboniferous, between ca 350 Ma and 330 Ma, the D_1/M_1 tectonometamorphic event is responsible for eastward nappe stacking coeval with an MP-HT prograde metamorphism. E: After 330 Ma, the orogenic crust recorded the D_2 event in response to a NW-SE bulk shortening.

Table 1. Summary of tectonic and metamorphic events recorded in this study for the Southwestern part of the Belledonne Massif. The two geochronological data shown [1] and [2] for the Dx event are from Ménot et al. (1988) and Pin and Carme (1987), respectively.

Table 2. Bulk rock composition in weight percent oxides for Samples MCE240, MCE56-Va, and MCE195a.

Table 3. Representative chemical compositions of minerals used for themobarometric calculation.

Table 4. List of solid solutions used in the themobarometric modeling.

Table 5. Zircon U-Pb analyses of plagioclase-rich sill MCE116.

Table 6. Detrital zircon U-Pb analyses of sandstone MC5.

Table 7. Detrital zircon U-Pb analyses of conglomerate from Taillefer unit.

Table 8. Monazite U-Pb analyses of micaschist MCE56-Va.

Table 1

			SMF			
		Outer branch	SW Inner branch			
				RT		
					ASZ	
EVENTS		Série-Satinée	Chamrousse ophiolitic unit	Rioupéroux-Livet unit	Allemont migmatitic unit	Taillefer unit
D_2	Structure	• upright folds • high angle S_2 • NE-SW L_2	• buckled folds SE vergent • NE-SW L_2	• buckled folds SE vergent • upright folds • high angle S_2 • NE-SW L_2 crenualtion	• buckled folds SE vergent • upright folds • high angle S_2 • NE-SW L_2 crenualtion	• upright folds NE-SW axis • NE-SW L_2 crenualtion • L_2 streching lineation
	Metamorphism	Greenschist facies	Retrograde Greenschist facies ?	Retrograde Greenschist facies ?	Retrograde amphibolite facies ? Sill - melt	Greenschist facies
	Age					Visean ca. 340Ma
			Late D1 thrusting of the Taillefer unit			
D_1	Structure	Low angle S_1 ?	• Low angle S_1 • E-W L_1	• Low angle S_1 • Recumbent folds E vergent • E-W L_1	• Low angle S_1 • Recumbent folds E vergent • E-W L_1	
	Kinematics		• top to the E-NE	• top to the E-NE	• top to the E-NE	
	Metamorphism	Greenschist facies?	Amphibolite Facies P ? T ?	Amphibolite Facies Gt-Bt-melt ca. 0.6 Gpa; 600°C	Amphibolite Facies Gt-Bt-melt ca. 0.8 GPa; 630°C	
	Age		339 ± 5 Ma (U-PbMnz)	339 ± 5 Ma (U-PbMnz)	339 ± 5 Ma (U-PbMnz)	

				Bi-modal magmatism @ 352 ± 1 Ma (U-PbZr). • S_0 bedding	
Dx	Kinematics		not documented • Eastward thrusting ?	• Eastward thrusting	
	Metamorphism			•Gt-Ky-Ab metapelite ca. 0.3 GPa; 370°C up to ca. 0.5 GPa; 430°C	
	Age			ca. 380 Ma?	
Pre orogenic		turbidite passive margin	Oceanic metamorphism 0.3-0.4 GPa; 500- 600°C	terrigenous passive margin	
		Cambro-ordovician	[1] 496 ± 6 Ma (U-PbZr) [2] 497 ± 24 Ma (Sm-Ndwr)		

Table 2

Sample	GARNET				BIOTITE			MUSCOVITE			PLAGIOCLASE		STAUROLITE
	MCE240		MCE56-Va	MCE195a	MCE240	MCE56-Va	MCE195a	MCE240	MCE56-Va	MCE195a	MCE240		MCE56-Va
	Rim	Core											
Wt%													
SiO2	37.87	37.87	37.29	36.45	34.61	35.96	35.30	46.61	45.99	49.34	70.08	64.40	27.72
Al2O3	20.37	20.06	20.27	20.84	17.78	18.90	19.03	34.34	36.82	36.10	19.08	21.58	55.91
TiO2	0.12	0.04	0.08	0.00	2.12	1.60	2.97	0.78	0.27	0.55	0.00	0.00	0.54
FeO	31.47	28.49	35.72	32.66	20.14	19.72	17.20	1.11	1.07	1.01	0.11	0.10	10.71
MgO	2.02	1.31	3.28	2.64	8.91	9.76	8.67	0.56	0.66	0.75	0.00	0.00	0.70
MnO	0.96	3.54	0.17	4.59	0.12	-0.02	0.08	0.08	-0.01	0.00			0.19
CaO	6.75	7.58	2.27	0.96	0.00	-0.01	0.00	0.00	-0.02	0.01	0.23	4.02	0.02
Na2O					0.09	0.22	0.22	1.04	1.78	0.25	11.51	9.31	0.07
K2O					8.61	9.21	9.57	9.62	9.20	7.58	0.14	0.15	0.24
Total	99.55	98.88	99.09	98.12	92.38	95.34	93.02	94.15	95.76	95.59	101.14	99.56	96.09
Mol cations													
Si	3.05	3.08	3.03	3.00	5.62	5.61	5.65	6.29	6.04	6.61	12.09	11.42	7.70
Al	1.93	1.91	1.94	2.02	3.00	3.08	3.15	4.93	5.20	4.99	3.88	4.51	18.32
Ti	0.01	0.00	0.01	0.00	0.23	0.19	0.31	0.07	0.03	0.06	0.00	0.00	0.11
Fe	2.12	1.93	2.42	2.25	2.73	2.57	2.30	0.13	0.12	0.10	0.02	0.01	2.49
Mg	0.24	0.16	0.40	0.32	2.16	2.27	2.07	0.11	0.13	0.15	0.00	0.00	0.29
Mn	0.07	0.24	0.01	0.32	0.01	0.00	0.01	0.01	0.00	0.00			0.04
Ca	0.58	0.66	0.20	0.08	0.00	0.00	0.00	0.00	0.00	0.00	0.04	0.76	0.01

Na					0.03	0.07	0.07	0.27	0.45	0.07	3.85	3.20	0.04
K					1.57	1.62	1.72	1.50	1.41	1.14	0.03	0.03	0.08
Fe#													0.89
Mg#					0.44	0.47	0.48						
End members %													
Ab											98.13	80.08	
An											1.06	19.09	
Orth											0.81	0.83	
Prp	8.04	5.29	13.10	10.87									
Alm	70.42	64.58	80.00	75.54									
Grs	19.36	22.01	6.52	2.84									
Sps	2.18	8.12	0.38	10.74									

Table 3

Wt%	Samples MCE240	MCE56-Va	MCE195a
SiO2	67.13	66.97	58.56
Al2O3	15.52	17.1	18.60
Fe2O3	5.64	5.8	7.52
MgO	2.02	1.51	2.68
CaO	0.83	0.33	1.24
Na2O	1.76	0.71	3.28
K2O	3.37	3.53	4.52
TiO2	0.80	0.8	1.02
MnO	0.09	0.07	0.06
P2O5	0.12	0.11	0.19
Cr2O3	0.01	0.04	0.01
NiO	0.00	0.01	0.00
H2O	2.30	2.29	1.69
Sum	99.59	99.27	99.37

Table 4

Mineral	Abbrev.	Solution model	Reference	End-Member
Biotite	Bi	Bio(TCC)	Tajcmanova et al., 2009	mts, sdph, east, mnbi, ann, phl, obi
Muscovite	Mu	Mica(CHA)	Coggon and Holland, 2002 - Auzanneau et al.,2010	mu, pa, ma, cel, fcel
Garnet	Gt	Gt(WPH)	White et al., 2000	spss, alm, py, gr
Cordierite	Crd	hCrd	Baumgartner, 2003	mncrd, fcrd, crd, hmncrd, hfcrd, hcrd
Plagioclase	Pl	Pl(h)	Newton et al., 1981	an, abh
K-Feldspar	San	San	Waldbaum and Thomson, 1968	san, abh
Staurolite	St	St(HP)		mnst, fst, mst
Melt	melt	melt(HP)	White et al., 2001	h2oL, fo8L, fa8L, abl, sil8L, anL, kspL, q8L
Chl	Chl	Chl(HP)	Holland et al. 1998	mame,mafchl,mnchl,fames,fafchl, daph,ames,afchl,clin
Epidote	Ep	Ep(HP)		cz, fep

Table 5

Sample/spot #	[U] (ppm)	[Th] (ppm)	[Pb] (ppm)	Th/U	f_{206} %	Radiogenic isotopic ratios						Age (Ma)					
						$^{207}Pb/^{206}Pb$	±σ (%)	$^{207}Pb/^{235}U$	±σ (%)	$^{206}Pb/^{238}U$	±σ (%)	$^{207}Pb/^{206}Pb$	±σ (%)	$^{207}Pb/^{235}U$	±σ (%)	$^{206}Pb/^{238}U$	±σ (%)
MC116@02	364	136	24	0.375	{0.11}	0.05414	1.12	0.40847	1.97	0.05556	1.52	340	28	348	6	349	5
MC116@03	116	29	7	0.247	{0.44}	0.05622	1.91	0.40219	4.07	0.05353	1.64	319	83	343	12	347	6
MC116@04	627	196	40	0.312	{0.15}	0.05343	0.83	0.41144	1.72	0.05558	1.50	347	19	350	5	350	5
MC116@05	332	101	21	0.305	{0.05}	0.05399	1.68	0.40685	2.31	0.05550	1.51	355	39	347	7	345	5
MC116@07	229	59	14	0.257	{0.60}	0.05708	1.64	0.40190	3.18	0.05556	1.50	303	63	343	9	349	5
MC116@08	357	103	23	0.290	{0.24}	0.05411	1.10	0.41657	1.86	0.05558	1.50	376	24	354	6	350	5
MC116@09	301	90	19	0.300	{0.25}	0.05456	1.21	0.40203	2.22	0.05554	1.51	312	37	343	6	348	5
MC116@1	451	153	29	0.340	{0.10}	0.05375	0.98	0.41081	1.80	0.05554	1.51	361	22	349	5	348	5
MC116@10	311	80	19	0.257	{0.09}	0.05402	1.55	0.40646	2.26	0.05553	1.51	341	38	346	7	347	5
MC116@11	163	55	11	0.341	{0.34}	0.05319	1.63	0.41245	2.22	0.05562	1.52	337	36	351	7	353	5
MC116@12	481	147	31	0.306	{0.08}	0.05290	0.96	0.40966	1.78	0.05562	1.51	325	22	349	5	352	5
MC116@13	167	42	11	0.253	{0.27}	0.05452	1.60	0.42265	2.21	0.05562	1.51	393	36	358	7	353	5
MC116@14	366	73	23	0.199	{0.12}	0.05414	1.58	0.41451	2.29	0.05565	1.50	337	39	352	7	354	5
MC116@15	177	74	12	0.419	{0.22}	0.05467	1.62	0.40508	2.87	0.05555	1.50	325	55	345	8	348	5
MC116@16	170	42	11	0.249	{0.27}	0.05442	1.60	0.42174	2.24	0.05562	1.56	388	36	357	7	353	5
MC116@17	391	168	26	0.430	{0.10}	0.05422	1.06	0.41701	1.94	0.05566	1.54	347	26	354	6	355	5

MC116@18	84	26	5	0.306	{0.54}	0.05374	2.29	0.41780	2.76	0.0564	1.54	360	51	354	8	354	5
MC116@21	70	15	4	0.211	{0.87}	0.05286	2.61	0.40514	3.03	0.0556	1.54	323	58	345	9	349	5
MC116@22	281	122	19	0.435	{0.19}	0.05435	1.22	0.42379	1.94	0.0566	1.51	386	27	359	6	355	5
MC116@23	383	177	26	0.464	{0.19}	0.05458	1.06	0.42028	2.03	0.0574	1.52	332	30	356	6	360	5
MC116@24	199	84	13	0.423	{0.14}	0.05469	1.49	0.40750	2.32	0.0551	1.50	355	39	347	7	346	5
MC116@25	332	102	22	0.306	{0.10}	0.05405	1.14	0.42455	1.91	0.0570	1.53	373	25	359	6	357	5
MC116@26	151	36	10	0.240	{0.30}	0.05453	1.71	0.43003	2.28	0.0572	1.52	393	38	363	7	359	5
MC116@27	370	103	24	0.278	{0.11}	0.05357	1.52	0.41308	2.18	0.0559	1.56	353	34	351	6	351	5
MC116@28	159	39	10	0.244	{0.24}	0.05264	1.64	0.41093	2.28	0.0566	1.58	313	37	350	7	355	5
MC116@29	170	72	11	0.424	{0.31}	0.05506	1.62	0.40988	3.26	0.0565	1.56	313	64	349	10	354	5
MC116@30	151	52	10	0.346	{0.07}	0.05579	1.74	0.42121	2.44	0.0553	1.52	421	42	357	7	347	5
MC116@31	526	121	34	0.229	{0.04}	0.05434	1.00	0.42117	1.84	0.0566	1.50	371	24	357	6	355	5
MC116@32	355	150	24	0.423	{0.10}	0.05429	1.13	0.41799	1.99	0.0566	1.51	351	29	355	6	355	5
MC116@33	236	81	15	0.344	{0.28}	0.05524	1.33	0.41308	2.44	0.0565	1.53	330	42	351	7	354	5
MC116@34	122	39	8	0.321	{0.26}	0.05514	1.83	0.41967	2.91	0.0573	1.55	333	55	356	9	359	5
MC116@35	685	182	45	0.266	{0.12}	0.05412	0.77	0.42815	1.69	0.0574	1.51	376	17	362	5	360	5
MC116@36	302	129	20	0.429	{0.11}	0.05371	1.23	0.41882	1.95	0.0566	1.52	359	27	355	6	355	5
MC116@37	108	39	7	0.358	{0.28}	0.05260	2.16	0.40695	2.66	0.0561	1.54	311	49	347	8	352	5
MC116@38	219	54	14	0.247	{0.12}	0.05370	1.40	0.42159	2.06	0.0569	1.51	358	31	357	6	357	5
MC116@39	300	122	20	0.406	{0.11}	0.05513	1.17	0.42456	2.02	0.0567	1.51	383	30	359	6	356	5

MC116@40	235	106	16	0.452	{0.11}	0.05415	1.32	0.41253	2.13	0.0561	1.50	342	34	351	6	352	5
MC116@41	502	193	32	0.385	{0.57}	0.05746	1.09	0.40173	2.26	0.0549	1.51	330	38	343	7	345	5
MC116@42	144	36	9	0.250	{0.13}	0.05354	1.74	0.42462	2.31	0.0575	1.52	352	39	359	7	361	5
MC116@43	272	95	18	0.351	{0.04}	0.05251	1.38	0.40906	2.04	0.0565	1.51	307	31	348	6	354	5
MC116@44	144	76	10	0.532	{0.22}	0.05336	2.51	0.41424	2.93	0.0563	1.52	344	56	352	9	353	5
MC116@45	197	85	13	0.434	{0.11}	0.05562	1.45	0.41267	2.26	0.0547	1.53	402	37	351	7	343	5
MC116@47	598	250	39	0.418	{0.05}	0.05384	1.01	0.40813	1.85	0.0554	1.51	347	24	348	5	348	5
MC116@48	146	60	9	0.411	{0.15}	0.05521	2.93	0.41080	3.57	0.0551	1.55	373	71	349	11	346	5
MC116@49	229	79	15	0.344	{0.19}	0.05366	1.57	0.42252	2.18	0.0571	1.51	357	35	358	7	358	5
MC116@50	142	35	9	0.247	{0.33}	0.05443	1.78	0.41870	2.34	0.0558	1.51	389	40	355	7	350	5
MC116@51	326	126	21	0.387	{0.06}	0.05291	1.23	0.40713	1.94	0.0558	1.50	325	28	347	6	350	5
MC116@52	434	105	27	0.242	{0.10}	0.05429	0.97	0.40892	1.87	0.0554	1.50	351	25	348	6	348	5
MC116@53	326	88	21	0.268	{0.10}	0.05224	1.57	0.40340	2.17	0.0560	1.50	296	35	344	6	351	5
MC116@54	263	85	17	0.324	{0.21}	0.05361	1.71	0.41616	2.33	0.0563	1.58	355	38	353	7	353	5
MC116@55	254	80	16	0.315	{0.27}	0.05506	1.31	0.40549	2.84	0.0556	1.51	325	54	346	8	349	5
MC116@56	620	246	42	0.397	{0.09}	0.05352	0.83	0.40273	1.72	0.0570	1.51	351	19	357	5	357	5
MC116@57	145	38	9	0.263	{0.08}	0.05446	1.86	0.41531	2.53	0.0560	1.50	363	45	353	8	351	5
MC116@59	274	119	19	0.434	{0.10}	0.05326	1.25	0.40218	1.99	0.0572	1.54	340	28	356	6	359	5
MC116@60	383	167	26	0.436	{0.09}	0.05241	1.08	0.41329	1.85	0.0572	1.50	303	24	351	6	359	5
MC116@61	107	24	7	0.226	{0.37}	0.05284	2.03	0.41806	2.58	0.0574	1.59	322	45	355	8	360	6

MC116@62	251	62	16	0.248	{0.24}	0.05478	1.45	0.412437	2.46	0.0565	1.51	324	43	351	7	355	5
MC116@63	215	61	14	0.286	{0.20}	0.05468	1.44	0.41941	2.37	0.0573	1.51	333	41	356	7	359	5
MC116@64	86	20	6	0.231	{0.82}	0.05385	2.29	0.42405	2.77	0.0571	1.56	365	51	359	8	358	5
MC116@65	282	102	19	0.363	{0.16}	0.05375	1.58	0.41860	2.18	0.0565	1.51	361	35	355	7	354	5

Table 6

Spot No.	Th (ppm)	U (ppm)	Th/U	Ratios						Ages (Ma)						Discordance (%)	Best Ages	± 1σ
				$^{207}Pb/^{206}Pb$	± 1σ	$^{206}Pb/^{238}U$	± 1σ	$^{207}Pb/^{235}U$	± 1σ	$^{207}Pb/^{206}Pb$	± 1σ	$^{206}Pb/^{238}U$	± 1σ	$^{207}Pb/^{235}U$	± 1σ			
MC5-37	894	1775	0.500	0.060619	0.000060	0.074748	0.000125	0.618108	0.005480	610	21	463	7	489	3	5.6%	463	7
MC5-35	176	1244	0.140	0.059550	0.000059	0.082999	0.000139	0.680891	0.005970	577	42	514	8	526	4	2.3%	514	8
MC5-58	855	1525	0.560	0.059777	0.000061	0.084533	0.000143	0.696563	0.006340	595	21	523	8	537	4	2.7%	523	8
MC5-41	331	940	0.350	0.061671	0.000064	0.084887	0.000143	0.722215	0.006630	618	45	524	8	542	5	3.4%	524	8
MC5-39	214	563	0.381	0.059772	0.000062	0.084944	0.000143	0.699441	0.006460	593	21	526	8	538	4	2.3%	526	8
MC5-67	762	663	0.150	0.060555	0.000079	0.085500	0.000149	0.713838	0.008380	623	19	529	9	547	5	3.4%	529	9
MC5-59	715	894	0.801	0.061446	0.000075	0.085775	0.000148	0.726750	0.007900	655	19	530	9	555	5	4.7%	530	9
MC5-18	128	117	0.100	0.062442	0.000075	0.086442	0.000147	0.743774	0.007970	689	19	534	9	565	5	5.8%	534	9
MC5-64	1330	1989	0.670	0.060615	0.000061	0.087757	0.000148	0.726222	0.006500	549	51	540	9	542	7	0.4%	540	9
MC5-60	539	1169	0.46	0.059896	0.000066	0.087940	0.000150	0.726091	0.007160	600	20	543	9	554	4	2.0%	543	9

MC5-54	535	672	0.800	0.060	0.000	0.089	0.000	0.742	0.000	621	20	550	9	564	5	2.5%	550	9
MC5-32	353	835	0.420	0.059	0.000	0.089	0.000	0.742	0.000	520	49	553	9	546	6	-1.3%	553	9
MC5-44	325	640	0.510	0.060	0.000	0.089	0.000	0.745	0.000	612	21	554	9	566	4	2.2%	554	9
MC5-36	86	278	0.310	0.059	0.000	0.090	0.000	0.740	0.000	576	20	560	9	563	4	0.5%	560	9
MC5-43	273	889	0.310	0.061	0.000	0.090	0.000	0.769	0.000	639	45	560	9	576	5	2.9%	560	9
MC5-31	790	819	0.960	0.060	0.000	0.091	0.000	0.760	0.000	610	20	565	9	574	4	1.6%	565	9
MC5-48	396	590	0.671	0.060	0.000	0.091	0.000	0.765	0.000	619	21	567	9	577	4	1.8%	567	9
MC5-05	178	171	0.041	0.063	0.000	0.092	0.000	0.810	0.000	721	20	571	9	603	4	5.6%	571	9
MC5-06	860	690	0.250	0.061	0.000	0.093	0.000	0.789	0.000	652	21	575	9	591	4	2.8%	575	9
MC5-07	179	417	0.431	0.060	0.000	0.093	0.000	0.783	0.000	631	21	576	9	587	4	1.9%	576	9
MC5-23	403	215	0.880	0.058	0.000	0.093	0.000	0.749	0.000	533	20	576	9	568	4	-1.4%	576	9
MC5-20	201	596	0.340	0.059	0.000	0.094	0.000	0.765	0.000	567	22	580	9	577	4	-0.5%	580	9

MC5-30	192	301	0.642	0.060	0.000	0.094	0.000	0.780	0.000	609	21	580	9	586	4	1.0%	580	9
MC5-45	3412	1497	0.280	0.060	0.000	0.094	0.000	0.787	0.000	619	21	582	9	590	4	1.4%	582	9
MC5-78	1566	1927	0.811	0.059	0.000	0.094	0.000	0.779	0.000	594	22	583	9	585	4	0.3%	583	9
MC5-40	480	481	0.000	0.061	0.000	0.094	0.000	0.805	0.000	660	21	584	9	600	4	2.7%	584	9
MC5-34	184	559	0.330	0.060	0.000	0.095	0.000	0.796	0.000	583	45	585	9	584	5	-0.2%	585	9
MC5-19	94	202	0.470	0.060	0.000	0.095	0.000	0.801	0.000	628	21	590	10	598	4	1.4%	590	10
MC5-17	77	109	0.710	0.062	0.000	0.096	0.000	0.832	0.000	636	54	591	10	600	8	1.5%	591	10
MC5-82	419	838	0.502	0.060	0.000	0.095	0.000	0.796	0.000	610	20	591	10	595	5	0.7%	591	10
MC5-27	543	261	0.080	0.061	0.000	0.096	0.000	0.827	0.000	673	20	596	10	612	4	2.7%	596	10
MC5-13	758	1041	0.731	0.060	0.000	0.097	0.000	0.821	0.000	639	20	601	10	609	4	1.3%	601	10
MC5-69	699	553	0.261	0.061	0.000	0.097	0.000	0.834	0.000	579	64	601	10	596	10	-0.8%	601	10
MC5-24	243	205	0.19	0.063	0.000	0.097	0.000	0.863	0.000	741	19	602	10	632	5	5.0%	602	10

MC5-22	413	336	1.231	0.063095	0.000065	0.009809	0.000165	0.853306	0.007761	711	21	603	10	626	4	3.8%	603	10
MC5-68	154	121	1.270	0.061810	0.000094	0.009800	0.000174	0.835021	0.011510	668	18	603	10	616	6	2.2%	603	10
MC5-50	496	518	1.961	0.060692	0.000063	0.009827	0.000166	0.825459	0.007590	636	21	604	10	611	4	1.2%	604	10
MC5-38	156	139	1.122	0.061260	0.000090	0.009875	0.000174	0.834131	0.011010	648	18	607	10	616	6	1.5%	607	10
MC5-57	476	203	0.340	0.060189	0.000099	0.009871	0.000177	0.819081	0.012210	610	18	607	10	608	7	0.2%	607	10
MC5-29	369	487	0.760	0.060432	0.000062	0.009886	0.000166	0.823774	0.007490	619	21	608	10	610	4	0.3%	608	10
MC5-66	273	1596	0.170	0.060712	0.000062	0.009887	0.000168	0.827557	0.007570	629	21	608	10	612	4	0.7%	608	10
MC5-08	199	667	0.300	0.061271	0.000061	0.009926	0.000166	0.838567	0.007370	598	44	609	10	607	5	-0.3%	609	10
MC5-28	468	477	0.980	0.062194	0.000064	0.009932	0.000167	0.851607	0.007690	681	21	610	10	626	4	2.6%	610	10
MC5-63	208	864	0.242	0.061436	0.000064	0.009969	0.000169	0.844264	0.007840	639	44	612	10	618	5	1.0%	612	10
MC5-89	1922	827	0.320	0.061842	0.000072	0.009985	0.000172	0.851272	0.008910	669	20	614	10	625	5	1.8%	614	10
MC5-93	1033	2899	0.360	0.060753	0.000063	0.101014	0.000173	0.846997	0.007870	630	21	621	10	623	4	0.3%	621	10

MC5-77	630	1830	0.341	0.061 53	0.000 063	0.103 31	0.001 76	0.876 36	0.000 803	658	21	634	10	639	4	0.8%	634	10
MC5-81	1576	819	0.930	0.062 06	0.000 071	0.103 46	0.001 78	0.885 19	0.000 910	676	20	635	10	644	5	1.4%	635	10
MC5-76	606	656	0.922	0.058 68	0.000 066	0.104 28	0.001 79	0.843 54	0.000 845	555	21	639	10	621	5	-2.8%	639	10
MC5-94	6107	2883	0.121	0.064 13	0.000 075	0.104 13	0.001 80	0.920 55	0.000 964	746	20	639	11	663	5	3.8%	639	11
MC5-74	608	328	0.866	0.061 51	0.000 088	0.104 46	0.001 84	0.858 88	0.001 145	657	18	640	11	644	6	0.6%	640	11
MC5-100	4344	3463	1.250	0.060 75	0.000 065	0.104 37	0.001 79	0.874 06	0.000 846	630	21	640	10	638	5	-0.3%	640	10
MC5-10	78	182	0.431	0.061 18	0.000 068	0.104 65	0.001 77	0.882 79	0.000 872	646	20	642	10	642	5	0.0%	642	10
MC5-75	1652	1217	0.360	0.061 29	0.000 064	0.104 80	0.001 78	0.885 50	0.000 821	649	21	642	10	644	4	0.3%	642	10
MC5-83	915	986	0.932	0.062 76	0.000 068	0.104 66	0.001 79	0.905 51	0.000 877	700	20	642	10	655	5	2.0%	642	10
MC5-55	398	133	0.991	0.063 48	0.000 112	0.104 91	0.001 91	0.918 16	0.001 468	724	17	643	11	661	8	2.8%	643	11
MC5-90	1844	1555	0.190	0.061 74	0.000 065	0.105 34	0.001 80	0.896 60	0.000 842	665	21	646	10	650	5	0.6%	646	10
MC5-73	148	548	0.27	0.053 98	0.000 067	0.106 03	0.001 82	0.789 12	0.000 892	370	20	650	11	591	5	-9.1%	650	11

MC5-80	1028	892	1.15	0.06276	0.00070	0.10631	0.00182	0.91986	0.00921	700	20	651	11	662	5	1.7%	651	11
MC5-26	155	252	0.62	0.06192	0.00067	0.10652	0.00180	0.90948	0.00873	671	20	653	10	657	5	0.6%	653	10
MC5-98	4191	3372	1.24	0.06120	0.00064	0.10677	0.00183	0.90076	0.00851	646	21	654	11	652	5	-0.3%	654	11
MC5-97	266	463	0.58	0.06382	0.00090	0.10760	0.00191	0.94670	0.01208	645	56	657	11	654	9	-0.5%	657	11
MC5-79	715	567	1.26	0.06169	0.00070	0.10773	0.00185	0.91628	0.00928	663	20	660	11	660	5	0.0%	660	11
MC5-87	661	620	1.07	0.05883	0.00077	0.10785	0.00188	0.87475	0.01036	561	19	660	11	638	6	-3.3%	660	11
MC5-51	525	801	0.66	0.06270	0.00064	0.10839	0.00183	0.93706	0.00852	698	21	663	11	671	4	1.2%	663	11
MC5-70	375	401	0.94	0.06179	0.00088	0.10905	0.00192	0.92898	0.01194	667	18	667	11	667	6	0.0%	667	11
MC5-49	341	614	0.56	0.06354	0.00065	0.10943	0.00185	0.95868	0.00880	726	21	669	11	683	5	2.1%	669	11
MC5-85	1763	2324	0.76	0.06246	0.00063	0.11150	0.00190	0.96013	0.00865	690	21	681	11	683	4	0.3%	681	11
MC5-84	2730	3556	0.77	0.06443	0.00064	0.11190	0.00190	0.99392	0.00878	756	21	684	11	701	4	2.5%	684	11
MC5-12	142	172	0.83	0.06417	0.00071	0.11427	0.00193	1.01117	0.00992	747	20	697	11	709	5	1.7%	697	11

MC5-88	731	1017	0.720	0.062507	0.000067	0.115444	0.000198	0.994958	0.000959	691	21	704	11	701	5	-0.4%	704	11
MC5-11	383	476	0.800	0.064641	0.000065	0.118441	0.000198	1.051633	0.000933	755	21	721	11	730	5	1.2%	721	11
MC5-14	127	231	0.550	0.067190	0.000071	0.112611	0.000212	1.168444	0.001098	766	47	763	12	764	8	0.1%	763	12
MC5-46	331	425	0.780	0.067590	0.000069	0.112988	0.000219	1.210400	0.001090	856	20	787	12	805	5	2.3%	787	12
MC5-56	301	303	0.990	0.068310	0.000080	0.113238	0.000227	1.246779	0.001306	878	19	801	13	822	6	2.6%	801	13
MC5-72	252	1145	0.220	0.069780	0.000070	0.113674	0.000232	1.315142	0.001172	884	41	825	13	841	6	1.9%	825	13
MC5-04	435	509	0.860	0.069110	0.000068	0.114944	0.000249	1.424088	0.001235	902	20	898	14	899	5	0.1%	898	14
MC5-02	220	434	0.510	0.071330	0.000070	0.115039	0.000251	1.479160	0.001281	967	20	903	14	922	5	2.1%	903	14
MC5-15	23	88	0.260	0.067430	0.000071	0.115152	0.000255	1.408900	0.001306	851	20	909	14	893	6	-1.8%	909	14
MC5-03	75	182	0.410	0.071150	0.000074	0.115953	0.000268	1.565074	0.001442	962	20	954	15	956	6	0.2%	954	15
MC5-62	365	432	0.840	0.072710	0.000077	0.116675	0.000284	1.671523	0.001573	1006	20	994	16	998	6	0.4%	994	16
MC5-16	172	220	0.790	0.073330	0.000091	0.116824	0.000290	1.701026	0.001886	1023	18	1002	16	1009	7	2.1%	1023	18

MC5-86	1357	876	1.551	0.07630	0.00008	0.18359	0.00314	1.93115	0.01805	1103	20	1087	17	1092	6	1.5%	1103	20
MC5-52	179	167	1.070	0.12322	0.00125	0.35617	0.00606	6.05059	0.05474	2003	18	1964	29	1983	8	2.0%	2003	18
MC5-33	123	126	0.970	0.12560	0.00133	0.34942	0.00597	6.05139	0.05688	2006	40	1927	29	1965	12	4.1%	2006	40
MC5-42	17	415	0.041	0.12718	0.00124	0.36881	0.00622	6.46711	0.05572	2059	18	2024	29	2041	8	1.7%	2059	18
MC5-65	739	553	1.340	0.13119	0.00127	0.39274	0.00665	7.10330	0.06108	2114	18	2136	31	2124	8	-1.0%	2114	18
MC5-96	2518	2821	0.890	0.13189	0.00128	0.41017	0.00700	7.45809	0.06497	2123	18	2216	32	2168	8	-4.2%	2123	18
MC5-53	110	299	0.370	0.15158	0.00156	0.43964	0.00753	9.18813	0.08457	2364	17	2349	34	2357	8	0.6%	2364	17
MC5-25	117	259	0.451	0.16609	0.00159	0.46840	0.00785	10.2672	0.09059	2519	17	2477	34	2500	8	1.7%	2519	17
MC5-71	308	189	0.640	0.19249	0.00192	0.55068	0.00868	13.4306	0.12058	2764	17	2642	37	2711	8	4.6%	2764	17
MC5-99	974	2519	0.390	0.19271	0.00185	0.54843	0.00935	14.5706	0.12537	2765	17	2819	39	2788	8	-1.9%	2765	17
MC5-01	76	103	0.740	0.20236	0.00196	0.56804	0.00951	14.8508	0.13524	2845	16	2900	39	2868	8	-1.9%	2845	16
MC5-61	374	380	0.99	0.20324	0.00204	0.57417	0.00887	14.4978	0.13081	2852	16	2688	38	2783	9	6.1%	2852	16

MC5-09	209	200	1.040	0.209380	0.000200	0.61086	0.010021	17.636277	0.148455	2901	16	3073	41	2970	8	-5.6%	2901	16
MC5-92	568	645	0.880	0.209880	0.000205	0.60057	0.010027	17.373078	0.152355	2904	17	3032	41	2956	8	-4.2%	2904	17
MC5-21	32	81	.400	0.201479	0.000232	0.51975	0.000904	15.393088	0.149889	2905	33	2681	38	2811	10	8.4%	2905	33
MC5-91	1222	1397	.880	0.201208	0.000204	0.58539	0.009974	17.115448	0.147480	2922	17	2971	41	2941	8	-1.6%	2922	17
MC5-47	117	845	0.140	0.203063	0.000223	0.59278	0.010033	18.849055	0.162241	3056	16	3001	41	3034	8	1.8%	3056	16
MC5-95	5085	11379	0.045	0.112928	0.000127	0.006360	0.000108	1.133356	0.000990	1710	43	385	6	645	7	67.5%		

Table 7

Zr no	Spot No.	Pb (ppm)	Th (ppm)	U (ppm)	Th/U	Ratios ^{238}Pb/^{206}Pb	Err %	^{207}Pb/^{206}Pb	Err %	^{206}Pb/^{238}U	±1σ	^{207}Pb/^{235}U	±1σ	rho	Ages (Ma) ^{207}Pb/^{206}Pb	±1σ	^{206}Pb/^{238}U	±1σ	^{207}Pb/^{235}U	±1σ	Discoor-dance (%)	Best Ages	±1σ
Tail1-1	5020616	143	96	249	0.38	1.91182656	1.15283142	0.1865	1.0616622	0.52306	0.00603	13.44831	0.16073	0.96457626	2712	17	2712	26	2712	11	0.0%	2712	17
Tail1-2	6020616	435	24	999	0.02	2.25759115	1.1491139	0.16193	1.04366084	0.44295	0.00509	9.8858	0.11699	0.97128854	2476	18	2364	23	2424	11	4.7%	2476	18
Tail1-3	7020616	212	162	329	0.49	1.77822036	1.14873035	0.2063	1.05186621	0.56236	0.00646	15.99386	0.18963	0.96886739	2877	17	2876	27	2876	11	0.0%	2877	17
Tail1-4	80206	241	101	473	0.21	2.06573	1.14648	0.18026	1.04848	0.484	0.005	12.029	0.142	0.96859	2655	17	2545	24	2607	11	4.3%	2655	17

	16					158	103		552	09	55	74	39	812									
Tail16-5	9020616	180	71	391	0.18	2.2544356	1.14525329	0.1708	1.05386417	0.44357	0.00508	10.4447	0.12379	0.96629994	2566	18	2367	23	2475	11	8.4%	2566	18
Tail16-6	10020616	26	34	71	0.48	2.94273439	1.15355188	0.13012	1.12204119	0.33982	0.00392	6.09592	0.0755	0.93138543	2100	20	1886	19	1990	11	11.3%	2100	20
Tail16-7	11020616	29	34	72	0.48	2.6678761	1.1498546	0.12778	1.11128502	0.37483	0.00431	6.60306	0.08121	0.93492906	2068	19	2052	20	2060	11	0.8%	2068	19
Tail16-8	12020616	105	107	164	0.65	1.84474616	1.14374262	0.19592	1.06676194	0.54208	0.0062	14.64111	0.17438	0.96029714	2793	17	2792	26	2792	11	0.0%	2793	17
Tail16-9	16020616	74	76	127	0.60	1.99896054	1.13940751	0.17574	1.07545237	0.50026	0.0057	12.12029	0.14468	0.95451683	2613	18	2615	24	2614	11	-0.1%	2613	18
Tail1	1702	288	55	663	0.08	2.331	1.133	0.161	1.065	0.42	0.00	9.54	0.11	0.958	2470	18	2300	22	2391	11	7.4%	2470	18

-10	0616					9264	31623	38	80741	883	486	037	276	87338									
Tail10-11	18020616	23	24	215	0.11	8.72600349	1.14310646	0.06511	1.21333129	0.1146	0.00131	1.02863	0.01346	0.87357622	778	25	699	8	718	7	2.7%	699	8
Tail10-12	19020616	47	123	587	0.21	12.0685494	1.13444364	0.058	1.17241379	0.08286	0.00094	0.66253	0.00841	0.89370148	529	26	513	6	516	5	0.6%	513	6
Tail10-13	20020616	63	50	144	0.35	2.50972519	1.13439578	0.18219	1.08677754	0.39845	0.00452	10.00788	0.1197	0.94844585	2673	18	2162	21	2436	11	23.6%	2673	18
Tail10-14	21020616	235	71	504	0.14	2.24648425	1.12998158	0.17855	1.07532904	0.44514	0.00503	10.95695	0.12981	0.95379028	2639	18	2374	22	2520	11	11.2%	2639	18
Tail10-15	22020616	50	112	109	1.03	2.74130322	1.13489953	0.1293	1.1136891	0.36479	0.00414	6.5025	0.07929	0.93072067	2088	19	2005	20	2046	11	4.2%	2089	19

Tail1-16	23020616	19	20	44	0.46	2.51768675	1.14302978	0.1349	1.17123795	0.39719	0.00454	7.38685	0.09353	0.90274667	2163	20	2156	21	2159	11	0.3%	2163	20
Tail1-17	27020616	10	33	100	0.33	10.0593502	1.14676592	0.05774	1.45479737	0.09941	0.00114	0.79137	0.01199	0.7568942	520	32	611	7	592	7	-3.1%	611	7
Tail1-18	28020616	57	70	93	0.76	1.95878712	1.12630259	0.18147	1.11313165	0.51052	0.00575	12.77211	0.15443	0.93150687	2666	18	2659	25	2663	11	0.3%	2666	18
Tail1-19	29020616	22	30	50	0.59	2.55251806	1.1307655	0.13277	1.1674324	0.39177	0.00443	7.17108	0.09013	0.89967934	2135	20	2131	21	2133	11	0.2%	2135	20
Tail1-20	30020616	88	132	195	0.67	2.58257793	1.12083882	0.1308	1.11620795	0.38721	0.00434	6.98256	0.08438	0.9275094	2109	19	2110	20	2109	11	-0.1%	2109	19
Tail1-21	310206	16	23	83	0.27	5.343307	1.132781	0.07852	1.273560	0.18715	0.00212	2.02585	0.02721	0.843382	1160	25	1106	12	1124	9	4.9%	1160	25

Tail1-22	16 32020616	98	94	225	0.42	512.53556125	191.11818251	0.14185	881.12090236	0.39439	0.00441	7.7129	0.09323	870.92507024	2250	19	2143	20	2198	11	5.0%	2250	19
Tail1-23	33020616	28	60	177	0.34	6.55007533	1.12006288	0.06968	1.20551091	0.15267	0.00171	1.4669	0.01888	0.87011919	919	25	916	10	917	8	0.1%	916	10
Tail1-24	34020616	93	707	836	0.85	10.5988341	1.11287758	0.06127	1.15880529	0.09435	0.00105	0.79691	0.00985	0.90036881	649	25	581	6	595	6	2.4%	581	6
Tail1-25	38020616	15	40	165	0.24	11.1395789	1.12509747	0.06029	1.37667938	0.08977	0.00101	0.74622	0.01064	0.78906977	614	29	554	6	566	6	2.1%	554	6
Tail1-26	39020616	125	1355	1164	1.16	11.9402985	1.11044776	0.05898	1.1698881	0.08375	0.00093	0.68101	0.00843	0.89706528	566	25	519	6	527	5	1.7%	519	6
Tail1-	40020	13	108	128	0.84	11.948	1.1351	0.058	1.5192	0.083	0.000	0.675	0.01	0.7307	552	33	518	6	524	6	1.2%	518	6

27	616					8589	4159	58	8986	69	95	96	05	7173									
Tail1-28	41020616	40	56	92	0.61	2.67845185	1.11423597	0.1295	1.18918919	0.37335	0.00416	6.66599	0.08372	0.88718178	2091	21	2045	20	2068	11	2.3%	2091	21
Tail1-29	5020616	108	100	158	0.63	1.75318642	1.11853293	0.21105	1.05662165	0.57039	0.00638	16.59605	0.19241	0.96477462	2914	17	2909	26	2912	11	0.1%	2914	17
Tail1-30	6020616	234	183	352	0.52	1.7522034	1.11615356	0.21053	1.04973163	0.57071	0.00637	16.56472	0.19097	0.96815056	2910	17	2911	26	2910	11	0.0%	2910	17
Tail1-31	7020616	58	42	107	0.39	2.02835642	1.11762439	0.17461	1.07095814	0.49301	0.00551	11.86836	0.13859	0.95709421	2602	18	2584	24	2594	11	0.7%	2602	18
Tail1-32	8020616	507	167	1178	0.14	2.38509791	1.11145563	0.1567	1.05296745	0.41927	0.00466	9.05757	0.10412	0.96687352	2420	18	2257	21	2344	11	7.2%	2420	18
Tail	902	44	246	321	0.	8.24	1.11	0.06	1.13	0.1	0.0	1.0	0.0	0.91	750	24	738	8	741	6	0.4%	738	8

1-33	0616				77	742268	340206	426	600996	2125	0135	7425	1312	164037									
Tail1-34	10020616	8	25	42	0.59	5.77834277	1.13833353	0.07439	1.41148004	0.17306	0.00197	1.77493	0.026	0.77710089	1052	28	1029	11	1036	10	2.2%	1052	28
Tail1-35	11020616	56	53	136	0.39	2.63449075	1.11438959	0.12835	1.08297624	0.37958	0.00423	6.71674	0.07894	0.94819675	2076	19	2074	20	2075	10	0.1%	2076	19
Tail1-36	12020616	22	127	234	0.54	11.3494496	1.11224606	0.05808	1.22245179	0.08811	0.00098	0.70546	0.00915	0.85753563	532	27	544	6	542	5	-0.4%	544	6
Tail1-37	16020616	125	120	211	0.57	1.97456757	1.10575784	0.18435	1.07404394	0.50644	0.0056	12.87199	0.14962	0.95129688	2692	18	2641	24	2670	11	1.9%	2692	18
Tail1-38	17020616	19	62	188	0.33	9.7599063	1.11262932	0.06101	1.22930667	0.10246	0.00114	0.86186	0.01124	0.8531412	640	26	629	7	631	6	0.4%	629	7

								1.		1.					0.																
	1					3.	1		0					9																
T	8					0	0		6	0	0		0	5																
a	0					0	2	0.	8	.	.	5	.	3																
il	2					4	5	1	8	3	0	.	0	1																
1	0					1	3	1	9	3	0	4	6	1	1		1		1			1	9						
-	6	4	1	1	0	7	2	9	3	2	3	9	3	7	9		8		9			5.	5						
3	1	0	2	2	.	5	5	7	5	8	6	5	5	4	5	1	5	1	0	1		4	2	1	9	2	1	8	1	9	1
9	6	1	2	0	1	8	2	5	3	7	7	5	5	2	2	9	2	8	0	0		%	2	9	2	8	5	0	2	9	9
						3.	1.		1.					0.																
	1					0	1		0					9																
T	9					2	0		7	0	0	5	0	5																
a	0					4	0		2	.	.	.	.	1																
il	2					3	8	0.	6	3	3	0	6	4																
1	0					4	6	1	3	3	0	3	2	6	1		1		1			1	9						
-	6	5	1	1	0	5	1	1	5	0	3	9	4	2	9		8		8			4.	3						
4	1	5	6	6	.	9	9	8	1	1	6	7	4	0	3	1	4	1	5	1	0	9	2	1	9	2	1	8	1	9	1
0	6	2	9	0	1	4	4	4	4	5	4	8	5	2	2	9	2	8	5	0		%	2	9	2	8	5	0	2	9	9
						4.	1.		1.					0.																
	2					4	1		0					9																
T	0					1	0		9	0		2	0	4																
a	0					4	3	0.	1	.	0	.	.	2																
il	2					0	5	0	0	2	.	7	0	5																
1	0					3	0	8	7	2	0	1	3	8	1		1		1			1							
-	6	1			5	6	9	7	6	6	0	9	1	5	3		3		3			3.	1						
4	1	2	6	8	8	6	1	0	1	5	2	6	8	3	6	2	1	6	3	4	9	5	3	6	2	1	6	3	4	9	1
6	6	9	8	4	2	4	6	7	5	5	5	5	8	4	6	2	1	6	3	4	9	%	2	1	6	3	4	9	2	1	6
						1	1.		1.					0.																
	2					0.	1		3					8																
T	1					7	1		4		0	0	0	0																
a	0					6	9	0.	2	0	.	.	.	3																
il	2					4	4	0	1	.	0	7	0	8																
1	0					2	8	6	7	0	0	9	1	6																
-	6				1	6	3	1	3	9	1	2	1	6	6		5		5			3.	5						
4	1	1	8	1	2	6	2	3	3	2	0	0	1	6	6	2	7	6	9	6		4	7						
2	6	3	0	2	2	6	2	4	5	9	4	3	3	6	9	8	3	6	2	6		%	3	6							
						1	1.		1.					0.																
	2					0.	1		3					8																
T	2					8	1		1		0	0	0	1																
a	0					5	8	0.	6	0	.	.	.	1																
il	2					7	3	0	6	.	0	7	0	2																
1	0					7	4	6	4	0	0	8	1	4																
-	6				0	6	9	1	4	9	1	1	0	4	6		5		5			3.	5						
4	1	1	8	1	.	6	3	6	5	2	0	2	7	7	6	2	6	6	8	6		2	6							
3	6	4	2	3	6	3	3	2	2	9	1	3	5	9	5	8	8	6	6	6		%	8							
T						2.	1.		1.	0	0		0																	
a	2					0	0	0.	0	.	.	1	.	0.																
il	3					4	9	1	8	4	0	1	1	9																
1	0					3	7	7	7	8	0	.	3	4	2		2		2			2							
-	2	3	1	6	0	7	5	1	6	9	5	5	5	2	5		5		5			0.	5						
4	0	3	2	3	.	7	0	9	5	2	3	9	0	7	7	1	6	2	7	1		3	7	1						
4	6	0	5	1	0	7	8	3	1	9	7	8	2	5	7	8	8	3	3	1		%	7	8						

	16					72	63		95			16		52									
Tail1-45	27020616	47	49	106	0.46	2.50865486	1.09879083	0.13428	1.13196306	0.39862	0.00438	7.37958	0.08856	0.91560691	2155	20	2163	20	2159	11	-0.4%	2155	20
Tail1-46	28020616	35	22	54	0.42	1.77717749	1.10895875	0.21384	1.15506921	0.56269	0.00624	16.58902	0.2023	0.9093692	2935	19	2878	26	2911	12	2.0%	2935	19
Tail1-47	29020616	145	189	326	0.58	2.58024564	1.09402415	0.13102	1.11433369	0.38756	0.00424	7.00082	0.08296	0.92322398	2112	19	2112	20	2112	11	0.0%	2112	19
Tail1-48	30020616	27	29	75	0.38	2.97769705	1.10174791	0.12479	1.16996554	0.33583	0.0037	5.77785	0.0713	0.89280984	2026	21	1867	18	1943	11	8.5%	2026	21
Tail1-49	31020616	13	30	78	0.39	6.3500127	1.11125222	0.07035	1.3503909	0.15748	0.00175	1.52737	0.02126	0.79835057	939	27	943	10	941	9	-0.1%	943	10
Tail1-	32020	23	50	304	0.16	12.938	1.0997	0.056	1.2651	0.077	0.000	0.597	0.007	0.8398	457	27	480	5	476	5	-0.8%	480	5

50	616					2844	5417	12	4612	29	85	97	83	72229									
Tail1-51	33020616	61	49	101	0.49	1.93824744	1.0951098	0.183	1.1420765	0.51593	0.00565	13.01647	0.15679	0.90914369	2680	19	2682	24	2681	11	-0.1%	2680	19
Tail1-52	34020616	8	27	63	0.42	8.93894699	1.11736837	0.06297	1.55629665	0.11187	0.00125	0.97112	0.01535	0.70690474	707	33	684	7	689	8	0.8%	684	7
Tail1-53	38020616	90	103	191	0.54	2.56614232	1.09061049	0.17177	1.17016941	0.38969	0.00425	9.22791	0.11279	0.8922826	2575	19	2121	20	2361	11	21.4%	2575	19
Tail1-54	39020616	301	50	605	0.08	2.12084579	1.08587305	0.17424	1.15358127	0.47151	0.00512	11.3258	0.1367	0.8996621	2599	19	2490	22	2550	11	4.4%	2599	19
Tail1-55	40020616	63	98	163	0.60	3.00480769	1.08774038	0.11602	1.18945009	0.3328	0.00362	5.32292	0.06576	0.88046762	1896	21	1852	18	1873	11	2.4%	1896	21
Tail	410	10	28	43	0.	5.09	1.10	0.08	1.43	0.1	0.0	2.2	0.0	0.76	12	28	11	12	11	10	7.2%	12	28

1-56	20616				64	087207	981011	175	119266	9643	0218	1373	3216	393655	40		56		85			40	
Tail1-57	5020616	23	73	252	0.29	10.8003024	1.09083054	0.06088	1.19908016	0.09259	0.00101	0.77713	0.00972	0.87213698	635	25	571	6	584	6	2.3%	571	6
Tail1-58	6020616	22	68	178	0.38	8.45165652	1.09026369	0.06366	1.19384229	0.11832	0.00129	1.03839	0.01304	0.86818935	730	25	721	7	723	7	0.3%	721	7
Tail1-59	7020616	3	19	31	0.60	10.7100782	1.15668844	0.06147	1.98470799	0.09337	0.00108	0.79126	0.01572	0.58221457	656	42	576	6	592	9	2.8%	576	6
Tail1-60	8020616	486	35	933	0.04	1.9629397	1.08354271	0.18444	1.04641076	0.50944	0.00552	12.95413	0.14505	0.96769067	2693	17	2654	24	2676	11	1.5%	2693	17
Tail1-61	9020616	115	237	263	0.90	2.76250725	1.08566535	0.12668	1.0656773	0.36199	0.00393	6.32207	0.07178	0.95620679	2052	19	1992	19	2022	10	3.1%	2052	19

Tail1-62	10020616	131	283	291	0.97	2.74529182	1.08439027	0.12632	1.06079797	0.36426	0.00395	6.34323	0.07199	0.95548505	2047	19	2002	19	2024	10	2.2%	2047	19
Tail1-63	11020616	23	32	56	0.58	2.7109087	1.09520711	0.12873	1.13415676	0.36888	0.00404	6.54657	0.07812	0.91779954	2081	20	2024	19	2052	11	2.8%	2081	20
Tail1-64	12020616	107	90	216	0.42	2.25204936	1.08548779	0.1696	1.06721698	0.44404	0.00482	10.38235	0.11794	0.95556335	2554	18	2369	22	2470	11	7.8%	2554	18
Tail1-65	16020616	39	30	76	0.40	2.15090768	1.0926611	0.16248	1.11398326	0.46492	0.00508	10.41405	0.12273	0.9271594	2482	19	2461	22	2472	11	0.8%	2482	19
Tail1-66	17020616	42	285	357	0.80	9.65996909	1.09157651	0.06222	1.15718419	0.10352	0.00113	0.88793	0.01081	0.89661751	682	25	635	7	645	6	1.6%	635	7
Tail1-67	180206	96	66	188	0.35	2.143944	1.084835	0.17439	1.078043	0.46643	0.00506	11.213	0.12812	0.949517	2600	18	2468	22	2541	11	5.4%	2600	18

	16					43	88		47			88		59									
Tail1-68	19020616	464	280	1726	0.16	3.78615781	1.08284113	0.13661	1.06873582	0.26412	0.00286	4.97422	0.05655	0.95248276	2185	18	1511	15	1815	10	44.6%	2185	18
Tail1-69	20020616	164	141	304	0.46	2.11010529	1.08248402	0.1828	1.07221007	0.47391	0.00513	11.94315	0.13606	0.95018881	2678	18	2501	22	2600	11	7.1%	2678	18
Tail1-70	21020616	23	61	217	0.28	9.48316738	1.10047742	0.06413	1.29424606	0.10545	0.00116	0.93228	0.01246	0.82307561	746	27	646	7	669	7	3.5%	646	7
Tail1-71	22020616	39	47	104	0.45	2.91027619	1.08844329	0.12775	1.11937378	0.34361	0.00374	6.05168	0.07129	0.92395995	2067	20	1904	18	1983	10	8.6%	2067	20
Tail1-72	23020616	50	120	116	1.03	2.93341156	1.08829569	0.12642	1.11532985	0.3409	0.00371	5.94114	0.06985	0.92565741	2049	20	1891	18	1967	10	8.3%	2049	20
Tail1-	27020	63	85	155	0.55	2.7441	1.0866	0.132	1.1196	0.364	0.003	6.640	0.078	0.9207	2127	19	2003	19	2065	10	6.2%	2127	19

73	616					618	8807	19	0057	41	96	86	38	1234									
Tail1-74	28020616	22	60	74	0.81	4.04138377	1.095215	0.09353	1.21886026	0.24744	0.00271	3.19047	0.04052	0.86235207	1499	23	1425	14	1455	10	5.1%	1499	23
Tail1-75	29020616	36	81	181	0.45	5.30222694	1.08695652	0.08049	1.16784694	0.1886	0.00205	2.09268	0.0255	0.89202046	1209	23	1114	11	1146	8	8.5%	1209	23
Tail1-76	30020616	62	344	708	0.49	12.0816721	1.08735049	0.05916	1.1663286	0.08277	0.0009	0.67505	0.0082	0.8951414	573	25	513	5	524	5	2.2%	513	5
Tail1-77	31020616	27	166	308	0.54	12.0525491	1.08472942	0.05785	1.22731201	0.08297	0.0009	0.66169	0.00842	0.85244015	524	27	514	5	516	5	0.4%	514	5
Tail1-78	32020616	158	74	265	0.28	1.87476565	1.08173978	0.21519	1.10599935	0.5334	0.00577	15.82409	0.18452	0.9276798	2945	18	2756	24	2866	11	6.9%	2945	18
Tail	330	63	53	112	0.	2.04	1.08	0.17	1.12	0.4	0.0	12.	0.1	0.91	26	19	25	23	26	11	3.0%	26	19

1-79	20616				48	006691	53156	957	490951	9018	0532	13494	4371	64456	49		71		15			49	
Tail1-80	34020616	22	80	281	0.28	12.6454224	1.08750632	0.05693	1.26471105	0.07908	0.00086	0.62067	0.0081	0.83331179	488	28	491	5	490	5	-0.1%	491	5
Tail1-81	38020616	386	275	801	0.34	2.30266188	1.07994842	0.17348	1.12404888	0.43428	0.00469	10.38632	0.12284	0.9131138	2592	19	2325	21	2470	11	11.5%	2592	19
Tail1-82	39020616	38	86	111	0.78	3.44174841	1.0875925	0.10991	1.18278592	0.29055	0.00316	4.4025	0.05436	0.88081787	1798	21	1644	16	1713	10	9.3%	1798	21
Tail1-83	40020616	23	38	58	0.65	2.88550323	1.09360572	0.12988	1.20880813	0.34656	0.00379	6.20527	0.07793	0.87079671	2096	21	1918	18	2005	11	9.3%	2096	21
Tail1-84	41020616	63	214	165	1.30	3.41425108	1.09256035	0.10432	1.23657975	0.29289	0.0032	4.21243	0.05398	0.85259985	1702	23	1656	16	1676	11	2.8%	1702	23

Tail2-1	5020616	7	34	98	0.35	13.3031795	1.1041639	0.0553	1.51898734	0.07517	0.00083	0.57309	0.00889	0.71179447	424	34	467	5	460	6	-1.5%	467	5
Tail2-2	6020616	20	40	281	0.14	13.2327643	1.08508667	0.05647	1.31043032	0.07557	0.00082	0.58828	0.00797	0.80092194	470	29	470	5	470	5	0.0%	470	5
Tail2-3	7020616	11	67	144	0.47	13.5098622	1.09429884	0.0578	1.4532872	0.07402	0.00081	0.58983	0.00873	0.7393474	522	32	460	5	471	6	2.3%	460	5
Tail2-4	8020616	23	19	334	0.06	13.4102186	1.08622771	0.05778	1.28071997	0.07457	0.00081	0.59404	0.00783	0.8240903	521	28	464	5	473	5	2.1%	464	5
Tail2-5	9020616	38	192	368	0.52	10.3316458	1.08482281	0.06086	1.1666119	0.09679	0.00105	0.81208	0.00994	0.88628059	634	25	596	6	604	6	1.4%	596	6
Tail2-6	100206	20	57	273	0.21	13.19783	1.082222	0.05638	1.241575	0.07577	0.00082	0.58898	0.00761	0.8375911	467	28	471	5	470	5	-0.1%	471	5

	16					56	52		03					88															
						1	1.		1.					0.															
	11					3.	08		2					86															
	10					26	79	0.	13	0	0	0	0	5															
Tail	20					78	60	05	50	.	.	.	.	1															
2-	61				3	76	03	06	68	07	00	59	00	16	48		46		47		0.	46	
7	6	28	44	91	11	85	3	86	6	53	82	1	43	03	5	27	8	5	1	5	%	8	5
						1	1.		1.					0.															
	12					3.	07		1					90															
Tail	20					26	44		32	0	0	0	0	5														
2-	61		15	11	1	43	13	0.	40	.	.	.	.	4															
8	6	118	72	80	3	87	05	074	07	00	59	00	07	20	50	25	46	5	47	5	1.	46	
						1	1.		1.					0.															
	16					3.	09		27	0	0		0	82															
Tail	02					17	38	0.	13	.	.	0	.	9															
2-	06				26	87	05	07	30	00	00	.	00	62															
9	16	19	34	5	13	03	74	2	40	88	83	07	92	66	50	28	47	5	47	5	1.	47	
						1	1.		1.					0.															
	17					0.	08		1					88															
Tail	02					57	9	0.	82	0	0	0	0	2															
2-	06					86	06	00	34	.	.	.	.	7															
10	16	36	153	369	0.41	65	10	6	80	0	0	7	0	12	60	25	58	6	58	6	0.	58	
						23	18	05	4	45	33	8	96	31	5	5	2		7		8	%	2	6
						1	1.		1.					0.															
	18					4.	0		1					90															
Tail	02					03	81	0.	33	0	0	0	0	4															
2-	06					9	0	00	10	.	.	.	.	3															
11	16	68	137	1006	0.14	0	0	5	0	0	0	5	0	1	47		44		44		1.	44	
						28	56	4	47	0	0	5	0	0	0	25	4	5	8	4	%	4	5
						1	1.		1.	0	0	0	0	0.															
Tail	19					1.	0	0.	1	.	.	.	.	9															
2-	02			12	0.	19	85	08	12	0	0	7	0	23	57		55		55		0.	55	
	0	112	451	19	37	0	4	0	6	89	0	30	08	4	9	24	5	6	7	5	%	2	6

12	616					6893	9687	32	0958	36	97	79	59	8109									
Tail2-13	20020616	39	69	457	0.15	11.3947129	1.09389243	0.05734	1.23822811	0.08776	0.00096	0.69385	0.00895	0.84804164	504	27	542	6	535	5	-1.3%	542	6
Tail2-14	21020616	22	287	233	1.23	11.2120193	1.09877789	0.06126	1.27326151	0.08919	0.00098	0.75323	0.00993	0.83346674	648	27	551	6	570	6	3.5%	551	6
Tail2-15	22020616	43	52	518	0.10	11.5326952	1.08407335	0.05797	1.17302053	0.08671	0.00094	0.69298	0.00853	0.88070475	528	26	536	6	535	5	-0.3%	536	6
Tail2-16	23020616	73	674	1020	0.66	15.6396622	1.07913669	0.05661	1.14820703	0.06394	0.00069	0.49904	0.00605	0.89013616	476	26	400	4	411	4	2.9%	400	4
Tail2-17	27020616	26	49	322	0.15	12.0221207	1.09401298	0.05746	1.2530456	0.08318	0.00091	0.65897	0.00858	0.84023512	597	27	515	5	514	5	-0.2%	515	5
Tail	280	103	54	337	0.	3.39	1.09	0.14	1.13	0.2	0.0	5.9	0.0	0.90	22	19	16	16	19	10	37.	22	19

2-18	20616				16	40875	289617	553	378685	9463	0322	1126	7101	978643	94		65		63		8%	94	
Tail2-19	29020616	59	290	754	0.38	13.1268049	1.08952481	0.0579	1.22625216	0.07618	0.00083	0.60813	0.00778	0.85163589	526	27	473	5	482	5	1.9%	473	5
Tail2-20	30020616	10	43	108	0.40	11.5713955	1.11085397	0.05892	1.47657841	0.08642	0.00096	0.70198	0.01061	0.73496444	564	31	534	6	540	6	1.1%	534	6
Tail2-21	31020616	38	52	540	0.10	13.1095962	1.10120608	0.05686	1.21350686	0.07628	0.00084	0.59796	0.00766	0.8596308	486	27	474	5	476	5	0.4%	474	5
Tail2-22	32020616	205	532	2355	0.23	11.2258644	1.08890885	0.06111	1.14547537	0.08908	0.00097	0.75041	0.00913	0.89499243	643	25	550	6	569	5	3.3%	550	6
Tail2-23	33020616	25	48	92	0.52	3.99840064	1.10755698	0.10997	1.24579431	0.2501	0.00277	3.79188	0.04929	0.85204365	1799	22	1439	14	1591	10	25.0%	1799	22

	3					1	1.		1.					0.															
	4					3.	1		2					8															
Tail	0					7	0		1	0		0	0	6															
20-	2					8	3	0.	7	.	0	.	.	4															
24	06	55	71	822	0.09	9	1	05	1	07	.0	56	00	7	479	27	451	5	456	5	1.0%	45	15						
						1	1.		1.					0.															
	3					3.	1		1					8															
Tail	8					8	0		8	0		0		7															
20-	0					0	4	0.	4	.	0	.	0	9															
25	2					8	6	0	1	0	.	5	.	0															
	06	186	133	2795	0.05	3	6	56	6	70	0	64	00	3	475	26	451	5	455	5	0.9%	45	15						
						1	1.							0.															
	3					1.	1		1.					8															
Tail	9					2	0		2	0	0			3															
20-	0					9	6	0.	7	.	.	0	0	0															
26	2					3	7	0	8	0	0	.	.	6															
	06	67	50	817	0.06	0	1	06	0	08	0	7	00	0	612	27	547	6	560	6	2.3%	54	76						
						1	1.							0.															
	4					5.	1		1.					8															
Tail	0					7	0		3	0		0	0	1															
20-	2					8	4	0.	1	.	0	.	.	1															
27	06	44	216	679	0.32	2	7	05	0	00	.	49	00	8	469	29	396	4	407	5	2.8%	39	64						
						1	1.		1.																				
	4					3.	1		3					0.															
Tail	1					6	0		3	0	0	0	0	7															
20-	0					3	4	0.	4	.	.	.	.	9															
28	2					6	5	0	9	0	0	5	0	3															
	06	23	84	317	0.26	9	9	05	9	07	0	56	00	1	459	30	456	5	457	5	0.1%	45	65						

Table 8

Th (ppm)	U (ppm)	Radiogenic isotopic ratios								Apparent ages (Ma)				Err R8 %	Err 7/6 %	Conc. (%)
		Th/U	208Pb/206Pb	207Pb/206Pb	±1σ	207Pb/235U	±1σ	206Pb/238U	±1σ	206Pb/238U	±1σ	207Pb/206Pb	±1σ			
14231	2076	6.86	2.13	0.0687	0.0012	0.5188	0.0110	0.0548	0.0006	344	4	888	37	1.1	1.8	38.7
4818	1350	3.57	1.17	0.1110	0.0026	0.8645	0.0241	0.0565	0.008	354	5	1816	42	1.5	2.4	19.5
20181	2940	6.86	2.17	0.0546	0.0013	0.4107	0.0108	0.0545	0.007	342	4	397	51	1.3	2.3	86.3
15072	2680	5.62	1.76	0.0555	0.0013	0.4089	0.0106	0.0534	0.007	335	4	434	49	1.3	2.3	77.3
11744	2829	4.15	1.90	0.1220	0.0027	0.9711	0.0253	0.0577	0.008	362	5	1986	39	1.4	2.2	18.2
10200	1702	5.99	1.84	0.0974	0.0024	0.7725	0.0219	0.0575	0.008	361	5	1575	45	1.4	2.4	22.9
13930	1912	7.29	2.24	0.0720	0.0016	0.5439	0.0141	0.0548	0.0071	344	4	986	45	1.3	2.2	34.9

Highlights

- A detailed petrostructural evolution of the Belledonne massif is proposed.
- New geochronological and thermo-barometrical constrains allow to refine the history of this area.
- Two main events are responsible of the variscan structuration of the Belledonne massif.

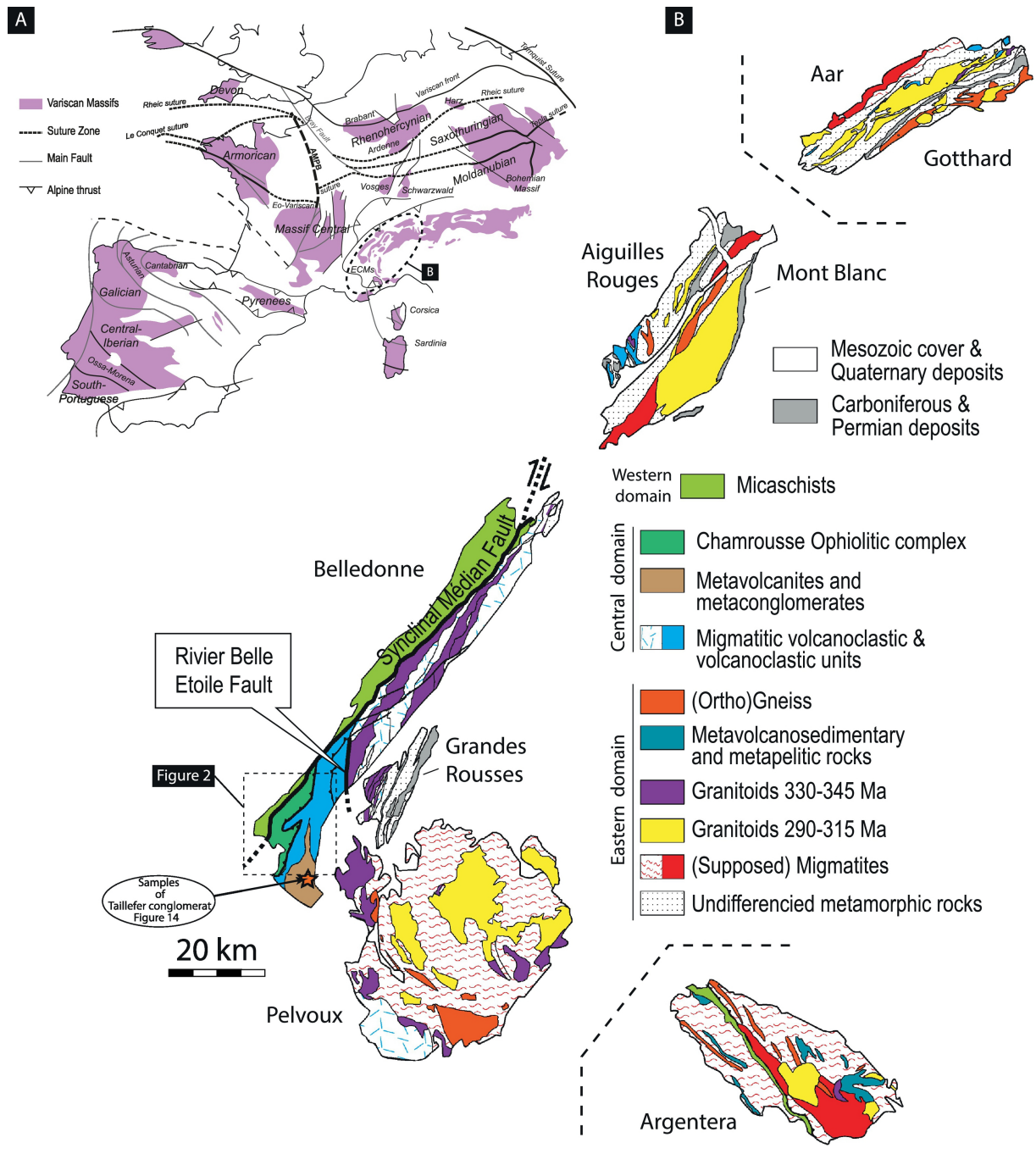
A
Variscan Massifs
Suture Zone
Main Fault
Alpine thrust
Devon
Rheic suture
Le Conquet suture
Armorican
MFB
Eo-Variscan suture
Massif Central
Asturian
Cantabrian
Galician
Central-Iberian
Ossa-Morena
South-Portuguese
Pyrenees
ECMs
B
Corsica
Sardinia
Brabant
Rhenohercynian
Ardenne
Variscan front
Harz
Rheic suture
Saxothuringian
Teplá suture
Moldanubian
Bohemian Massif
Schwarzwald
Vosges
Tornquist Sture
B
Aar
Gotthard
Aiguilles Rouges
Mont Blanc
Mesozoic cover & Quaternary deposits
Carboniferous & Permian deposits
Western domain
Micaschists
Central domain
Chamrousse Ophiolitic complex
Metavolcanites and metaconglomerates
Migmatitic volcanoclastic & volcanoclastic units
Eastern domain
(Ortho)Gneiss
Metavolcanosedimentary and metapelitic rocks
Granitoids 330-345 Ma
Granitoids 290-315 Ma
(Supposed) Migmatites
Undifferencied metamorphic rocks
Belledonne
Synclinal Médian Fault
Rivier Belle Etoile Fault
Figure 2
Grandes Rousses
Samples of Taillefer conglomerat Figure 14
20 km
Pelvoux
Argentera

Figure 1

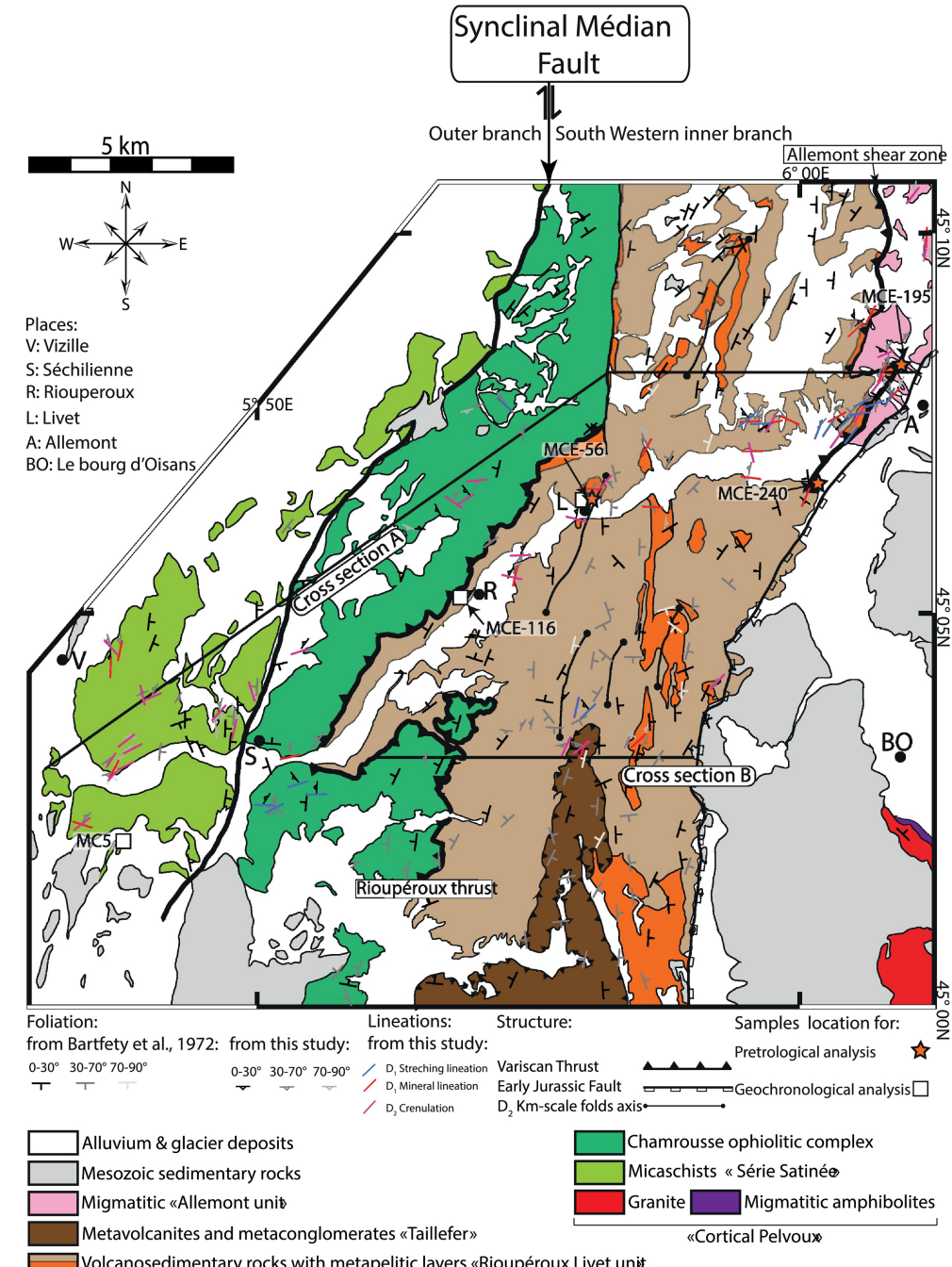
Synclinal Médian Fault
Outer branch
South Western inner branch
Allemont shear zone
6° 00E
5° 50E
45° 10N
45° 05N
45° 00N
5 km
N
W
E
S
Places:
V: Vizille
S: Séchilienne
R: Riouperoux
L: Livet
A: Allemont
BO: Le bourg d'Oisans
MCE-195
MCE-56
MCE-240
MCE-116
MC5
Cross section A
Cross section B
Rioupéroux thrust
Foliation:
from Bartfety et al., 1972:
0-30° 30-70° 70-90°
from this study:
0-30° 30-70° 70-90°
Lineations:
from this study:
D1 Streching lineation
D1 Mineral lineation
D2 Crenulation
Structure:
Variscan Thrust
Early Jurassic Fault
D2 Km-scale folds axis
Samples location for:
Pretrological analysis
Geochronological analysis
Alluvium & glacier deposits
Mesozoic sedimentary rocks
Migmatitic «Allemont unit»
Metavolcanites and metaconglomerates «Taillefer»
Volcanosedimentary rocks with metapelitic layers «Rioupéroux Livet unit»
Chamrousse ophiolitic complex
Micaschists « Série Satinée»
Granite
Migmatitic amphibolites
«Cortical Pelvoux»

Figure 2

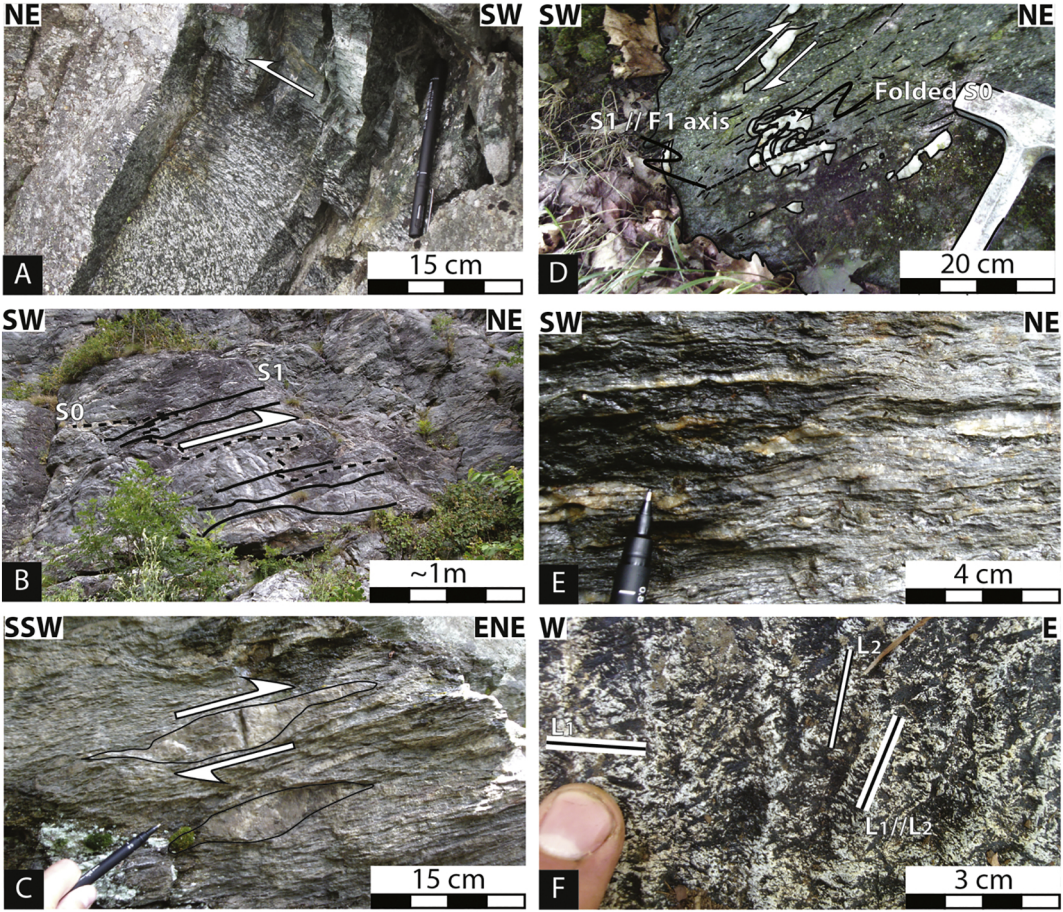
NE
SW
A
15 cm
SW
NE
S1 // F1 axis
Folded S0
D
20 cm
SW
NE
S1
S0
B
~1m
SW
NE
E
4 cm
SSW
ENE
C
15 cm
W
E
L2
L1
L1 / L2
F
3 cm

Figure 3

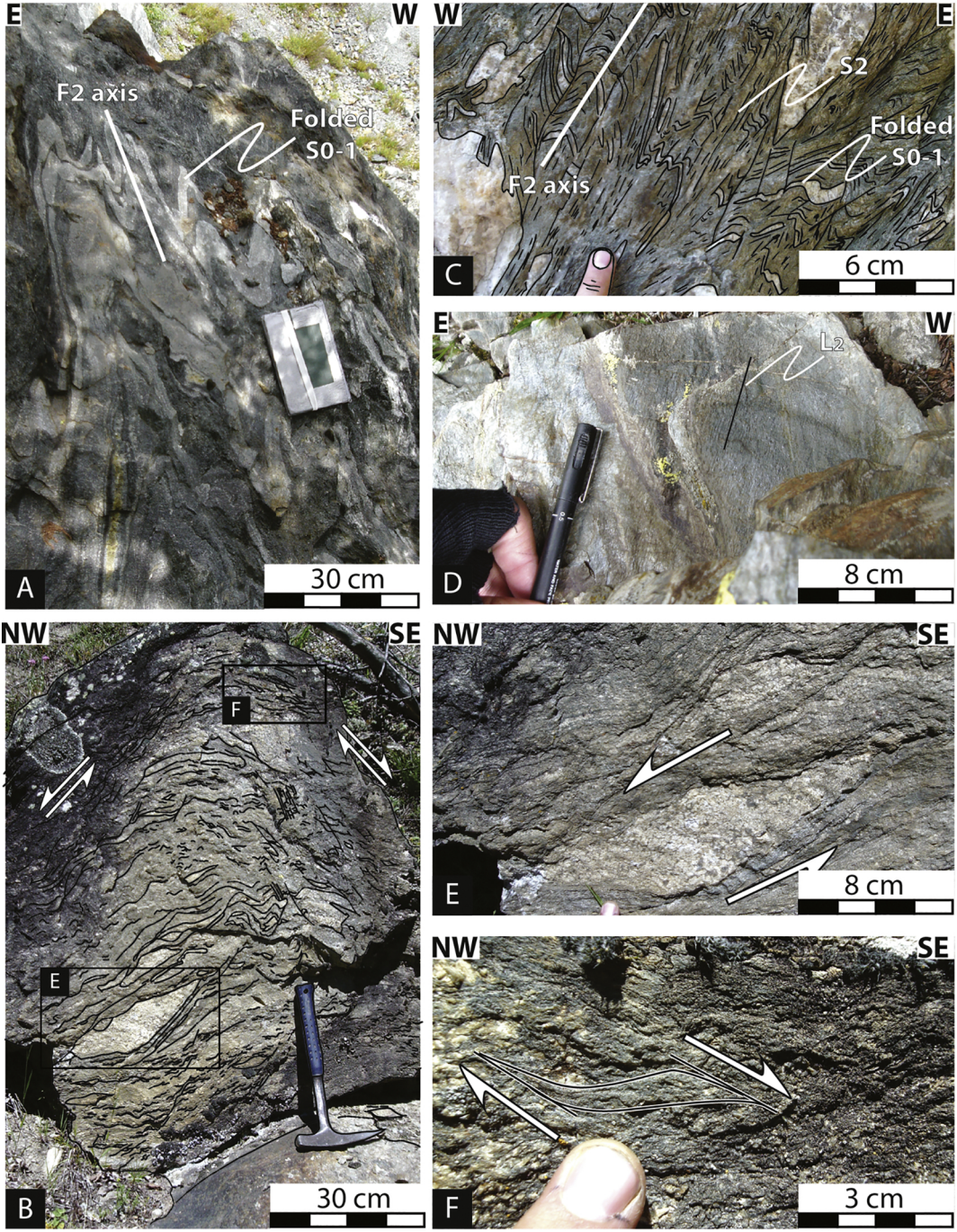
E
W
F2 axis
Folded
S0-1
A
30 cm
W
E
S2
Folded
S0-1
F2 axis
C
6 cm
E
W
L2
D
8 cm
NW
SE
F
E
B
30 cm
NW
SE
E
8 cm
NW
SE
F
3 cm

Figure 4

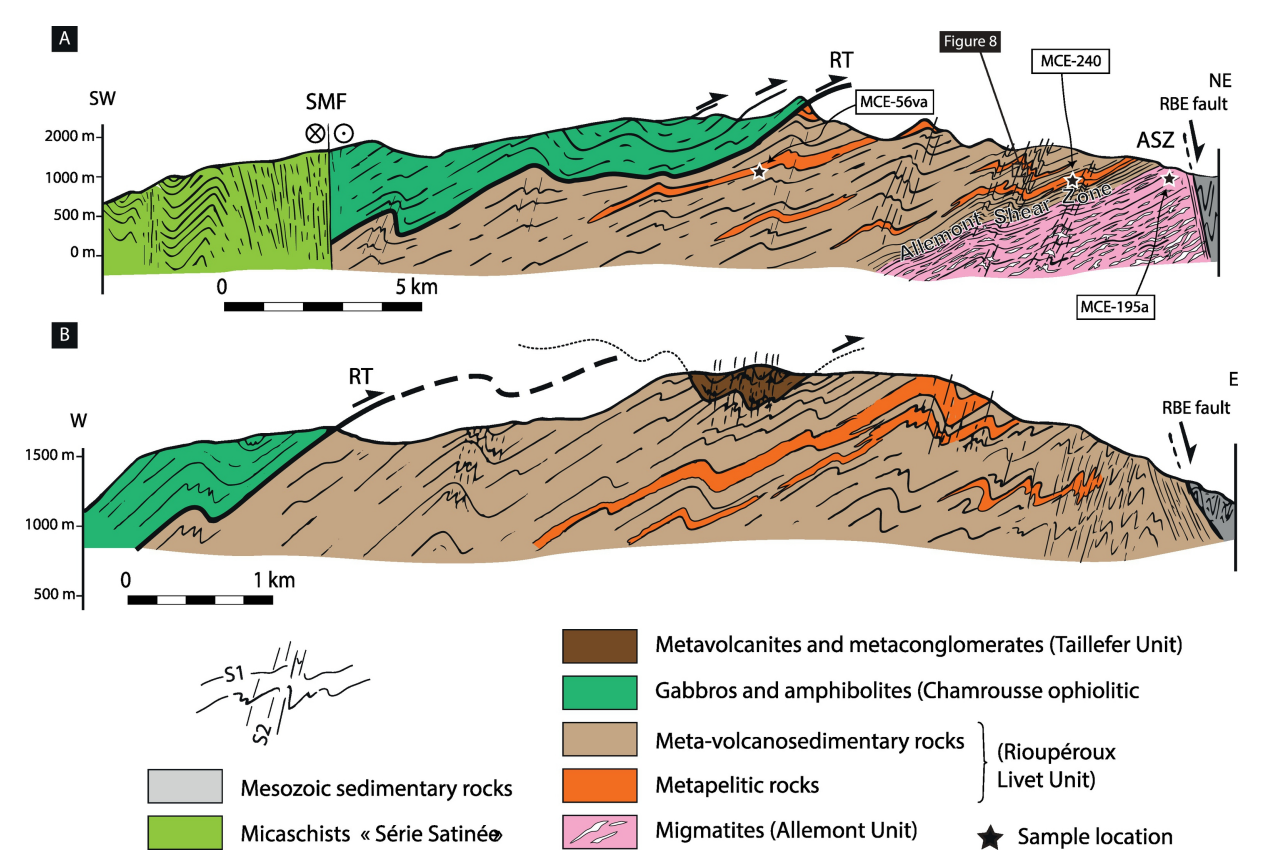
A
SW
SMF
RT
Figure 8
MCE-240
NE
RBE fault
MCE-56va
ASZ
2000 m
1000 m
500 m
0 m
0
5 km
Allemont Shear Zone
MCE-195a
B
RT
E
W
RBE fault
1500 m
1000 m
500 m
0
1 km
S1
S2
Metavolcanites and metaconglomerates (Taillefer Unit)
Gabbros and amphibolites (Chamrousse ophiolitic
Meta-volcanosedimentary rocks
Metapelitic rocks
(Rioupéroux
Livet Unit)
Mesozoic sedimentary rocks
Micaschists « Série Satinée»
Migmatites (Allemont Unit)
Sample location

Figure 5

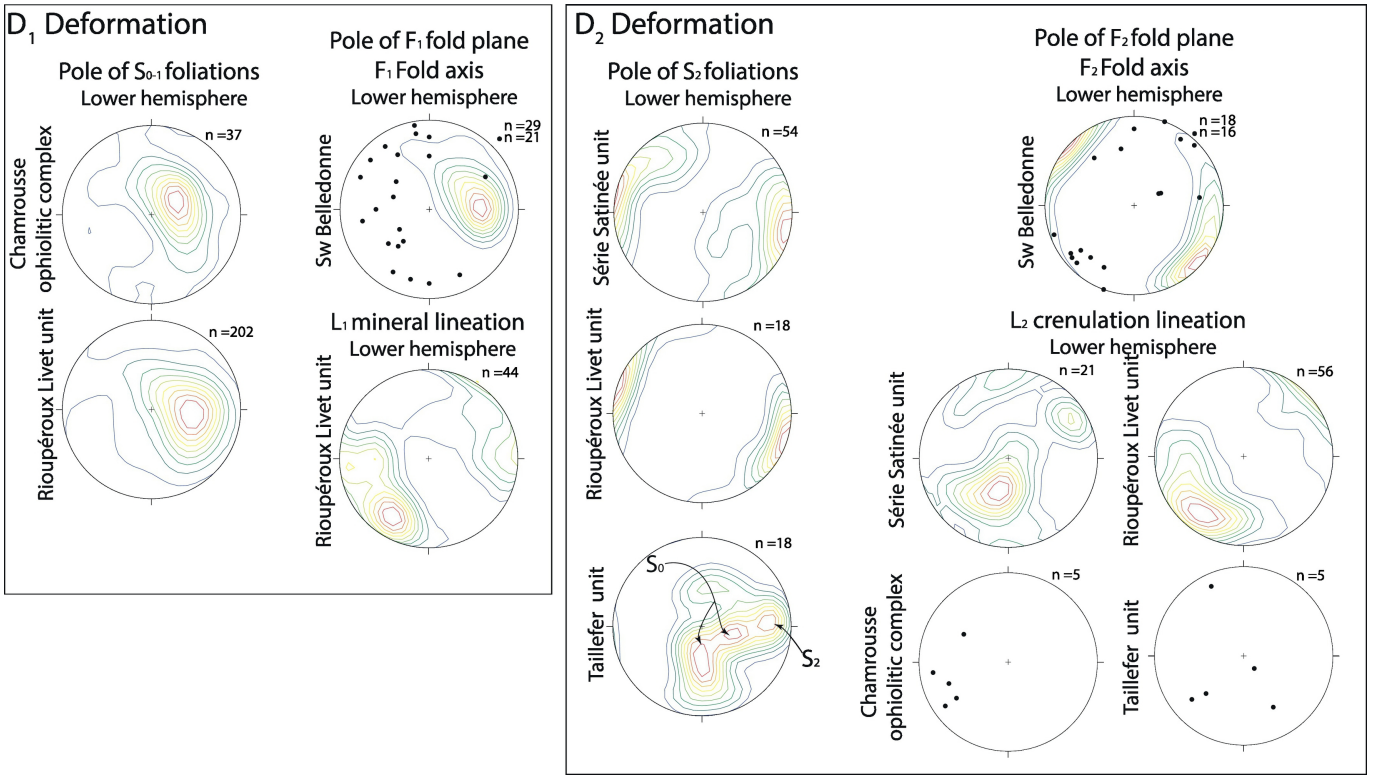
D1 Deformation
Pole of S0-1 foliations
Lower hemisphere
Chamrousse ophiolitic complex
n =37
Rioupéroux Livet unit
n =202
Pole of F1 fold plane
F1 Fold axis
Lower hemisphere
Sw Belledonne
n =29
n =21
L1 mineral lineation
Lower hemisphere
Rioupéroux Livet unit
n =44
D2 Deformation
Pole of S2 foliations
Lower hemisphere
Série Satinée unit
n =54
Rioupéroux Livet unit
n =18
Taillefer unit
n =18
S0
S2
Pole of F2 fold plane
F2 Fold axis
Lower hemisphere
Sw Belledonne
n =18
n =16
L2 crenulation lineation
Lower hemisphere
Série Satinée unit
n =21
Rioupéroux Livet unit
n =56
Chamrousse ophiolitic complex
n =5
Taillefer unit
n =5

Figure 6

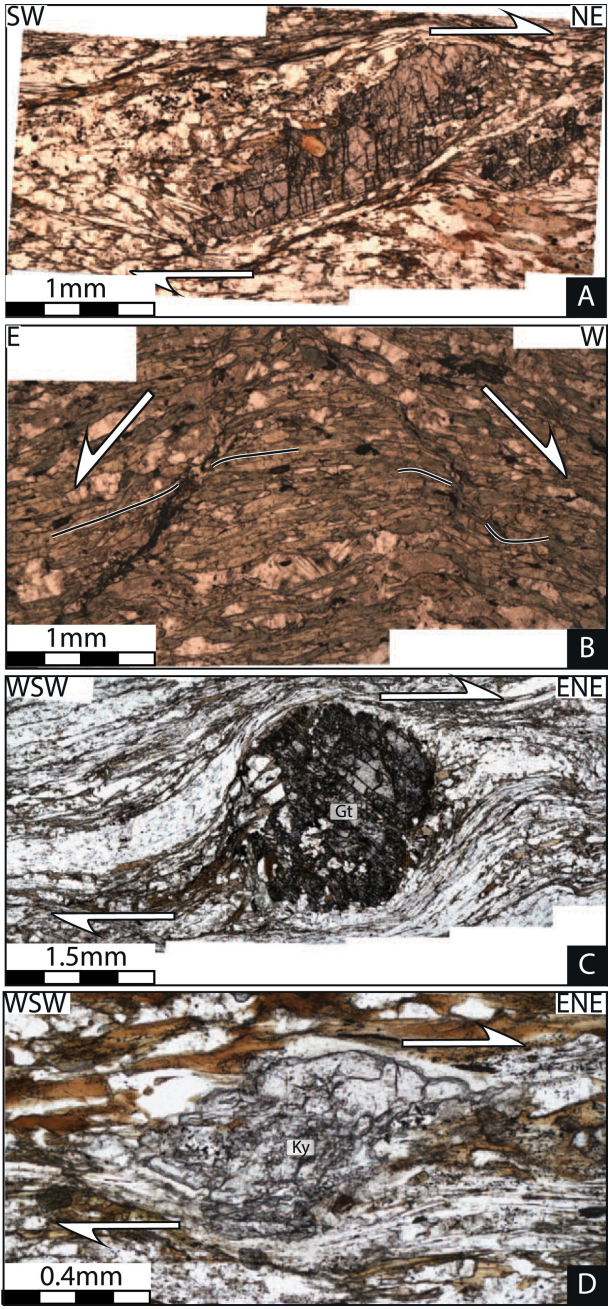

Figure 7

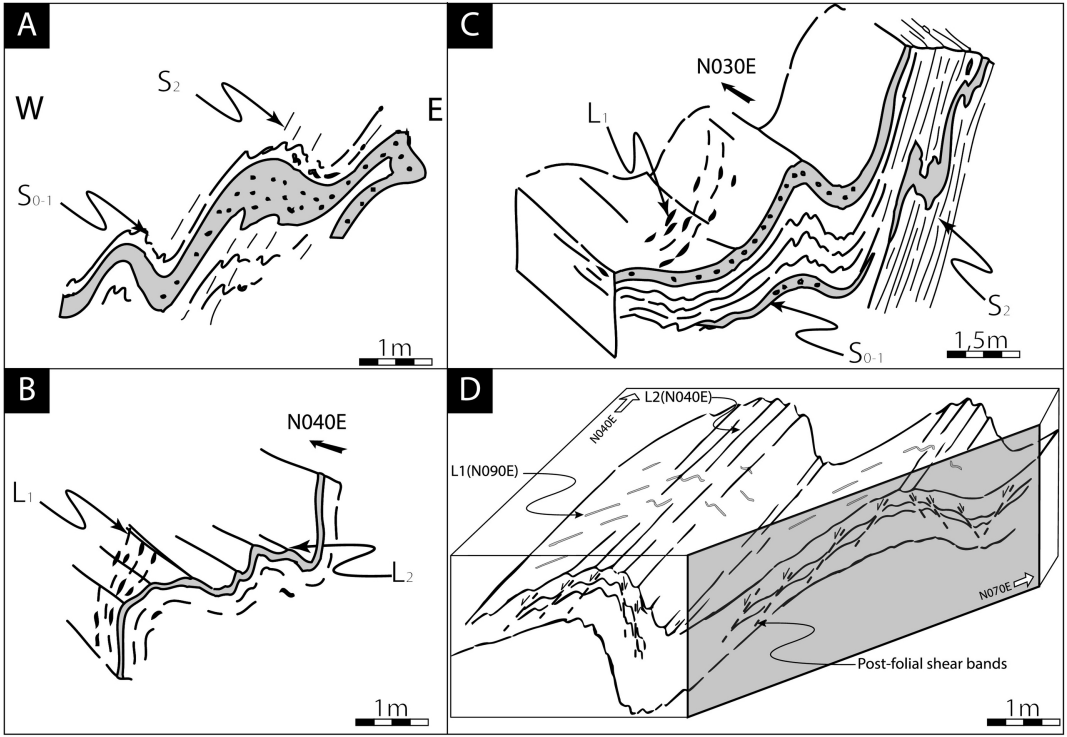
A
W
E
S_2
S_{0-1}
1m
B
N040E
L_1
L_2
1m
C
N030E
L_1
S_2
S_{0-1}
1,5m
D
L2(N040E)
N040E
L1(N090E)
N070E
Post-folial shear bands
1m

Figure 8

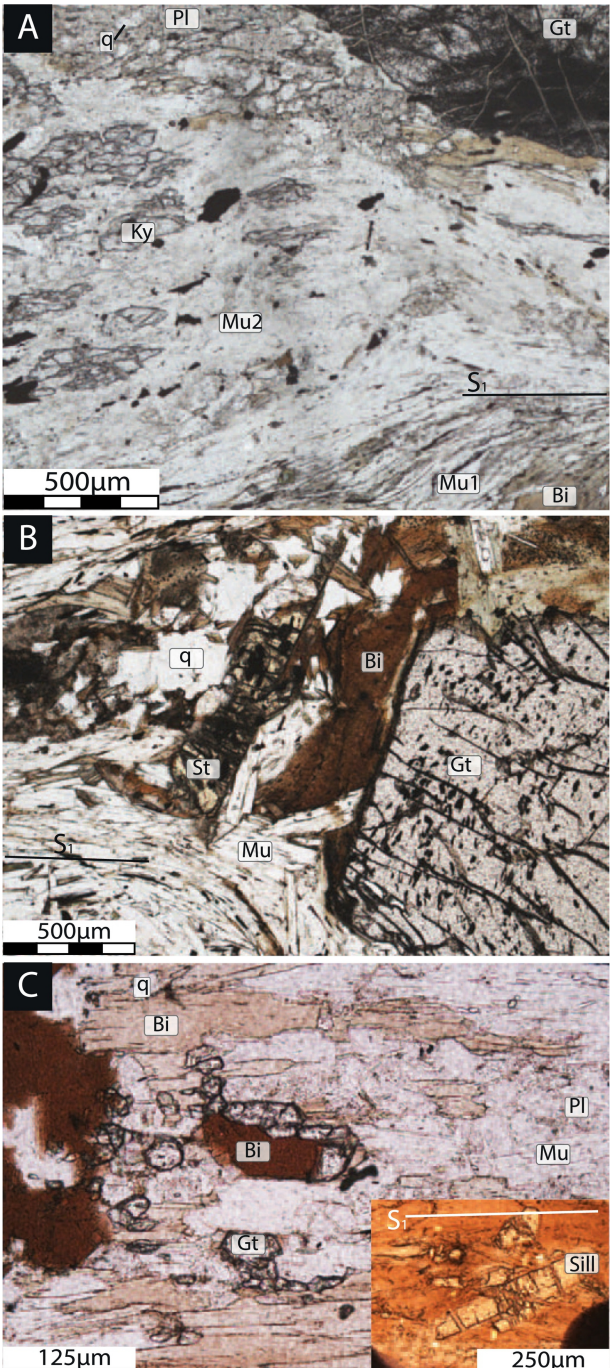
A
q
Pl
Gt
Ky
Mu2
S1
500µm
Mu1
Bi
B
q
Bi
St
Gt
S1
Mu
500µm
C
q
Bi
Pl
Bi
Mu
Gt
S1
Sill
125µm
250µm

Figure 9

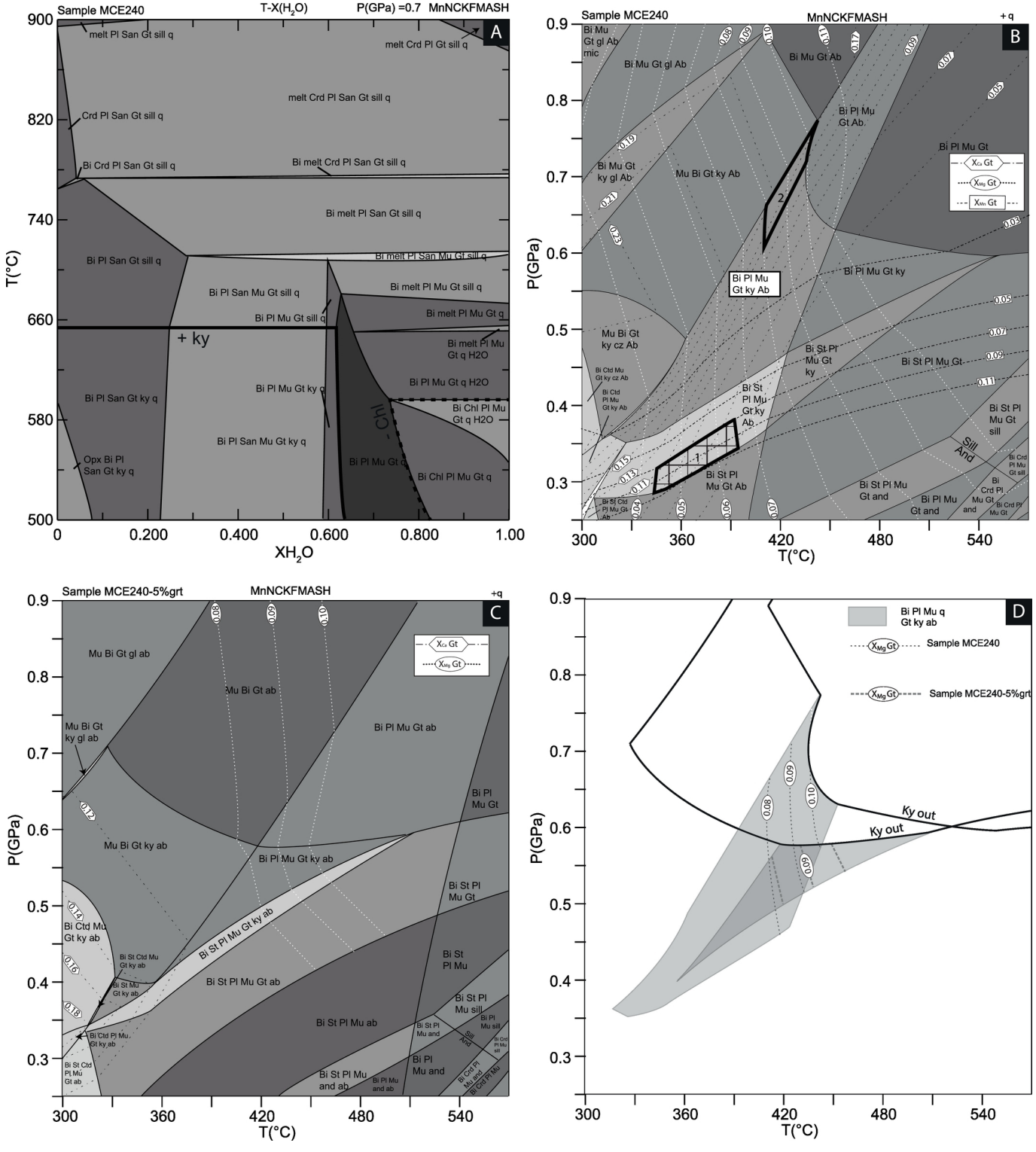
Sample MCE240
T-X(H2O)
P(GPa) =0.7
MnNCKFMASH
A
melt Pl San Gt sill q
melt Crd Pl Gt sill q
melt Crd Pl San Gt sill q
Crd Pl San Gt sill q
Bi Crd Pl San Gt sill q
Bi melt Crd Pl San Gt sill q
Bi melt Pl San Gt sill q
Bi Pl San Gt sill q
Bi melt Pl San Mu Gt sill q
Bi Pl San Mu Gt sill q
Bi melt Pl Mu Gt sill q
Bi Pl Mu Gt sill q
Bi melt Pl Mu Gt q
+ ky
Bi melt Pl Mu Gt q H2O
Bi Pl Mu Gt ky q
Bi Pl Mu Gt q H2O
Bi Pl San Gt ky q
Chl
Bi Chl Pl Mu Gt q H2O
Bi Pl San Mu Gt ky q
Opx Bi Pl San Gt ky q
Bi Pl Mu Gt q
Bi Chl Pl Mu Gt q
T(°C)
XH2O
Sample MCE240
MnNCKFMASH
+q
B
Bi Mu Gt gl Ab mic
Bi Mu Gt gl Ab
Bi Mu Gt Ab
Bi Pl Mu Gt Ab
Bi Pl Mu Gt
Bi Mu Gt ky gl Ab
Mu Bi Gt ky Ab
XCa Gt
XMg Gt
XMn Gt
Bi Pl Mu Gt ky Ab
Bi Pl Mu Gt ky
Mu Bi Gt ky cz Ab
Bi St Pl Mu Gt ky
Bi St Pl Mu Gt
Bi St Pl Mu Gt sill
Sill And
Bi St Pl Mu Gt Ab
Bi St Pl Mu Gt and
Bi Pl Mu Gt and
P(GPa)
T(°C)
Sample MCE240-5%grt
MnNCKFMASH
+q
C
Mu Bi Gt gl ab
Mu Bi Gt ab
Bi Pl Mu Gt ab
Mu Bi Gt ky gl ab
Bi Pl Mu Gt
Mu Bi Gt ky ab
Bi Pl Mu Gt ky ab
Bi St Pl Mu Gt
Bi Ctd Mu Gt ky ab
Bi St Pl Mu Gt ky ab
Bi St Pl Mu
Bi St Pl Mu Gt ab
Bi St Pl Mu sill
Bi St Pl Mu ab
Bi Pl Mu and
Bi St Pl Mu and ab
P(GPa)
T(°C)
D
Bi Pl Mu q Gt ky ab
XMg Gt
Sample MCE240
Sample MCE240-5%grt
Ky out
Ky out
P(GPa)
T(°C)

Figure 10

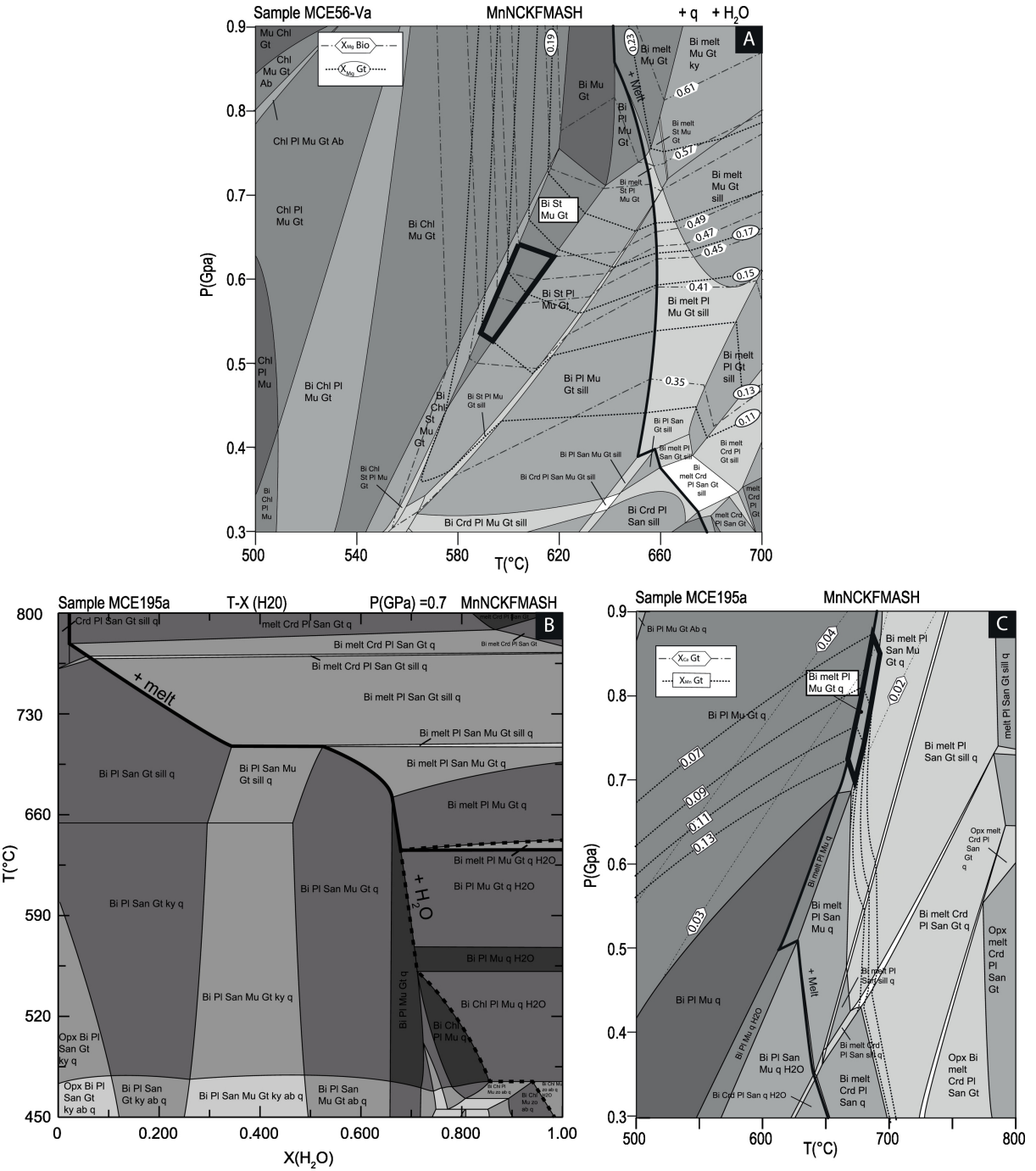
Sample MCE56-Va
MnNCKFMASH
+ q + H2O
A
P(Gpa)
T(°C)
Sample MCE195a
T-X (H20)
P(GPa) =0.7
MnNCKFMASH
B
T(°C)
X(H2O)
Sample MCE195a
MnNCKFMASH
C
P(Gpa)
T(°C)

Figure 11

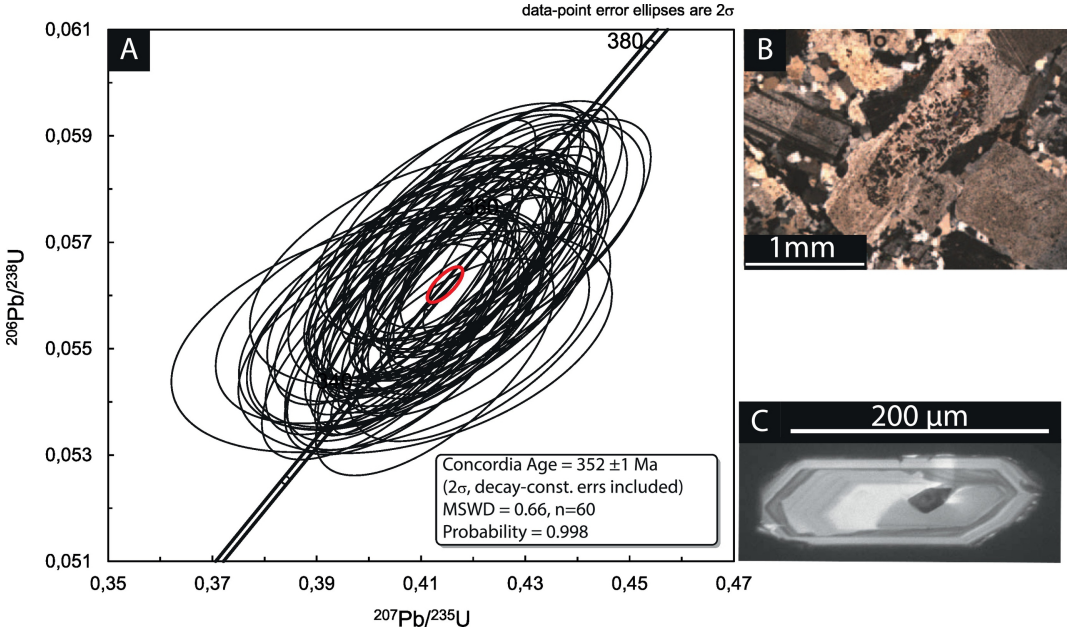
data-point error ellipses are 2σ
A
380
B
1mm
C
200 µm
Concordia Age = 352 ±1 Ma
(2σ, decay-const. errs included)
MSWD = 0.66, n=60
Probability = 0.998
0,061
0,059
0,057
0,055
0,053
0,051
0,35
0,37
0,39
0,41
0,43
0,45
0,47
206Pb/238U
207Pb/235U

Figure 12

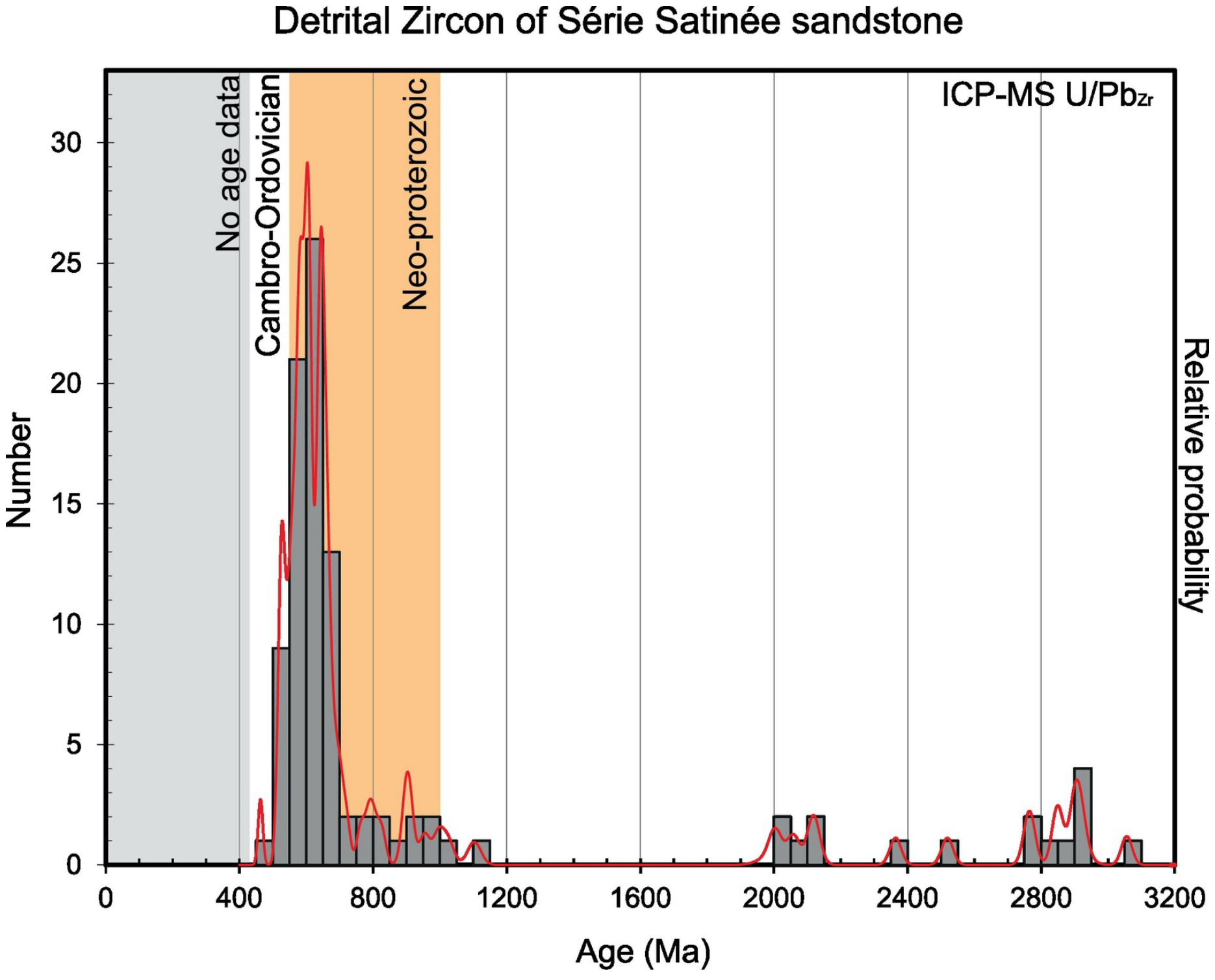
Detrital Zircon of Série Satinée sandstone
ICP-MS U/Pbzr
No age data
Cambro-Ordovician
Neo-proterozoic
Number
Relative probability
Age (Ma)
0
5
10
15
20
25
30
0
400
800
1200
1600
2000
2400
2800
3200

Figure 13

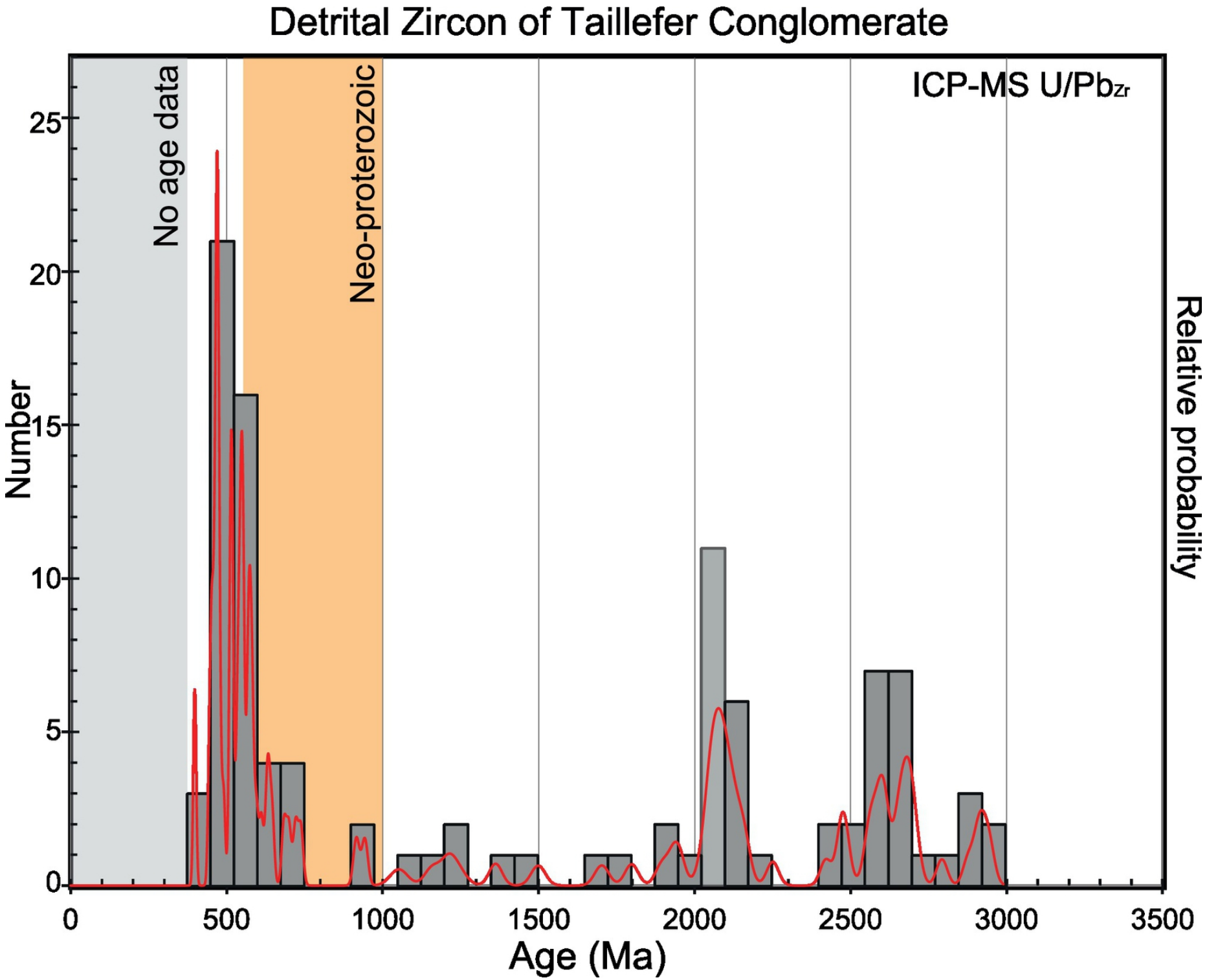
Detrital Zircon of Taillefer Conglomerate
No age data
Neo-proterozoic
ICP-MS U/Pbzr
Number
Relative probability
25
20
15
10
5
0
0
500
1000
1500
2000
2500
3000
3500
Age (Ma)

Figure 14

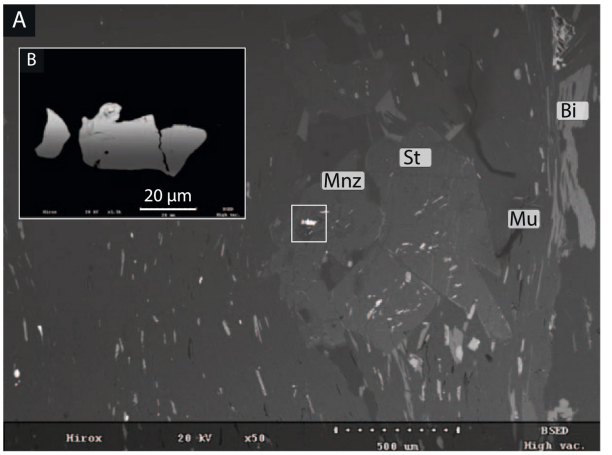
A
B
20 µm
Bi
St
Mnz
Mu
Hirox
20 kV
x50
500 um
BSED
High vac.

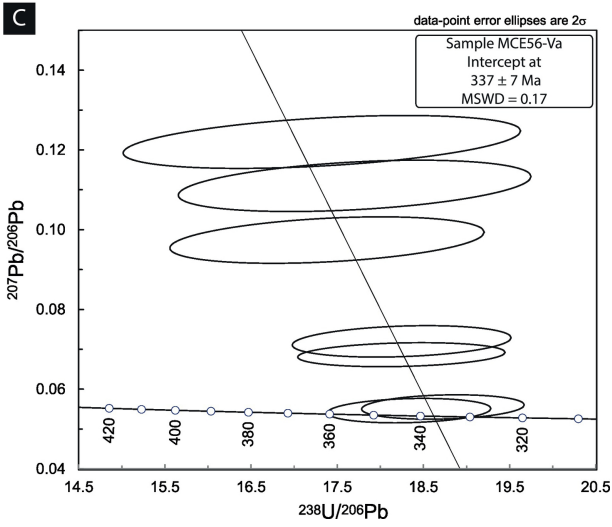
C
data-point error ellipses are 2σ
Sample MCE56-Va
Intercept at
337 ± 7 Ma
MSWD = 0.17
0.14
0.12
0.10
0.08
0.06
0.04
207Pb/206Pb
420
400
380
360
340
320
14.5
15.5
16.5
17.5
18.5
19.5
20.5
238U/206Pb

Figure 15

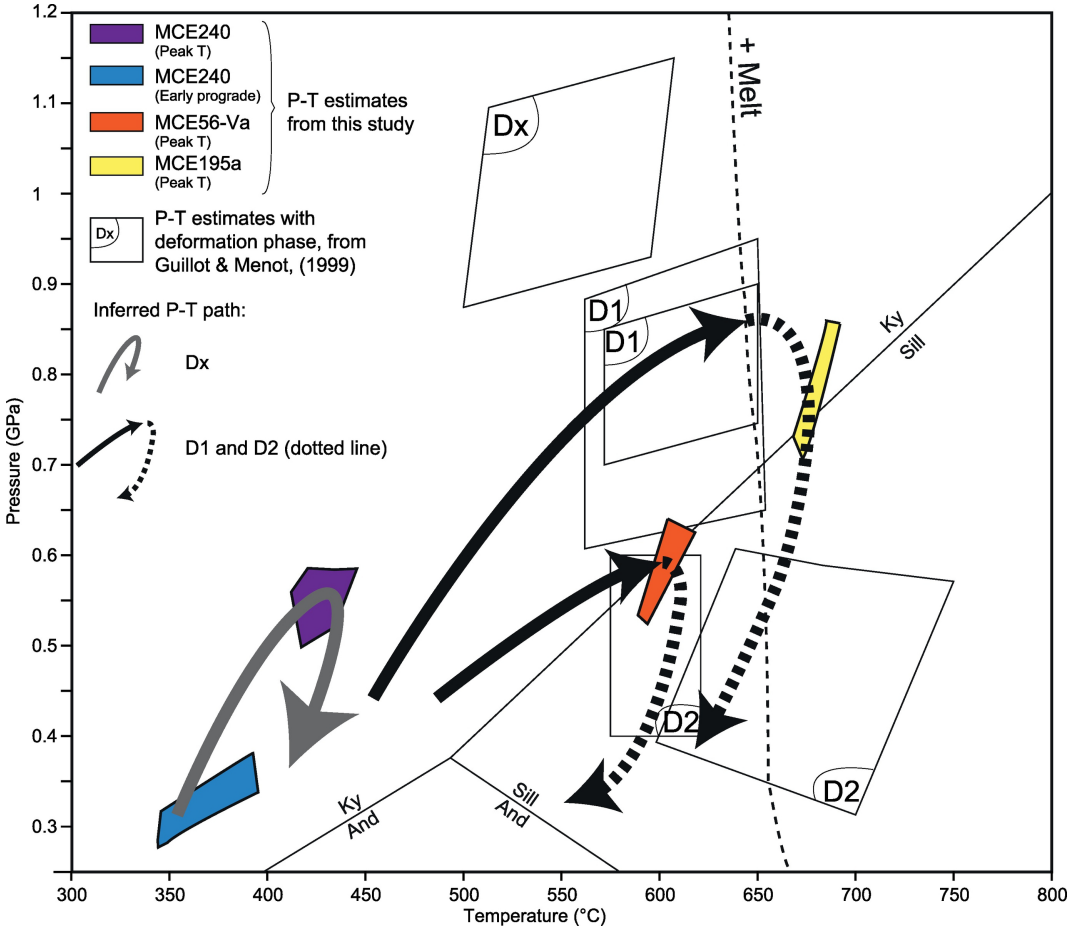
MCE240
(Peak T)
MCE240
(Early prograde)
MCE56-Va
(Peak T)
MCE195a
(Peak T)
P-T estimates
from this study
Dx
P-T estimates with
deformation phase, from
Guillot & Menot, (1999)
Inferred P-T path:
Dx
D1 and D2 (dotted line)
+ Melt
Ky
Sill
D1
D2
Ky
And
Sill
And
Pressure (GPa)
Temperature (°C)
1.2
1.1
1
0.9
0.8
0.7
0.6
0.5
0.4
0.3
300
350
400
450
500
550
600
650
700
750
800

Figure 16

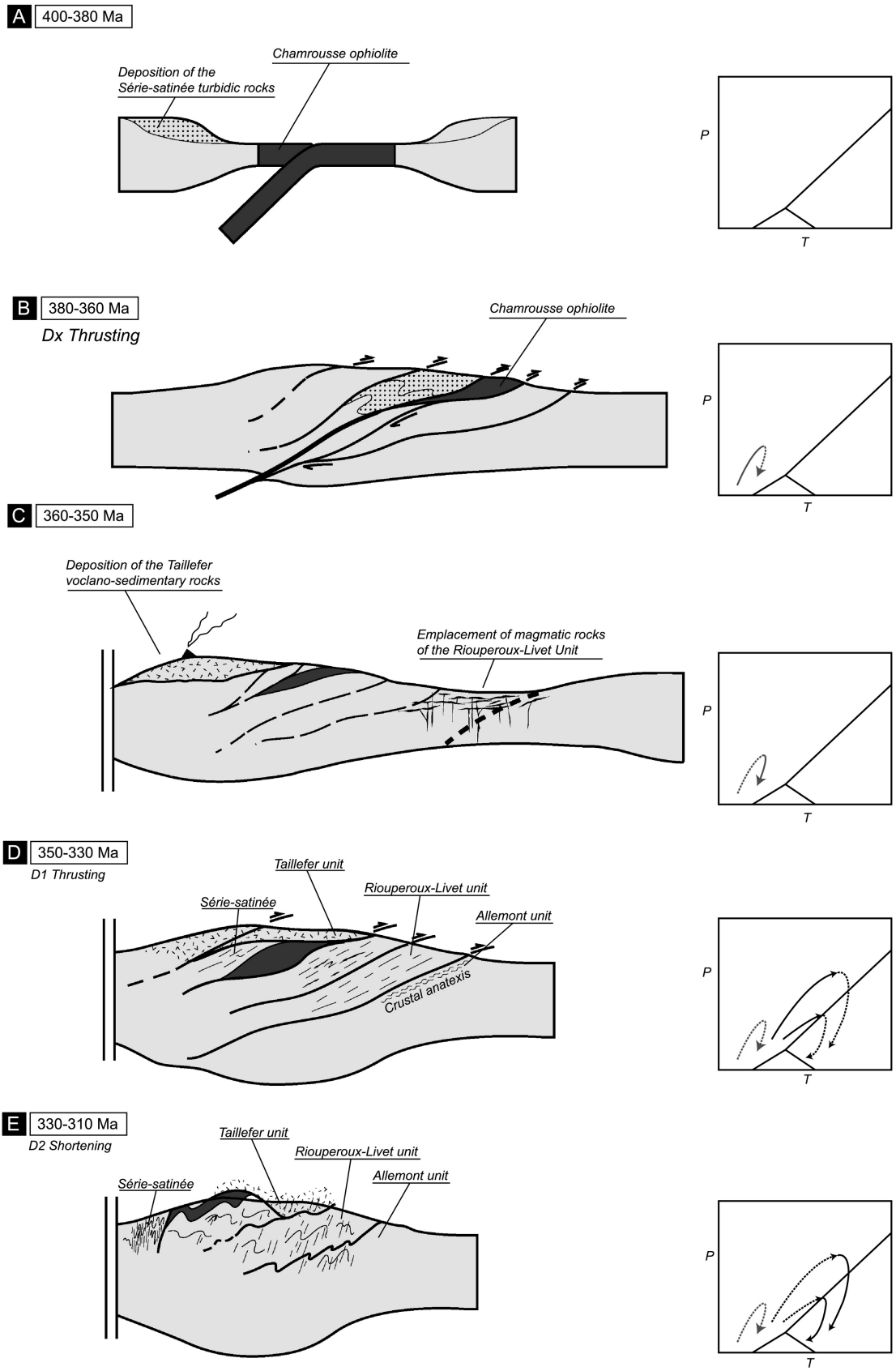
A
400-380 Ma
Chamrousse ophiolite
Deposition of the
Série-satinée turbidic rocks
P
T
B
380-360 Ma
Dx Thrusting
Chamrousse ophiolite
P
T
C
360-350 Ma
Deposition of the Taillefer
voclano-sedimentary rocks
Emplacement of magmatic rocks
of the Riouperoux-Livet Unit
P
T
D
350-330 Ma
D1 Thrusting
Taillefer unit
Riouperoux-Livet unit
Série-satinée
Allemont unit
Crustal anatexis
P
T
Thrusting of the Taillefer unit
E
330-310 Ma
D2 Shortening
Taillefer unit
Riouperoux-Livet unit
Allemont unit
Série-satinée
P
T

Figure 17